UNIVERSITY OF CALIFORNIA SAN DIEGO

Computational Techniques for Stratified Shear Flows

A dissertation submitted in partial satisfaction of the
requirements for the degree
Doctor of Philosophy

in

Engineering Sciences (Mechanical Engineering)

by

Alexandra C. VanDine

Committee in charge:

Professor Sutanu Sarkar, Chair
Professor Eugene R. Pawlak
Professor Daniel L. Rudnick
Professor David Saintillan
Professor Antonio L. Sanchez

2019

The dissertation of Alexandra C. VanDine is approved, and it is acceptable in quality and form for publication on microfilm and electronically:

_____

_____

_____

_____

_____

Chair

University of California San Diego

2019

DEDICATION

To my wonderful parents, without whom, none of my academic pursuits would have been possible.

EPIGRAPH

The Road goes ever on and on

Down from the door where it began.

Now far ahead the Road has gone,

And I must follow, if I can,

Pursuing it with eager feet,

Until it joins some larger way

Where many paths and errands meet.

And whither then? I cannot say.

J.R.R. Tolkien

TABLE OF CONTENTS

LIST OF FIGURES

LIST OF TABLES

ACKNOWLEDGEMENTS

I'd like to express my sincere thanks to my advisor, Dr. Sutanu Sarkar, for his guidance. His knowledge of turbulence and fluid mechanics has been invaluable in my studies and I am grateful that I was able to spend graduate school in the Computational Fluid Dynamics Lab. I'd also like to thank my colleagues in the lab for their input and support even when times are tough as well as the enlightening conversations we've had over the years about our dreams for the future. I've learned so much from all of you and know that I'm a better person for it.

My publications would not have been possible without the guidance of my CFD Lab coauthors, Karu and Hieu. I'm still amazed by Karu's coding talent and firmly believe that I wouldn't know half of what I do without Hieu's hours spent teaching me about stratified shear flows. I couldn't ask for two better people to call coauthors. This dissertation was made complete with the feedback of my dissertation committee members: Dr. Eugene R. Pawlak, Dr. Daniel L. Rudnick, Dr. David Saintillan, and Dr. Antonio L. Sanchez. I appreciate their input and the opportunity to share my research.

There are too many other people at UCSD who have helped me along the way to single out everyone so, for now, I'll say thank you for being there for me. I'd also like to thank everyone who stepped up when it was time for me to take a step back from hosting our departmental tea times. If there's one thing our department loves, its tea time and I'm happy to have been a part of such a great legacy.

A huge thanks to my friends from the University of Virginia alumni group in San Diego. You guys kept me sane with trips, hikes, golf, happy hours, and an endless schedule of game watches. Go Hoos! To all my friends across the country and those abroad, thank you for your support. I couldn't have done it without you.

My most enthusiastic thanks goes to my parents who are the most supportive and loving people I know. Mom and Dad, youve been there for every athletic event and educational milestone and I owe everything I have achieved to you. I can't even begin to describe my appreciation. To my grandfathers, thank you for introducing me to science and engineering. I don't know where I would

be if I hadn't heard you talk so enthusiastically about your work but I know that you were a huge part of my decision to enter this field.

Here's to having many more adventures down the road with the people who have supported me throughout this journey.

Chapter 2 is a reprint of material in preparation for publication as follows: A. VanDine, H. T. Pham, S. Sarkar, "Evolution of turbulent shear layers with uniform stratification at high Reynolds number", 2019. The author of this dissertation is the primary investigator and author of this work.

Chapter 3 is a reprint of material under review for publication as follows: A. VanDine, H. T. Pham, S. Sarkar, "Investigation of LES models for a stratified shear layer", *Comput. Fluids*, 2019. The author of this dissertation is the primary investigator and author of this work.

Chapter 4 is a reprint of material published as follows: A. VanDine, K. Chongsiripinyo, S. Sarkar, "Hybrid spatially-evolving DNS model of flow past a sphere", *Comput. Fluids*, 171, 41-52, 2018. The author of this dissertation is the primary investigator and author of this work.

VITA

2019	Ph. D. in Engineering Sciences (Mechanical Engineering) University of California San Diego, La Jolla, CA, USA
2015	M. S. in Mechanical Engineering University of California San Diego, La Jolla, CA, USA
2014	B. S. in Aerospace Engineering University of Virginia, Charlottesville, VA, USA

ABSTRACT OF THE DISSERTATION

Computational Techniques for Stratified Shear Flows

by

Alexandra C. VanDine

Doctor of Philosophy in Engineering Sciences (Mechanical Engineering)

University of California San Diego, 2019

Professor Sutanu Sarkar, Chair

This work utilizes various computational techniques to study the turbulent mechanisms found in stratified shear flows. Three-dimensional DNS was used to investigate the influence of stratification on turbulence and mixing within a shear layer between two currents. Similarities in the development of secondary instabilities during transition to turbulence and discrepancies in flow evolution are seen between the case of uniform stratification considered here and the two-layer density profile of prior works. Vertical contraction of the shear layer is identified in cases with low Richardson number and determined to be the result of the flattening of Kelvin-Helmholtz billows before the flow becomes fully turbulent. Transition layers with enhanced shear and stratification form at the periphery of the shear layer and are found to support turbulent mixing. In an effort to find a less computationally costly tool than DNS, the Dynamic Smagorinsky, Ducros, and

WALE subgrid-scale models were chosen for an LES study of the stratified shear layer. This investigation revealed the Ducros model to the least computationally costly LES option and the most reliable with coarsening grid resolution. A subgrid analysis revealed the LES models to be largely unsuccessful in capturing convective turbulence though the mean flow and turbulent kinetic energy were well-captured.

To address the limitations of DNS and LES, a hybrid spatially-evolving DNS model was developed. The wake of a sphere towed in a stratified background was selected for validation. The hybrid model involves extracting planes from a spatially-evolving, body-inclusive simulation and feeding the planes as inflow into a body-exclusive simulation thereby eliminating the need for a highly resolved grid to capture flow near the body. This study revealed that particular attention should be paid to the extraction location, grid resolution, and time step between extractions. Planes must be extracted downstream of the recirculation region behind the body and sufficient grid resolution is required in the body-exclusive simulation to capture small-scale turbulence. Results show the hybrid DNS model to be an effective tool in the study of the stratified turbulent wake. The combination of results presented herein offer computational techniques and cost-saving options for future studies of shear flows.

Chapter 1

Introduction

Turbulence is a complex phenomenon observed in a myriad of diverse fields including astrophysics, naval engineering, climatology, and combustion to name a few. As turbulence is characterized by chaotic behavior over a wide range of length and time scales, it has proven to be a historically interesting and challenging subject of study. Scientists and engineers have sought to better understand the physics of turbulent flow and transport using experiments, theoretical tools, and numerical models. With vast improvements in computational tools over the past few decades, there has been particular interest in numerical modeling of turbulent geophysical flows for the purposes of improved environmental forecasting and engineering of technologies which operate in the natural environment. In such flows, it is important to consider the variability of density in the environment also known as its stratification. Nonhomogeneity in density greatly impacts flow evolution and turbulence and is, thus, a crucial consideration in studies which seek to characterize turbulence and mixing. While there exist many canonical shear flows which can be used in such studies, this work specifically addresses the numerical modeling of shear layers and wakes in stratified environments in an effort to improve fundamental knowledge of such flows.

Turbulent mixing in the environment is a combination of both shear-driven and buoyancy-driven processes. Buoyancy is known to stabilize turbulence and a variety of instabilities that are found in stratified shear flows. The physical mechanisms resulting from the interaction of parallel

shear flows in a stably stratified environment are observed in the ocean where shear instabilities generate turbulent mixing. Consequently, the accurate prediction of such mixing and turbulent energetics is key in the design of many naval applications.

In a stably stratified shear layer with moderate stratification, Kelvin-Helmholtz (KH) instabilities are generated by inflectional shear and their evolution is modified by stratification. These KH billows are followed by secondary instabilities that eventually break down into three-dimensional turbulence. The shear layer thickens by entrainment until the potential energy barrier to overturning motions at the scale of the shear layer thickness becomes sufficiently large to arrest shear layer growth which is an inevitable consequence of stratification even if its value is small relative to the initial shear. The creation of these billows, transition to turbulence, and decay of turbulence have been widely studied using a variety of laboratory experiments (Thorpe, 1973; Lawrence *et al.*, 1991; Schowalter *et al.*, 1994; De Silva *et al.*, 1996) and simulations (Smyth & Moum, 2000*b*,*a*; Brucker & Sarkar, 2007; Pham *et al.*, 2009; Pham & Sarkar, 2010, 2014; Khani, 2018; Kaminski & Smyth, 2019). Particular attention has been paid to the influence of turbulence on the density field of a stratified fluid and mixing mechanisms (Peltier & Caulfield, 2003; Salehipour *et al.*, 2015) as well as the development and evolution of instabilities in stratified shear flows (Mashayek & Peltier, 2012*a*,*b*). In a stably stratified mixing layer, buoyancy effects are constrained to larger scales such that the smallest scales of turbulent motion are not initially impacted. However, the scales of turbulence increase in size as the mixing layer evolves and buoyancy increasingly inhibits turbulent motions.

Quantifying the rate of mixing has important implications in large-scale ocean and atmospheric models. Ocean models often parametrize mixing efficiency (Γ) with a constant empirical value, where Γ is understood to be the ratio of the gain in the background potential energy over the sum of the gain plus the dissipation rate of turbulent kinetic energy. A typical value of approximately 0.16 is used although the physics behind the mixing processes and the dependence of Γ on flow conditions are not yet clearly understood (Osborn, 1980). In the past two decades, there has been a sustained effort to more accurately quantify mixing efficiency using three-dimensional,

turbulence-resolving direct numerical simulations (DNS). Smyth & Moum (2000*b*) and Caulfield & Peltier (2000) performed some of the first DNS of three-dimensional turbulence in a stratified shear layer and were able to quantify the rate of mixing despite being at a low Reynolds number. Since then, due to the benefits of increased computational power, DNS have been able to examine higher Reynolds numbers, most notably in the recent works by Mashayek & Peltier (2013); Mashayek *et al.* (2013); Salehipour *et al.* (2015); Salehipour & Peltier (2015); Kaminski & Smyth (2019). The Reynolds numbers in these simulations reach up to 40,000, a value considered high enough to reflect turbulent dynamics at geophysical scales. Some significant results from these simulations are: (1) Γ can have a significantly higher value than 0.16 and (2) the value varies significantly with Reynolds number (*Re*), Prandtl number (*Pr*), stratification (via using Richardson number, *Ri*), and even the amount of pre-existing turbulence in the shear layer (Brucker & Sarkar, 2007; Kaminski & Smyth, 2019). For a review of these effects on Γ, readers are referred to the work of Mashayek & Peltier (2013) (hereafter referred to as MP13) and Mashayek *et al.* (2013) (hereafter referred to as MCP13). Their studies indicate that mixing efficiency depends on the route to turbulence, namely how the two-dimensional Kelvin-Helmholtz billows transition into fully three-dimensional turbulence. They found a myriad of secondary instabilities to develop during the transition period that controls the mixing rate. Interestingly, they assert the existence of an intermediate value of stratification, $Ri \approx 0.16$, which produces the optimal turbulent mixing given that the secondary shear instabilities are richest in this regime of *Ri*. They find that the mixing efficiency decreases as *Ri* deviates from this value, either larger or smaller.

Nearly all DNS of stratified layers at high Reynolds numbers use a hyperbolic tangent profile for velocity and density in order to represent a shear layer that develops at an interface between two layers having different but constant density. In the oceans and atmosphere, it is typical that the stratification extends beyond the region of the shear layer such that a uniform stratification is a more appropriate representation of the density gradient than the two-layer profile. There are intrinsic differences between these configurations. In particular, for the same value of *Ri* at the center of the shear layer, the density difference across the layer is larger in the case with uniform

stratification. In other words, the average value of the stratification is larger, leading to the possibility of different physics associated with turbulent mixing. Furthermore, Pham *et al.* (2009) show that the external stratification, when sufficiently strong, can support propagating internal waves. At low $Re = 1,000$, they show that the internal wave flux can be as large as 15% of the turbulent production generated in the shear layer. The strength of the internal wave reduces as Re increases to 5,000 (Pham & Sarkar, 2010). Recent DNS of shear layers with uniform stratification in Watanabe *et al.* (2018) (hereafter referred to as WR18) at $Re = 6,000$ reveal interesting turbulent dynamics at the turbulent/non-turbulent interface (TNTI). These authors also find that at low Ri, though internal waves do not propagate far from the shear layer, the wave flux measured at the TNTI can reach up to 50% of the dissipation rate generated inside the shear layer. The effect of uniform stratification on the mixing rate at high Reynolds number is presently unknown. Table 1.1 lists the parameters of recent two-layer and uniformly stratified DNS at high Reynolds number. It is clear from the table that DNS of shear layers with uniform stratification at high Reynolds number would improve the present understanding of stratified turbulent mixing. It is noted that, according to Mashayek & Peltier (2013), the dynamics of mixing is richest when $Re \geq 24,000$.

There is also a need to quantify flow dynamics of the transition layers which develop at the edges of the shear layer during transition to fully three-dimensional turbulence. Previous simulations have shown enhanced shear and stratification in the shear layer. However, it is presently unknown how the uniform stratification of the ambient can impact the development of the transition layer as well as the turbulent and mixing physics therein. In oceans, a transition layer is often located between the surface mixed layer and the thermocline below (Johnston & Rudnick, 2009). Here, the transition layer controls the rate of heat flux at the base of the mixed layer. Given its influence, it is necessary to explore the turbulent physics which arise in the layer.

Specifically, recent observations and simulations reveal nightly bursts of deep-cycle turbulence in the Pacific Equatorial Under-Current (EUC) which are triggered by descending transition layers (Smyth *et al.*, 2013; Pham *et al.*, 2013). It has been shown that, as the transition layer descends down from the base of mixed layer to depths, it enhances the local shear rate, reduces the

Table 1.1: Parameters used in recent DNS of stratified shear layers with high Reynolds number. Listed are simulations using a two-layer density profile with a sufficiently large *Re*. For the case of uniform stratification, the highest Reynolds number simulated is 6,000. Note that the Reynolds numbers for the two-layer cases given in this table are a factor of four larger than the number stated in the works referenced above due to differences in notation.

Re	*Ri*	Density profile	Source
16,000	0.16	two-layer	Kaminski & Smyth (2019)
16,000	0.20	two-layer	Kaminski & Smyth (2019)
24,000	0.12	two-layer	MP13, MCP13, Salehipour & Peltier (2015)
24,000	0.14	two-layer	MP13, MCP13
24,000	0.16	two-layer	MP13, MCP13
24,000	0.18	two-layer	MP13, MCP13
24,000	0.20	two-layer	MP13, MCP13
32,000	0.12	two-layer	MP13
40,000	0.04	two-layer	MP13
40,000	0.12	two-layer	MP13
6,000	0.01	uniform	WR18
6,000	0.04	uniform	WR18
6,000	0.08	uniform	WR18
24,000	0.04	uniform	present study
24,000	0.08	uniform	present study
24,000	0.12	uniform	present study
24,000	0.16	uniform	present study

local gradient Richardson number, and triggers shear instabilities and turbulence. It is presently unclear what factors control the turbulent momentum flux associated with the descending transition layer. Pham *et al.* (2017) suggest there are seasons in which the deep-cycle turbulence does not occur, possibly because the turbulent flux in the transition layer is not sufficiently strong when the stratification in the ambient is too strong. It is, therefore, of interest to understand how the transition layer develops and propagates with different levels of stratification in a canonical problem that is simpler than the EUC.

To improve our knowledge of mixing in stratified shear layers and the transition layers which develop therein, an investigation in which four DNS with differing Richardson number (*Ri*) indicative of the stratification strength were compared. Chapter 2 provides a detailed analysis of this study and quantifies the influence of stratification on shear layer flow dynamics.

For temporally-evolving DNS, an increase of the Reynolds number corresponds to a reduction of the smallest scales of motion and a consequent increase in the number of grid points required to resolve all scales, which leads to a prohibitive increase of computational expense. Simulations of stratified shear flows performed at a high Reynolds number are especially significant as they are directly relevant to realistic environmental flows. As such, LES models are often used as an alternative to DNS. LES studies are appealing because they reduce computational cost by using a subgrid-scale (SGS) model for small-scale turbulence while only larger scales are resolved. This allows for more flexibility in simulation design, avoiding many limitations of DNS although sacrificing the fact that all scales of motion are not solved for directly as in DNS. A number of LES models have been employed in the study of stratified flows (Armenio & Sarkar, 2002; Chamecki *et al.*, 2007; Scotti, 2010; Pham & Sarkar, 2014; Chongsiripinyo & Sarkar, 2017; Khani, 2018). Although specific SGS models have been utilized in stratified flows, there is need for a comprehensive and direct comparison of widely used LES models. This need motivates another component of the present work.

To that end, three LES models, namely the Dynamic Smagorinsky, Ducros, and Wall-Adapting Local Eddy-Viscosity (WALE) models, were used to simulate a shear layer in a uniformly stratified flow environment. In brief, the Dynamic Smagorinsky model uses two filters (a grid and a test filter) and dynamically calculates the coefficients used to model eddy viscosity as opposed to setting a coefficient *a priori* (Germano *et al.*, 1991; Lilly, 1992). A version of this model was recently used by Chongsiripinyo & Sarkar (2017) in their study of the impact of stratification on flow evolution in the turbulent wake behind a sphere at a moderate Reynolds number. In contrast, the Ducros model is a filtered structure-function (FSF) model which applies a high-pass filter to the LES field in order to obtain a filtered version that retains the smaller scales of the LES field and uses a second-order structure function of the explicitly filtered LES field to estimate eddy viscosity (Ducros *et al.*, 1996). Sundermeyer *et al.* (2014) utilized this model in their investigation of turbulent mixing in the surface ocean boundary layer. Furuichi & Hibiya (2015) employed the Ducros model in their study of upper-ocean mixing. In the WALE model, eddy viscosity is

determined without explicit filtering and instead employs a tensor invariant that takes into account the influence of both strain and rotation. This model is well suited to the simulation of complex geometries and wall-bounded flows as it uses only local gradients to compute eddy viscosity and reproduces proper wall scaling (Nicoud & Ducros, 1999). The WALE model was recently used by Posa & Balaras (2018) to study the physics of towed and self-propelled submarine geometries. Details concerning these models and the results of their use in studying a stratified shear layer can be found in chapter 3.

Of additional interest are the physical mechanisms within turbulent wakes. In a broad sense, a wake is created as flow encounters an obstacle and disturbances are noted in the lee of the body. The study of wakes in stratified flow environments is important to many naval and environmental applications including ship and submersible movement, marine swimmers, and flow over topography in the atmospheric boundary layer and on the ocean floor. Over the length scales observed in such stratified flows, buoyancy effects are important to the quantification of turbulence. The near wake is a complex flow that involves flow separation dependent on boundary layer dynamics, vortex shedding from the body, and recirculation regions. The far wake is a canonical turbulent shear flow. Like the shear layer studied in chapter 2, the wake has vertical mean shear that competes with the stabilizing effect of stratification but a key difference is the added presence of mean horizontal shear.

Lin & Pao (1979) provide a comprehensive review of wakes in stratified flows prior to 1979 which highlights interesting large-scale structures in self-propelled and towed bodies. More recently, Riley & Lelong (2000) discussed a wide range of numerical simulations, laboratory experiments, and theory for low Froude number (Fr) flows while progress specific to wake detection, geophysical and marine swimmer flow evolution, and related laboratory experiments is reviewed by Spedding (2014). Several experimental studies have investigated bluff body wakes using towed or self-propelled spheres in a stratified fluid (Pao & Kao (1977); Chashechkin (1989); Lin *et al.* (1992*b*,*a*); Chomaz *et al.* (1993*b*,*a*); Spedding *et al.* (1996); Spedding (1997); Bonnier *et al.* (2000); Bonnier & Eiff (2002)). Chashechkin (1989) studied the hydrodynamics of stratified flow past a sphere using

optical methods noting clear differences in the internal wave propagation and the high-gradient flow envelope in the lee of the body for different Froude numbers. Lin *et al.* (1992*b*) and Lin *et al.* (1992*a*) analyzed linearly stratified fluid past a towed sphere for a variety of Fr and Re. They determined that many flow features are dramatically influenced by the level of stratification. In particular, horizontal scales of motion are notably larger than vertical scales owing to the inhibition of vertical modes by stratification. Observations of vortex shedding as well as a variation in the size and behavior of an attached region in the near wake behind the sphere are noted. They also assert that sufficiently large Fr and $Re > 2000$ are criteria for the existence of turbulence. Chomaz *et al.* (1993*b*) investigated the near wake structure behind a sphere, identifying four flow regimes with Fr dependence: a quasi-two-dimensional ($Q2D$) regime when $0.25 < Fr < 0.8$, a lee wave dominated regime when $0.8 < Fr < 1.5$, a transition region between lee wave domination and stratification independence when $1.5 < Fr < 4.5$, and a three-dimensional regime independent of stratification when $Fr > 4.5$.

The work on the near wake was extended by Chomaz *et al.* (1993*a*) to document the $Q2D$ regime and transition in the far wake. Bonnier *et al.* (2000) investigated the vortical structure of the far wake and observed the same $Q2D$ behavior seen in previous works suggesting universal behavior in stratified flows. Late wake evolution was further explored for $Re = [10^3, 10^4]$ and $Fr = [1, 10]$ by Spedding *et al.* (1996) who observed flow dominated by coherent vortices and provided scaling arguments for various flow parameters. Spedding (1997) later extended the study to high $Fr = [10, 240]$ where an intermediate non-equilibrium (NEQ) regime which precedes the late wake was identified. In this region between the three-dimensional near wake and the $Q2D$ regimes, buoyancy effects become increasingly important. Eventually, vertical motions are suppressed by the effect of stratification and the coherent vortices known as "pancake eddies" characteristic of the $Q2D$ regime emerge. Bonnier & Eiff (2002) used hot-film measurements and particle image velocimetry to characterize the impact of buoyancy on the transition from the near to far wake and analyze the far wake in detail. Investigation of the transition region in stratified wakes led to identification of a subregion within the NEQ regime, termed the accelerated collapse (AC) region,

located approximately between $2 \leq Nt \leq 7$, during which the mean defect velocity briefly increases before continuing to decay. Another region, termed buoyant collapse (*BC*), was proposed by Meunier *et al.* (2006) to appear within the *NEQ* regime at high *Re*. A reproduction of figure 9 from Brucker & Sarkar (2010) is given in Figure 1.1 to illustrate the various flow regimes in the development of the towed wake in a stratified fluid. It should be noted that these simulations were temporally evolving.

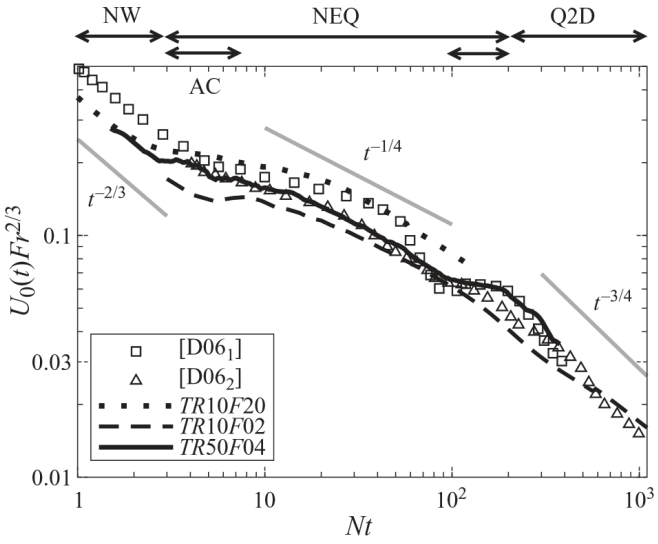

Figure 1.1: Reproduction of figure 9 from Brucker & Sarkar (2010) to illustrate the various flow regimes in the development of the towed wake in a stratified fluid. Specifically shown is the evolution of peak defect velocity plotted as $U_0(t)Fr^{2/3}$ versus Nt. [$D06_1$] corresponds to the data from the simulations of Diamessis & Spedding (2006) with $Re = 5.0 \times 10^3$ and $Fr = 2$. [$D06_2$] corresponds to the data from the simulations of Diamessis & Spedding (2006), $Re = 1.0 \times 10^5$ and $Fr = 8$. The cases $TR50F04$, $TR10F02$, and $TR10F20$ are temporally-evolving towed sphere simulations with $Re = 5.0 \times 10^4$, 1.0×10^4, and 1.0×10^4 and $Fr = 4$, 2, and 20, respectively.

In addition to the study of the mean defect velocity scale, the far wake is of particular interest due to the aforementioned formation of coherent vortex structures. It was originally thought that the appearance of these late wake structures was due to the propagation of instabilities in the near wake (Chomaz *et al.* (1993*b*); Spedding (1997)). However, more recent experiments (Bonnier *et al.* (1998)) and simulations which were initialized with a prescribed flow field (Gourlay *et al.* (2001); Dommermuth *et al.* (2002); Diamessis & Spedding (2006); Brucker & Sarkar (2010)) have shown that upstream instabilities are not a necessary condition for the coherent formation of late wake

structures. Performed by Gourlay *et al.* (2001), the first fully three-dimensional temporally-evolving direct numerical simulation (DNS) of its kind found "pancake eddies" despite initial conditions not containing so called "coherent seeding" from the flow past a body. The emergence of these structures was, therefore, concluded to be independent of coherence in the initial conditions.

Numerical simulations using a temporally-evolving flow model have been used extensively to study the turbulent wake. Temporal evolution neglects streamwise flow evolution, thereby allowing the use of periodic boundary conditions which significantly reduces the computational cost of a simulation. DNS temporal flow studies have been employed to gain insight into flow dynamics, parameter dependency, energy budgets, and scaling including, but not limited to, the study of towed and self-propelled wakes by Brucker & Sarkar (2010) who found a longer NEQ regime at the higher $Re = 50,000$, Prandtl number study by de Stadler *et al.* (2010), and the weakly stratified wake investigation by Redford *et al.* (2015).

LES have also been employed to study the physical mechanisms of the turbulent wake. Dommermuth *et al.* (2002) simulated the wake behind a towed sphere at $Re = 10^4$ and $Re = 10^5$. Diamessis *et al.* (2011) performed implicit LES of a wake and found that turbulence at large Nt (where N is the buoyancy frequency and t is the turbulent time scale) is enhanced when Re is large, up to $Re = 10^5$ in their simulations. Constantinescu & Squires (2003) also performed LES of flow over a sphere at $Re = 10^4$.

Despite the abundance of temporally-evolving DNS and LES, there exist drawbacks to their use. One such limitation is that an approximation of initial fluctuations which is often taken from measurements of the unstratified downstream wake is necessary and, as such, it may not be possible to accurately capture buoyancy effects in the near wake. An alternative is a spatially-evolving simulation including the body that resolves the boundary layer, flow separation, and the near wake. Simulations of this sort for the stratified wake have successfully documented vortex shedding, boundary layer dynamics as well as turbulence in the near and intermediate wake (Orr *et al.* (2015); Pal *et al.* (2016, 2017); Chongsiripinyo *et al.* (2017); Chongsiripinyo & Sarkar (2017)). Pal *et al.* (2017) performed spatially-evolving DNS of flow past a towed sphere at $Re = 3700$ and $Fr = 1$, 2,

3 and found strong buoyancy effects such as a decrease in the recirculation length, increase in near wake turbulence anisotropy, lee waves, and oscillatory modulation of the streamwise velocity.

Although illuminating results are found by body-inclusive, spatially-evolving simulations, there is a limitation to their practicality. Because a large number of grid points are required near the body to resolve the boundary layer and flow separation, the simulations are computationally expensive and unable to extend far downstream without prohibitive cost. The final contribution of this work is the development of a hybrid spatially-evolving DNS model which addresses these drawbacks. For the cases in chapter 4, the model uses inflow conditions generated from a well-resolved, spatially-evolving, body-inclusive DNS of the wake past a towed sphere and performs a separate spatially-evolving simulation without including the body. Pasquetti (2011) suggested a similar idea in which a spatial development study was carried out to generate initial conditions although these conditions were used in a temporally-evolving simulation. Although additional research has been performed concerning the generation of realistic initial conditions to be used in numerical simulations (Lund *et al.* (1998); Xiang *et al.* (2015)), the work presented herein is the first hybrid spatially-evolving study of its kind for stratified flows.

The remainder of this work is structured as follows. Chapters 2 and 3 discuss the evolution of turbulence in a shear layer in a uniformly stratified background using DNS and LES, respectively. The work in chapter 3 is under consideration for publication in *Computers & Fluids* while that of chapter 2 is in preparation for publication. Chapter 4 focuses on an investigation of the turbulent wake and provides details concerning the formulation and validation of the hybrid model which is published in *Computers & Fluids*. A final evaluation of this work and its contribution to the scientific community is given in chapter 5.

Chapter 2

Evolution of turbulent shear layers with uniform stratification at high Reynolds number

There is need for an investigation of turbulent mixing physics in shear layers at high Reynolds number using density profiles of uniform stratification as evidenced in chapter 1. Specifically, results of the current investigation are compared to those of MP13, MCP13 and WR18 in table 1.1 in order to answer the following: (1) Is the effect of uniform stratification similar to what has been observed in prior two-layer simulations and (2) at what value of Ri does the shear layer have optimal mixing?

Particular attention is paid to the flow dynamics of the transition layers which form at the periphery of the shear layer and have yet to be studied within the framework of a canonical stratified shear layer. DNS with varying background stratification are performed to assess the impact of buoyancy effects on the development of, and mixing mechanisms within, transition layers.

2.0.1 Formulation

2.0.1.1 Stratified shear layer

The problem of a temporally evolving stratified shear layer with uniform stratification is considered. A sketch of the shear layer with relevant initialization parameters is shown in figure 2.1. The flow is initialized similarly to previous works (Brucker & Sarkar, 2007; Pham & Sarkar, 2010, 2014; Watanabe *et al.*, 2018) with a streamwise velocity field (u) continuously varying in the vertical direction (z) as given by

$$\langle u^* \rangle (z^*, t = 0) = -\frac{\Delta U^*}{2} \tanh\left(\frac{2z^*}{\delta^*_{\omega,0}}\right), \tag{2.1}$$

where ΔU^* denotes the velocity difference across the shear layer and the initial vorticity thickness of the shear layer is given by

$$\delta^*_{\omega,0}(z^*, t = 0) = \frac{\Delta U^*}{(\mathrm{d}\langle u^* \rangle / \mathrm{d}z^*)_{\max}}. \tag{2.2}$$

Note that in this configuration, maximum shear at initial time ($t = 0$) occurs at the centerline of the shear layer where $z^* = 0$. A superscript $*$ denotes a dimensional quantity while the $\langle\rangle$ operator indicates horizontal averaging.

Various configurations of density-stratified shear layers have been studied (Pham *et al.*, 2009; Pham & Sarkar, 2010; Watanabe *et al.*, 2018). Pham & Sarkar (2010) compared the mechanisms present in the well-known two-layer case with the J_d density profile characteristic of observations in the ocean pycnocline. Instead, this work utilizes a uniformly distributed stratification, a choice motivated by atmospheric and ocean observations in which stratification extends beyond regions of shear (Fritts, 1982; Smyth *et al.*, 2001). In the stably stratified fluid considered, uniform stratification is characterized by a constant background density gradient in the vertical direction such that density is initialized by $\langle \rho^* \rangle (z^*, t = 0) = \rho^*_b(z^*) + \tilde{\rho}^*$ where ρ^*_b denotes the time-invariant background density profile and $\tilde{\rho}^*$ is the deviation from the background. A reference density (ρ^*_0) represents

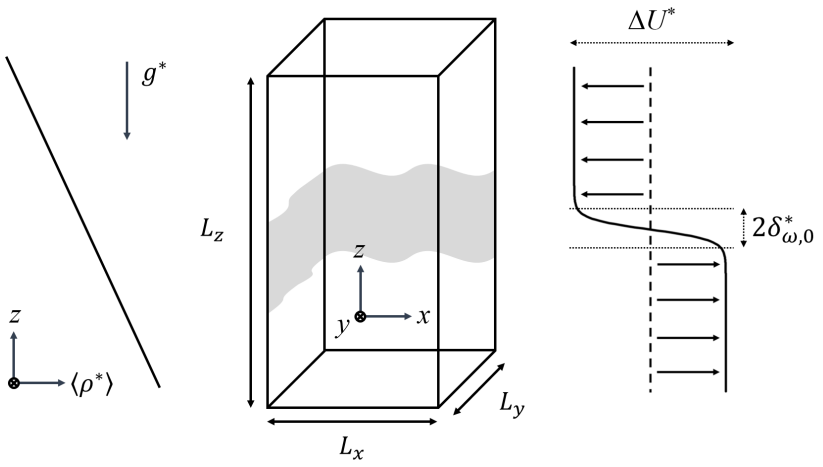

Figure 2.1: Sketch of the stratified shear layer with the velocity difference across the shear layer (ΔU^*), initial vorticity thickness of the shear layer ($\delta^*_{\omega,0}$), and initial density profile ($\langle\rho^*\rangle$) identified.

the value of $\rho^*_b(z^*=0)$. Therefore, the background buoyancy frequency of the ambient fluid (N_0^{*2}) has a constant value given by $N_0^{*2} = -(g^*/\rho^*_0)\,\mathrm{d}\rho^*_b/\mathrm{d}z^*$. Gravitational acceleration (g^*) acts in the vertical.

The governing equations for this problem are the three-dimensional Navier-Stokes equations for unsteady, incompressible flows with the Boussinesq treatment of density such that density variations are considered only where they contribute to a gravitational force. A Cartesian frame of reference is used to represent the streamwise, spanwise, and vertical coordinates such that spatial orientation and velocities are given by $x_i = (x,y,z)$ and $u_i = (u,v,w)$, respectively. These equations can be nondimensionalized using the following reference quantities: velocity difference across the shear layer (ΔU^*), initial vorticity thickness of the shear layer ($\delta^*_{\omega,0}$), and a reference value for

density deviation ($\Delta\rho^* = \delta^*_{\omega,0}\,\mathrm{d}\rho^*/\mathrm{d}z^*$). The resulting nondimensional equations are given by

$$\frac{\partial u_j}{\partial x_j} = 0\,, \tag{2.3a}$$

$$\frac{\partial u_i}{\partial t} + \frac{\partial (u_j u_i)}{\partial x_j} = -\frac{\partial p}{\partial x_i} + \frac{1}{Re_0}\frac{\partial^2 u_i}{\partial x_j \partial x_j} - Ri_0 \tilde{\rho} g_i\,, \tag{2.3b}$$

$$\frac{\partial \tilde{\rho}}{\partial t} + \frac{\partial (u_j \tilde{\rho})}{\partial x_j} = \frac{1}{Re_0 Pr}\frac{\partial^2 \tilde{\rho}}{\partial x_j \partial x_j} - w\frac{d\bar{\rho}}{dz}\,. \tag{2.3c}$$

Here, the density equation is solved for the nondimensional density deviation ($\tilde{\rho}$) from the uniform background. Nondimensional parameters, namely the initial Reynolds number (Re_0), initial gradient Richardson number at the center of the shear layer (Ri_0), and Prandtl number (Pr) are given by

$$Re_0 = \frac{\Delta U^* \delta^*_{\omega,0}}{\nu^*}\,, \quad Ri_0 = \frac{N_0^{*2}\delta^{*2}_{\omega,0}}{\Delta U^{*2}}\,, \quad Pr = \frac{\nu^*}{\kappa^*}\,. \tag{2.4}$$

Here, ν^* and κ^* are the kinematic viscosity and thermal diffusivity, respectively. The pressure (p) denotes deviation from the mean pressure in hydrostatic balance. The velocity and pressure fields are decomposed using Reynolds decomposition into mean and fluctuating components while density is composed of a constant reference density, a horizontally averaged mean component, and a fluctuating component. These decompositions are given by

$$u_i(x_i,t) = \langle u_i \rangle(x_i,t) + u_i'(x_i,t)\,, \tag{2.5a}$$

$$p(x_i,t) = \langle p \rangle(x_i,t) + p'(x_i,t)\,, \tag{2.5b}$$

$$\rho(x_i,t) = \rho_0 + \langle \rho \rangle(z,t) + \rho'(x_i,t)\,, \tag{2.5c}$$

where $\langle\rangle$ and $'$ indicate a mean and fluctuating value, respectively.

2.0.1.2 Numerical methods and simulation setup

The numerical methods employed to solve the governing equations are similar to DNS of previous works (Brucker & Sarkar, 2007; Pham *et al.*, 2009; Pham & Sarkar, 2010; VanDine *et al.*, 2018). A staggered grid approach wherein normal velocities are located at the cell faces while pressure and density are located at the cell center is used. The Williamson low-storage, third-order Runge Kutta method is employed for time advancement while discretization of spatial derivatives is achieved using a second-order, central finite difference scheme. The Poisson pressure equation is solved using a parallel multigrid solver and Red-Black Gauss-Seidel smoothing. Parallel computations and message-passing interface (MPI) are also utilized throughout the numerical scheme. In a sponge region near the vertical boundaries in the regions $z > 10$ and $z < 10$ (sufficiently far from the shear layer), a Rayleigh damping function gradually relaxes the density and velocities to their corresponding boundary values in order to damp propagating fluctuations and prevent reflections of features such as internal waves which have propagated far from the shear layer.

The flow is initialized using velocity perturbations for which the broadband spectrum is given by

$$E(k) \propto k^4 \exp\left[-2\left(\frac{k}{k_0}\right)^2\right], \tag{2.6}$$

where the peak spectrum is found at $k_0 = 1.1$, e.g. the fastest growing mode of the Kelvin-Helmholtz instability, and the initial velocity fluctuations have peak values at $0.1\%\ \Delta U$.

The streamwise and spanwise directions utilize periodic boundary conditions. In the vertical direction, vertical velocity uses a Dirichlet boundary condition while Neumann boundary conditions

are enforced for density, pressure, and the remaining velocities as follows:

$$\frac{\partial \tilde{\rho}}{\partial z}(-L_z/2) = \frac{\partial \tilde{\rho}}{\partial z}(L_z/2) = 0, \tag{2.7a}$$

$$\frac{\partial p}{\partial z}(-L_z/2) = \frac{\partial p}{\partial z}(L_z/2) = 0\,, \tag{2.7b}$$

$$\frac{\partial u}{\partial z}(-L_z/2) = \frac{\partial u}{\partial z}(L_z/2) = \frac{\partial v}{\partial z}(-L_z/2) = \frac{\partial v}{\partial z}(L_z/2) = 0\,, \tag{2.7c}$$

$$w(-L_z/2) = w(L_z/2) = 0\,. \tag{2.7d}$$

For this work, an isotropic grid is used in the central region of the shear layer with grid spacing of $\Delta x = \Delta y = \Delta 0.0074\,\delta_{\omega,0}$. The streamwise and spanwise grids have uniform spacing while mild stretching is used in the vertical outside the region $|z| < 2.5$. Throughout the entire grid, this grid spacing is less than 2.75η where $\eta = (\nu^3/\varepsilon)^{1/4}$ (ε denotes turbulent kinetic energy dissipation rate) is the Kolmogorov length scale thus indicating appropriate resolution for capturing small-scale fluctuations. The number of grid points in the streamwise, spanwise, and vertical directions are given by $(N_x, N_y, N_z) = (1536, 768, 1024)$ such that the domain extent is $(L_x, L_y, L_z) \approx (11\,\delta_{\omega,0}, 5.7\,\delta_{\omega,0}, 32\,\delta_{\omega,0})$.

Four DNS cases are presented herein. All cases have $Re_0 = 24{,}000$ and $Pr = 1$ while the strength of stratification is varied such that $Ri_0 = [0.04, 0.08, 0.12, 0.16]$ encompasses a range of fluid types from weakly stratified at $Ri_0 = 0.04$ to strongly stratified at $Ri_0 = 0.16$. It should be noted that the value of $Pr = 1$ is chosen as in a number of other studies so that the scalar field does not require finer resolution than the velocity field. For the remainder of this work, Ri will be used in lieu of Ri_0.

2.0.1.3 Statistical analysis

In later discussions, both two-dimensional (K_{2d}) and three-dimensional (K) turbulent kinetic energy (TKE) are evaluated where each is defined as

$$K_{2d} = \frac{1}{2}\left(\langle u' \rangle^2 + \langle w' \rangle^2\right), \quad K = K_{2d} + \frac{1}{2}\langle v' \rangle^2 . \tag{2.8}$$

The TKE budget will be used to examine the routes to turbulence and is given by

$$\frac{\mathrm{D}K}{\mathrm{D}t} = \mathrm{P} - \varepsilon + \mathrm{B} - \frac{\mathrm{d}\mathrm{T}_3}{\mathrm{d}z}, \tag{2.9}$$

with production (P), dissipation (ε), buoyancy flux (B), and the transport term (T_3) specified as

$$\begin{aligned} &\mathrm{P} = -\langle u'w' \rangle \tfrac{\mathrm{d}\langle u \rangle}{\mathrm{d}z}, \quad \varepsilon = \tfrac{2}{Re_0}\langle s'_{ij} s'_{ij} \rangle, \quad s'_{ij} = \tfrac{1}{2}\left(\tfrac{\partial u'_i}{\partial x_j} + \tfrac{\partial u'_j}{\partial x_i}\right), \\ &\mathrm{B} = -Ri_0 \langle \rho' w' \rangle, \quad \mathrm{T}_3 = \tfrac{1}{2}\langle w' u'_i u'_i \rangle + \tfrac{1}{\rho_0}\langle w' p' \rangle - \tfrac{2}{Re_0}\langle u'_i s'_{3i} \rangle . \end{aligned} \tag{2.10}$$

In order to calculate mixing efficiency, Mashayek & Peltier (2013) computed the change in background potential energy by sorting the density field. Instead, we use the dissipation of the density field as a surrogate to the change in background potential energy such that the mixing efficiency (Γ) is given by

$$\Gamma = \frac{\varepsilon_\rho}{\varepsilon + \varepsilon_\rho}, \quad \varepsilon_\rho = \frac{1}{Re_0 Pr}\frac{g^2}{\rho_0^2 N_0^2}\left\langle \frac{\partial \rho'}{\partial x_i}\frac{\partial \rho'}{\partial x_i} \right\rangle, \tag{2.11}$$

where ε_ρ is the dissipation rate of the potential energy.

2.0.2 Flow evolution

2.0.2.1 Linear stability analysis of Kelvin-Helmholtz shear instability

We first examine the effect of stratification on the growth rate of the KH shear instability using linear stability analysis (LSA). The LSA of a stratified shear layer with a two-layer density profile indicates that the shear instability develops when $Ri < 0.25$. The growth rate (σ) of the fastest growing mode (FGM) reduces significantly as Ri increases toward 0.25 (Hazel, 1972). This analysis assumes that the fluid is inviscid and the shear layer is located inside an infinite domain.

Here, LSA is performed, taking into account the effect of viscosity, diffusivity, and a finite domain, to examine the FGM when the shear layer is uniformly stratified. The theory and numerical implementation of the LSA is given in Smyth *et al.* (2011). In the LSA, the Reynolds number, the Prandtl numbers, and domain size (L_z) have the same values as in the DNS. The grid spacing is $\Delta z = 0.1$. Free-slip and fixed buoyancy conditions are used at the top and bottom boundaries. The LSA of the two-layer profile is also performed for comparison.

Figure 2.2(a,b) contrasts the mean profiles of the squared buoyancy frequency (N^2), squared rate of shear (S^2), and gradient Richardson number (Ri_g) in the two-layer shear layer to those in the linearly stratified shear layer. The same level of stratification at the center of the shear layer, $N^2 = 0.12$, is used. Away from the center, N^2 decreases to zero in the two-layer case while it remains constant in the other case. As a result, the Ri_g in the two layer case is smaller than that in the case with linear stratification throughout the shear layer except at the center where $Ri_g = 0.12$ in the both cases. With the same amount of mean kinetic energy, e.g. the same velocity profile, the potential energy barrier inside the shear layer is significantly higher in the case with linear stratification, thereby inhibiting the growth of the KH shear instability.

Results of the LSA are shown in figure 2.2(c,d). In the two-layer case, the growth rate (σ) is similar to that of Hazel (1972) in the region with low k and Ri. However, as k and Ri increase, the growth rate becomes smaller than the value from Hazel (1972) due to the effect of viscosity, diffusivity, and a finite domain. The FGM at various Ri, marked by the white line, suggests that the

critical Richardson number for the two-layer case is 0.18. At higher stratification, the growth rate of the KH mode is still positive. However, there exist higher modes with faster growth rate. In the case of uniform stratification, the critical Richardson number for the KH mode becomes smaller, approximately 0.15.

Figure 2.2(e,f) contrasts how the growth rate varies with wavenumber between the two cases for five values of Ri. At the same Ri, the growth rate of the KH mode is higher in the two-layer case which suggests that the KH shear instability in the case with uniform stratification would be weaker. In the case with uniform stratification, when $Ri = 0.16$, the KH shear instability is not the FGM, but the growth rate is still positive so the instability develops as will be examined later.

In the cases with weaker stratification, e.g. $Ri < 0.18$, the KH shear instability develops but does not excite propagating internal waves. The KH mode perturbs the pressure field in the region above and below the shear layer, but the perturbation decays exponentially with the distance away from the shear layer as evanescent waves. Pham *et al.* (2009) also suggest that turbulence also can excite propagating internal waves which are significantly weaker than those excited by the KH instability. In the present study, turbulence also excites internal waves in the cases with $Ri < 0.18$. The characteristics of the turbulence-generated internal waves will be addressed in a later section.

2.0.2.2 Routes to turbulence: Kelvin-Helmholtz shear instability and secondary instabilities

In a stratified shear layer with large Re, it is understood that there is a strong primary instability in the form of a Kelvin-Helmholtz (KH) shear instability. This instability manifests as a series of vortices which roll up over time (termed billows) and are connected by vorticity filaments (termed braids). As the KH billows evolve, secondary instabilities develop throughout the shear layer. Mashayek & Peltier (2012*b*) provide a compilation of such secondary instabilities, of which, secondary shear instabilities (SSI), stagnation point instabilities (SPI), secondary convective instabilities (SCI), secondary core deformation instabilities (SCDI), secondary vorticity bands instabilities (SVBI), and localized core vortex instabilities (LCVI) are also identifiable in the results presented herein. SSI, SCI, and SCDI are typically categorized as early-time secondary instabilities

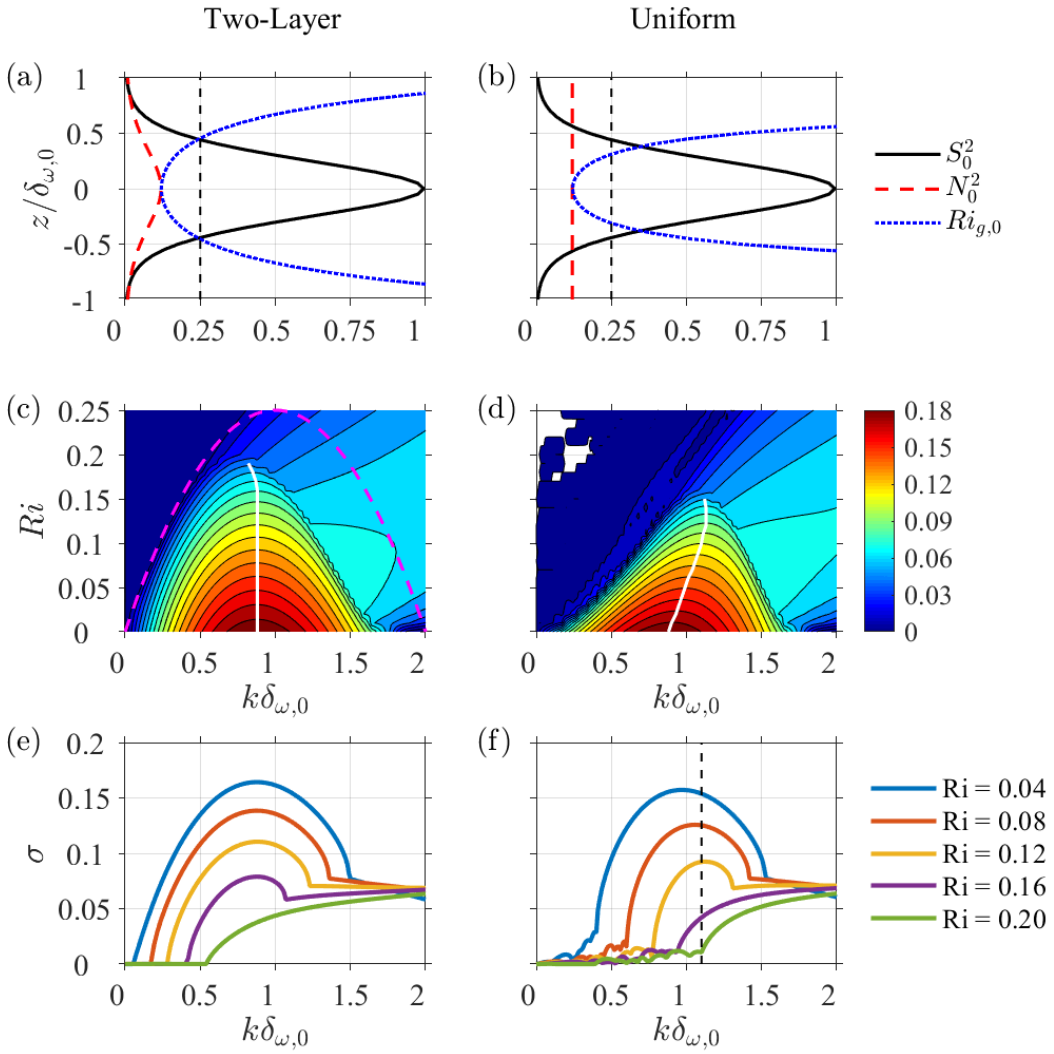

Figure 2.2: Effect of stratification on the KH shear instability using linear stability analysis (LSA) giving (a,b) mean initial profiles of the squared shear rate (S^2), squared buoyancy frequency (N^2), and gradient Richardson number (Ri_g) as well as (c,d) contours of growth rate (σ) at various Richardson numbers (Ri) and wave number (k). The variability of the growth rate with wave number at fixed Richardson numbers is shown in (e,f). Results in (a,c,e) are from the two-layer density profile while those in (b,d,f) are from the linear density profile. In (c), a dashed magenta line marks the stability boundary, $Ri = k(1-k)$ where k is the non-dimensional wavenumber (Hazel, 1972). Solid white lines in (c,d) indicate the FGM. The dashed black line in (f) marks the modes used to excite the KH shear instability in the present study.

whereas SPI, LCVI, and SVBI are associated with late-time shear layer evolution (Mashayek & Peltier, 2012*b*). The appearance and behavior of these instabilities varies with background stratification (as will be discussed later) but a brief explanation of each follows from Mashayek & Peltier (2012*a*,*b*); Arratia (2011); Arratia *et al.* (2013); Salehipour *et al.* (2015).

As KH billows roll up, they extract kinetic energy from the shear layer and transfer it to available potential energy as they grow vertically. SCI form as convectively unstable regions appear inside the billow during this roll-up. Mashayek & Peltier (2012*b*) see increasing growth rates of these instabilities between $0.04 \leq Ri \leq 0.12$ due to increasing density gradients across the unstable regions. However, SCI are suppressed at higher values of Ri due to decreased growth of the KH billow and weaker overturning associated with higher stratification. SSI develop along the braids between billows due to velocity shear along the filament. The strain field is shown to suppress the instability and, as such, SSI develop in areas of relatively weak strain and diminish under the influence of high strain. Mashayek & Peltier (2012*b*) saw enhanced SSI with increasing Ri until $Ri = 0.12$, at which point, the growth of SSI is diminished due to a stronger strain field induced by core growth. SCDI form in regions nearly parallel to the braid inside the KH billow core. As their presence is responsible for an observable inflation of the core itself, it is more prevalent in less stratified flows. As Ri increases, the vortex core becomes smaller due to the enhanced stratification and SCDI are suppressed.

The core vortex bands become sufficiently close to the braid as KH billows develop causing perturbations from which a SPI emerges. Mashayek & Peltier (2012*b*) observe the growth rate of SPI to increase between $0.04 \leq Ri \leq 0.12$ and decrease at higher values of Ri. They also note that SPI developed high growth rates at large wavenumbers. As the core vortex bands grow and achieve sufficiently large magnitude, counter-clockwise vortices (LCVI) form at the tips of the negative vorticity bands within the core. The appearance of LCVI is particularly apparent at high Re because the KH billows roll up faster and there is less time for the vorticity bands in the core to diffuse. Mashayek & Peltier (2012*b*) assert that both SPI and LCVI could trigger SSI by inducing braid deformation. The interaction of SPI and LCVI near the braid are responsible for the generation of

SVBI.

The elliptical instability characterized by Arratia (2011) and Arratia *et al.* (2013) and the eyelid instability described by Salehipour *et al.* (2015) are also observed in this work. The eyelid is distinguished as the region surrounding the core of the KH billow. Flow instabilities are largely responsible for momentum transport from the center of the shear layer towards the periphery as well as the development and evolution of the transition layer which will be discussed later. A discussion of the instabilities relevant to the cases in this work follows.

The $Ri = 0.04$ case is used to outline the general development of the stratified shear layer while differences between the various Ri cases are discussed thereafter. Figures 2.3 and 2.4 show cross-sectional snapshots at early times of the density (ρ), spanwise vorticity ($\omega_2 = \partial u/\partial z - \partial w/\partial x$), and dissipation rate (ε). The creation of the primary shear instability is clearly illustrated in figure 2.3 in the form of two KH billows. As the billows grow vertically, they extract kinetic energy from the shear layer. At their maximum vertical extent, the billows contract vertically. As seen in figure 2.4, in the $Ri = 0.04$ case, the primary KH instabilities deform into elliptical instabilities similar to those described at length by Arratia (2011). A spanwise instability visualized in figure 2.4 is also generated which further disrupts the flow. The billow continues to develop lateral motions and *r.m.s.* spanwise velocity fluctuations (not shown) increase in this case. Note that there is no broadband turbulence as yet in the development. As small-scale fluctuations are allowed to develop due to low viscosity (high Re), the billows begin to break down with turbulent motions concentrated in the core of the billow. Due to the weak stratification, this case is dominated by core-centered vortices and SCI caused by the convectively unstable regions within the billow. As SCI develop, SCDI are observed inside the billows as evidenced in figure 2.5 by the region of elevated positive vorticity and strong dissipation rate near the lower core periphery of the central billow. Eventually, the breaking billows become localized turbulent patches with the majority of overturning occurring at the core of each billow.

As seen in figure 2.6, the flow evolves similarly in the $Ri = 0.08$ case with the KH billows exhibiting vertical growth followed by contraction which is accompanied by lateral motions and

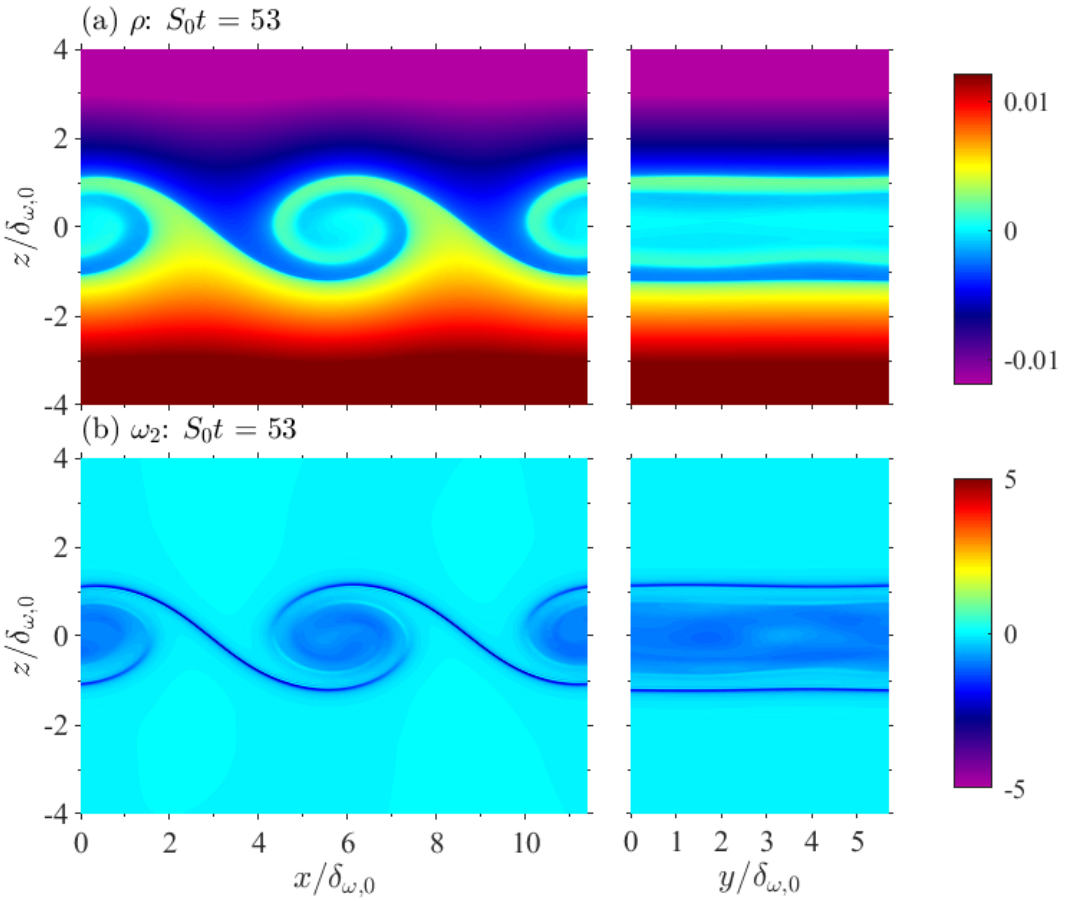

Figure 2.3: Cross-sectional snapshots of the (a) density (ρ) and (b) spanwise vorticity (ω_2) fields for the $Ri = 0.04$ case at $S_0t = 53$. For this and future similar plots, the $y/\delta_{\omega,0}$ - $z/\delta_{\omega,0}$ and $x/\delta_{\omega,0}$ - $z/\delta_{\omega,0}$ planes are extracted at the centerline streamwise and spanwise locations where $x/\delta_{\omega,0} = 5.7$ and $y/\delta_{\omega,0} = 0$, respectively.

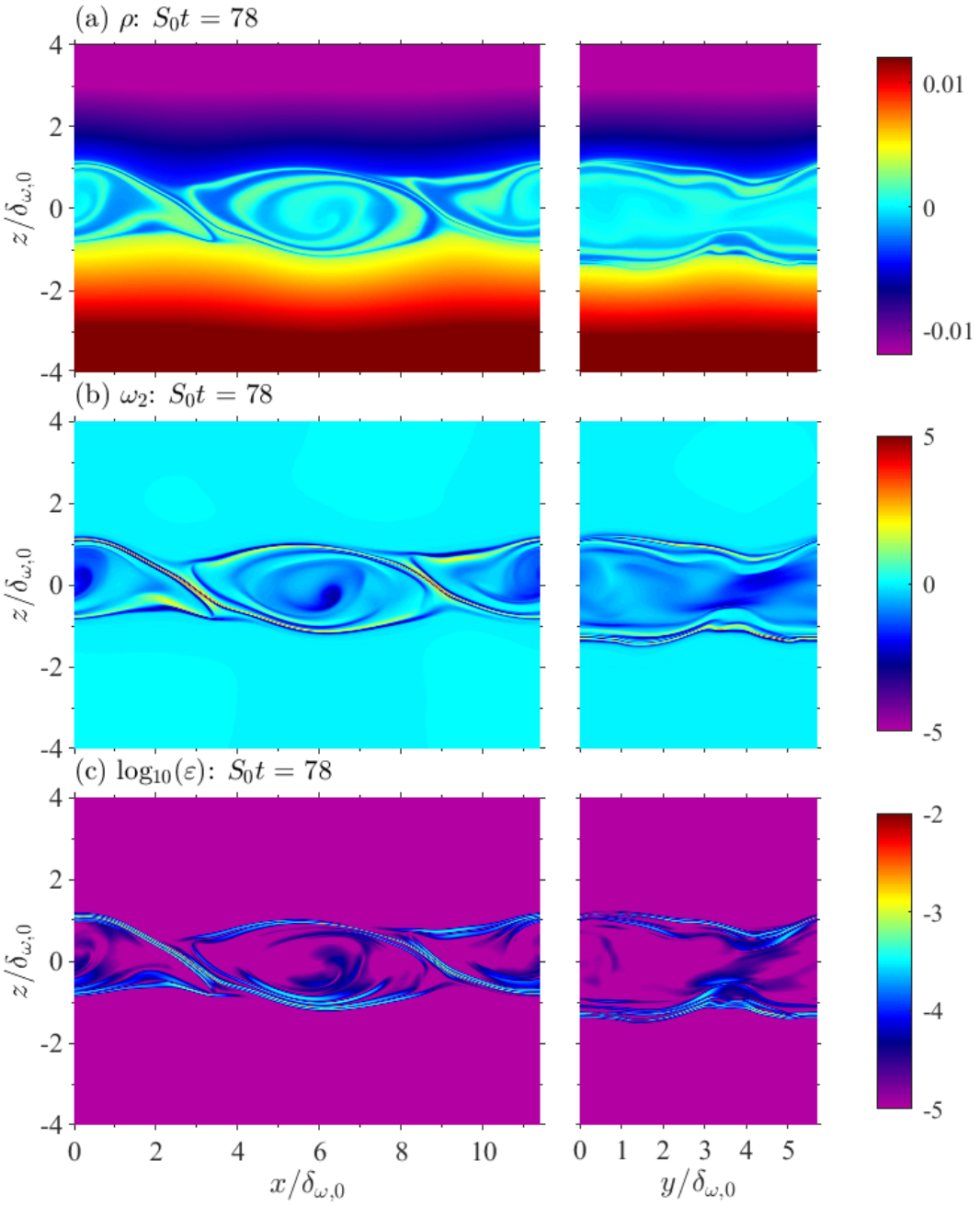

Figure 2.4: Cross-sectional snapshots of the (a) density (ρ), (b) spanwise vorticity (ω_2), and (c) dissipation rate (ε) fields for the $Ri = 0.04$ case at $S_0t = 78$.

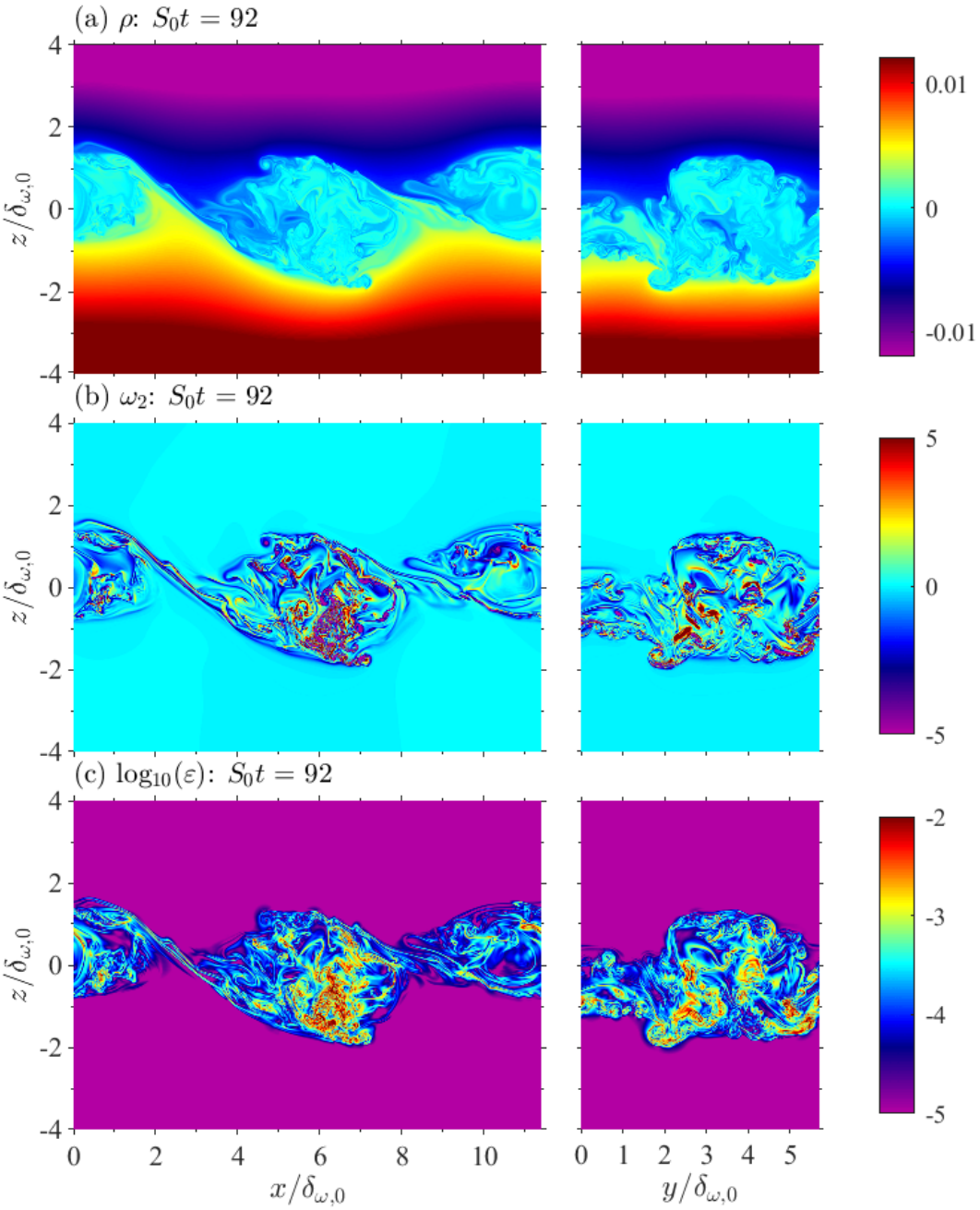

Figure 2.5: Cross-sectional snapshots of the (a) density (ρ), (b) spanwise vorticity (ω_2), and (c) dissipation rate (ε) fields for the $Ri = 0.04$ case at $S_0t = 92$.

deformation into elliptical billows. However, in this case, the increased effect of buoyancy prevents the extent of the lateral motion observed in the $Ri = 0.04$ case. Instead, the billows experience shorter vertical contraction and weaker lateral motions. The billows first begin to break down in the lower periphery of the billow in the form of an eyelid instability from which SCI are generated by convectively unstable regions. The spanwise snapshots show the emergence of SCI in the eyelid rather than in the core of the billow as seen in figure 2.6(b). The $y/\delta_{\omega,0}$ - $z/\delta_{\omega,0}$ planes in this figure reveal much more coherent behavior at the edges of the shear layer than in the $Ri = 0.04$ case with secondary instabilities clearly observed and little turbulence noted at the billow core. Eventually, patches of turbulence develop with elevated turbulence along the braids where weak SSI evolve due to weakening strain and strengthening shear.

The $Ri = 0.12$ case is particularly interesting. In this case, more obvious differences are observed in the evolution of the flow and instabilities as compared to the low *Ri* cases. The effect of buoyancy inhibits large vertical growth of the billows, thereby preventing the elliptical instabilities caused by the collapse and redistribution of the billow. Figure 2.7 depicts the density, spanwise vorticity, and TKE dissipation rate fields at $S_0 t = 101$ for the $Ri = 0.12$ case. As the primary KH instability grows, a number of distinct secondary instabilities are observed. Eyelid instabilities which prompt SCI near the peripheries of the billow are stronger than in the weakly stratified cases due to the stronger density deviation across the core and unstable regions. Localized weak strain promotes the development of SSI and their propagation along the braids (not shown). An SPI for which dissipation rate is strong and vorticity is strongly negative is identifiable on the braid of the billow in figure 2.7 due to the destabilizing interaction of the core vortex bands with the stagnation point. Near the connection of the braids with the eyelid of the billow where the influence of the internal vorticity bands is strong, LCVI are seen to form as counter-clockwise vortices. The appearance of LCVI is more prolific in this investigation than in other works due to the increased *Re*, at which, the KH billows roll up faster, reducing the time available for vorticity bands to diffuse. SVBI are observed along the braids as SPI and LCVI interact (not shown). Overall, turbulence is strongly isolated to the edges of the billows in the form of these instabilities.

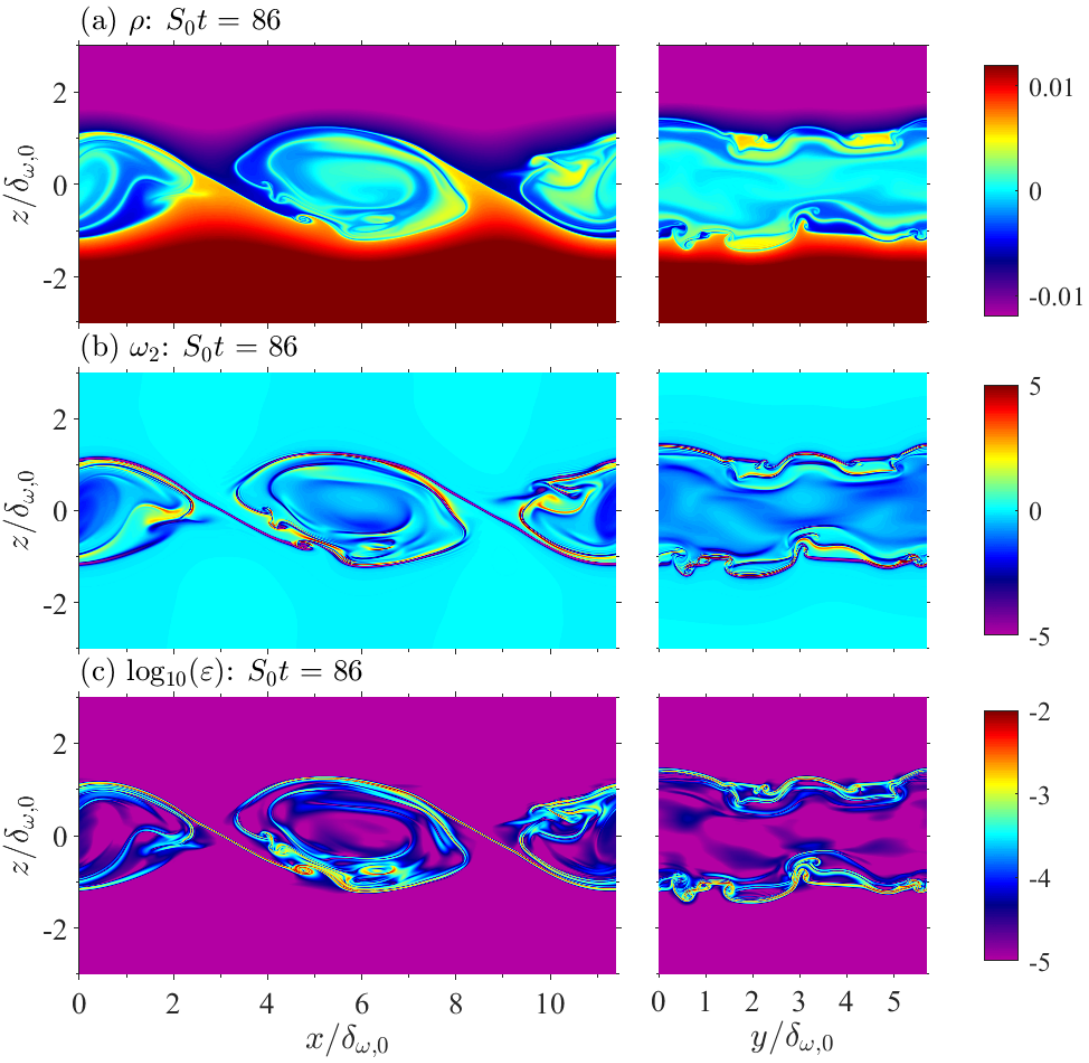

Figure 2.6: Cross-sectional snapshots of the (a) density (ρ), (b) spanwise vorticity (ω_2), and (c) dissipation rate (ε) fields for the $Ri = 0.08$ case at $S_0t = 86$.

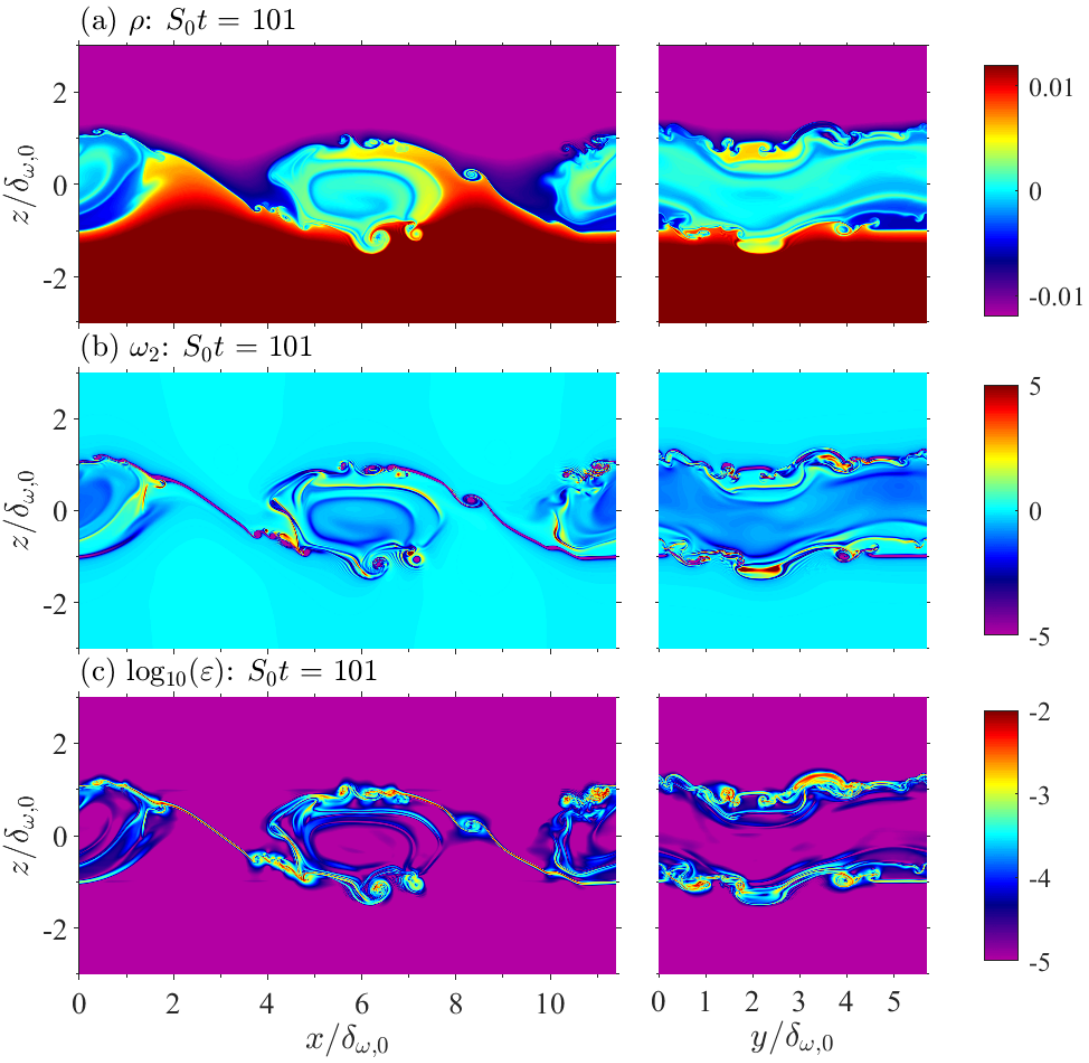

Figure 2.7: Cross-sectional snapshots of the (a) density (ρ), (b) spanwise vorticity (ω_2), and (c) dissipation rate (ε) fields for the $Ri = 0.12$ case at $S_0t = 101$.

At early time in the $Ri = 0.16$ case, the primary KH instability develops (not shown) although not to the same vertical height as in the low Ri cases due to the suppressing influence of buoyancy in the highly stratified environment. By the same mechanisms described in the $Ri = 0.12$ discussion, secondary instabilities take the form of eyelid, SCI, SSI, SPI, LCVI, and SVBI. Eyelid instabilities are clearly seen in the billow periphery in figure 2.8. Strong mushroom-like instabilities (alluded to as secondary convective instabilities (SCI) in Mashayek & Peltier (2012*b*)) are observed to propagate from the eyelid in the spanwise plane at locations near the edges of the shear layer in the $x/\delta_{\omega,0}$ - $z/\delta_{\omega,0}$ planes of figure 2.8 at $S_0 t = 138$. These regions show elevated positive spanwise vorticity and high rates of TKE dissipation and grow in vertical extent until the entirety of the shear layer in the spanwise is disturbed. As such, they are highly influential in the breakdown of billows. Unlike in the $Ri = 0.12$ case in which a SPI appears followed by SVBI, two distinct SVBI are seen to form (see the location of elevated vorticity and dissipation rate in figure 2.8) and propagate along the braid before a SPI is observed (see figure 2.9). As in the $Ri = 0.12$ case, LCVI appear, leading to braid deformation and the appearance of secondary shear vortices (and therefore, late-time SSI) on the braid. In this case, there are only weak SCDI (see the right side of the central billow core in figure 2.9) due to the enhanced stratification and smaller vortex core sizes. As in the $Ri = 0.12$ case, edge breaking is noted such that turbulence is concentrated away from the center of the shear layer as the flow becomes fully turbulent.

2.0.2.3 Effect of stratification on the growth of the shear layers

The growth of the shear layer can be quantified using the momentum thickness which is defined by

$$I_u = \int_{-5}^{5} \left[1 - 4\langle u \rangle^2\right] \mathrm{d}z\,. \tag{2.12}$$

Figure 2.10(a) compares the temporal evolution of the normalized momentum thickness ($I_u/I_{u,0}$) for all Ri and a number of distinct flow regimes are identified. At early time, (approximately $30 < S_0 t < 60$ in the $Ri = 0.04$ case, $40 < S_0 t < 70$ in the $Ri = 0.08$ case, and $50 < S_0 t < 90$ in the $Ri = 0.12$ case), the shear layer thickens rapidly due to the growth of the KH shear instability. In

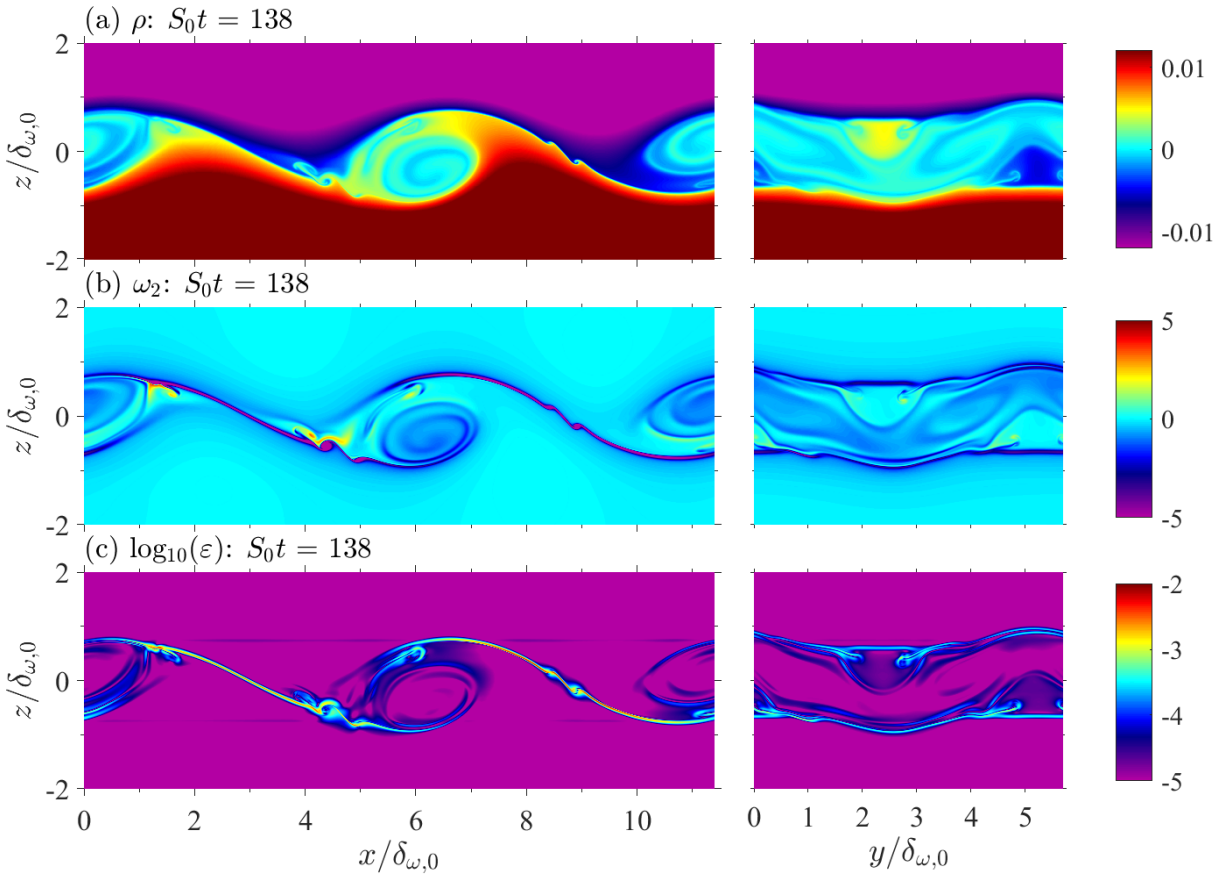

Figure 2.8: Cross-sectional snapshots of the (a) density (ρ), (b) spanwise vorticity (ω_2), and (c) dissipation rate (ε) fields for the $Ri = 0.16$ case at $S_0t = 138$.

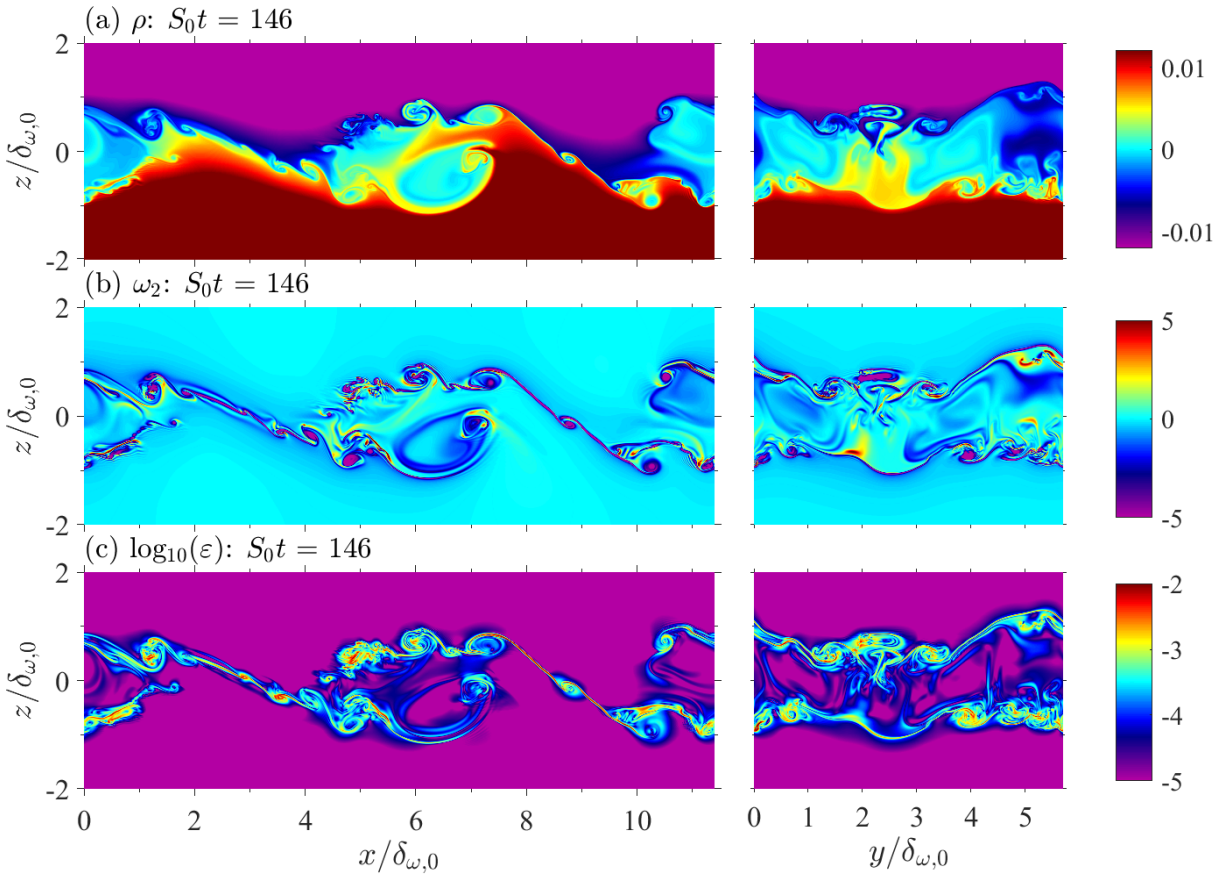

Figure 2.9: Cross-sectional snapshots of the (a) density (ρ), (b) spanwise vorticity (ω_2), and (c) dissipation rate (ε) fields for the $Ri = 0.16$ case at $S_0t = 146$.

all cases, except for the $Ri = 0.16$ case, there is a period where the shear layer briefly shrinks or stops growing before beginning to grow once again (approximately $60 < S_0t < 80$ in the $Ri = 0.04$ case, $70 < S_0t < 90$ in the $Ri = 0.08$ case, and $90 < S_0t < 100$ in the $Ri = 0.12$ case). In the case of $Ri = 0.12$, the layer does not contract significantly as in the $Ri = 0.04$ and $Ri = 0.08$ cases but there is stagnation in shear layer growth. The contraction of the shear layer persists longer with smaller values of Ri and is not seen at all in the $Ri = 0.16$ case indicating that stratification plays a key roll in this flow feature.

The period of contraction occurs during the transition regime from flow dominated by two-dimensional KH rollers to fully three-dimensional turbulence. Figures 2.10(b-e) illustrate the evolution of two-dimensional TKE (K_{2d}) and three-dimensional TKE (K) as defined in equation 2.8. The terms are vertically integrated across the shear layer in the region bounded by $|z| < 5$. When K is larger than K_{2d} by 1% (marked as t_{2d}), the KH rollers begin to transition into turbulence. Turbulence in the shear layer becomes fully developed when K reaches its maximum value denoted as t_{3d} in figures 2.10(b-e). It is clear that the contraction of the shear layer occurs between t_{2d} and t_{3d}. After the growth stagnation and contraction, the shear layer thickness resumes growing until reaching $S_0t \approx 150$ in all cases except the $Ri = 0.16$ case which plateaus at $S_0t \approx 180$. At this time, buoyancy effects become sufficiently strong to cause turbulence decay and the shear layer can no longer thicken. In the $Ri = 0.04$ case, a second period of contraction is noted after reaching maximum momentum thickness at $S_0t \approx 150$. Overall, the rate of growth decreases with increasing Ri and the ultimate thickness of the shear layer is much smaller. The $Ri = 0.04$ case shows an eventual normalized momentum thickness of approximately 3.5 while the $Ri = 0.16$ case barely reaches 1.8 indicating a much more vertically confined shear layer in the higher Ri case.

Snapshots of the density field are shown in figure 2.11 at times before ($S_0t = 53$), during ($S_0t = 73$), and after ($S_0t = 81$) the first contraction. As previously discussed, the primary KH instability grows vertically until the potential energy barrier becomes too large, at which point, the billow contracts vertically and expands horizontally in the streamwise direction. The deformation of the billows occurs coherently without inciting broadband turbulence. The change in vertical extent

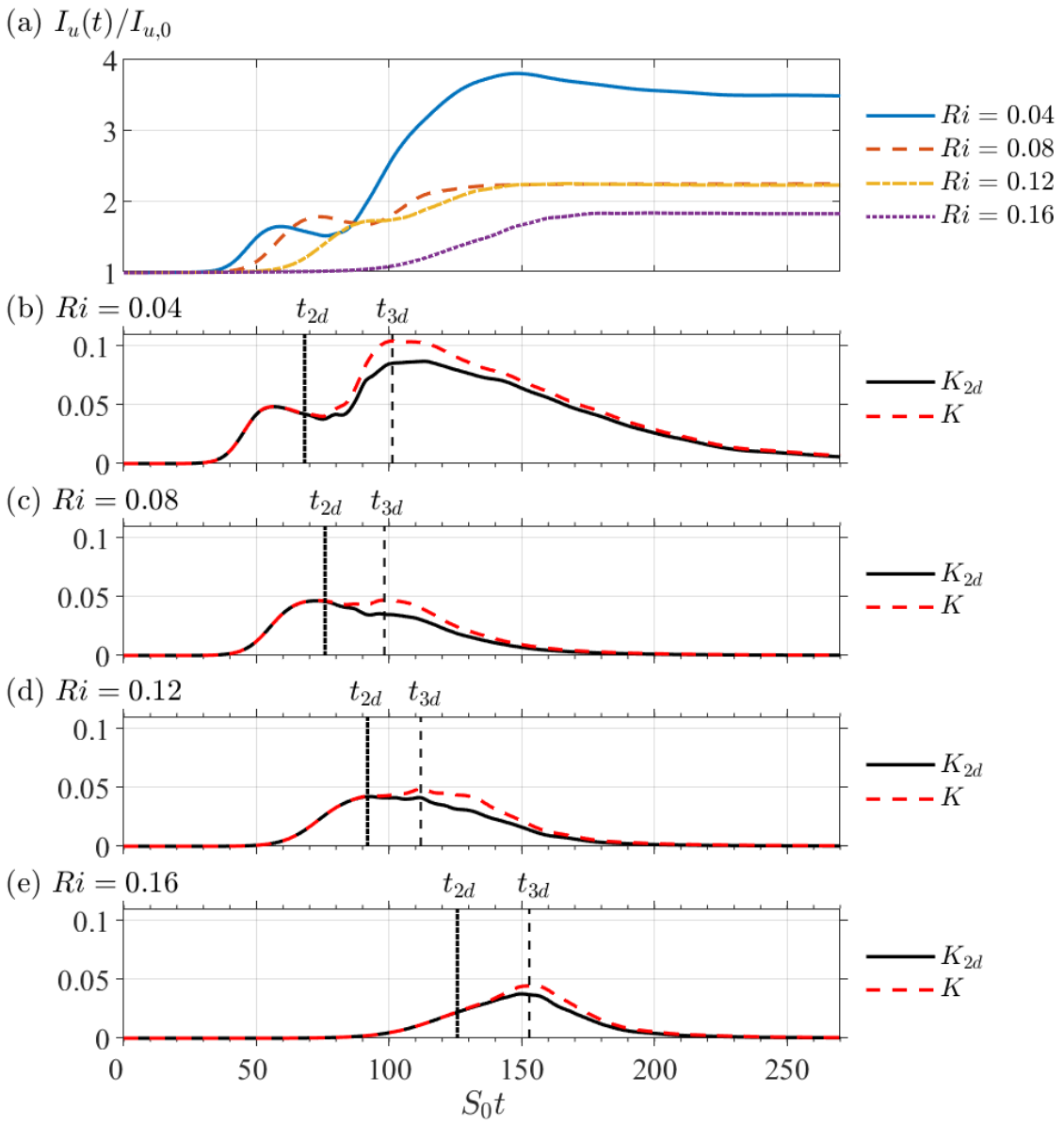

Figure 2.10: $S_0 t$ evolution of the (a) normalized momentum thickness ($I_u/I_{u,0}$) and (b-e) integrated two-dimensional and three-dimensional turbulent kinetic energy in the (b) $Ri = 0.04$, (c) $Ri = 0.08$, (d) $Ri = 0.12$, and (e) $Ri = 0.16$ cases. Integration is performed between $z = \pm 5$. Dotted lines in (b-e) mark the transition from two-dimensional KH billows to three-dimensional turbulence while dashed lines denotes the time of peak three-dimensional TKE.

is clear between figures 2.11(a) and 2.11(b). The development of subsequent spanwise instabilities visible in figures 2.11(b,c) break down the billows. The $y/\delta_{\omega,0}$ - $z/\delta_{\omega,0}$ snapshot in figure 2.11(d) shows a mushroom-like structure at $y/\delta_{\omega,0} = 1.5$ in the core of the billow suggesting that a SCI is responsible for the transition to fully three-dimensional turbulence in the shear layer during the period of contraction.

The contraction of the shear layer influences the energetics of turbulence since the evolution of the momentum thickness is directly related to the mean kinetic energy (MKE) defined as $\bar{K} = \frac{1}{2}\langle u \rangle^2$. Therefore, the change in momentum thickness is given by

$$\frac{\mathrm{d}I_u}{\mathrm{d}t} = \int_{-5}^{5} -8\,\frac{\partial \bar{K}}{\partial t}\mathrm{d}z. \tag{2.13}$$

From the Navier-Stokes equation, the evolution of MKE can be obtained as follows:

$$\frac{\mathrm{D}\bar{K}}{\mathrm{D}t} = -\mathrm{P} - \bar{\varepsilon} - \frac{\partial \bar{\mathrm{T}}_3}{\partial z}, \tag{2.14}$$

with turbulent production (P), viscous dissipation ($\bar{\varepsilon}$), and transport term ($\bar{\mathrm{T}}_3$) specified as

$$\mathrm{P} = -\langle u'w' \rangle \frac{\partial \langle u \rangle}{\partial z}, \quad \bar{\varepsilon} = \frac{1}{Re_0}\left(\frac{\partial \langle u \rangle}{\partial z}\right)^2, \quad \text{and} \quad \bar{\mathrm{T}}_3 = \langle u \rangle \langle u'w' \rangle - \frac{1}{Re_0}\langle u \rangle \frac{\partial \langle u \rangle}{\partial z}.$$

Equations 2.13 and 2.14 are combined to yield

$$\frac{\mathrm{d}I_u}{\mathrm{d}t} = \int_{-5}^{5} -8\,\frac{\partial \bar{K}}{\partial t}\,\mathrm{d}z \approx \int_{-5}^{5} 8\,\mathrm{P}\,\mathrm{d}z, \tag{2.15}$$

where the small contribution of the viscous dissipation of MKE inside the shear layer as well as the small transport term at $z = \pm 5$ have been neglected. Equation 2.15 indicates that, when the shear layer contracts, e.g. $\mathrm{d}I_u/\mathrm{d}t < 0$, the integrated turbulent production becomes negative and MKE (integrated across the shear layer) increases.

During the contraction of the shear layer, MKE increases due to negative production and the

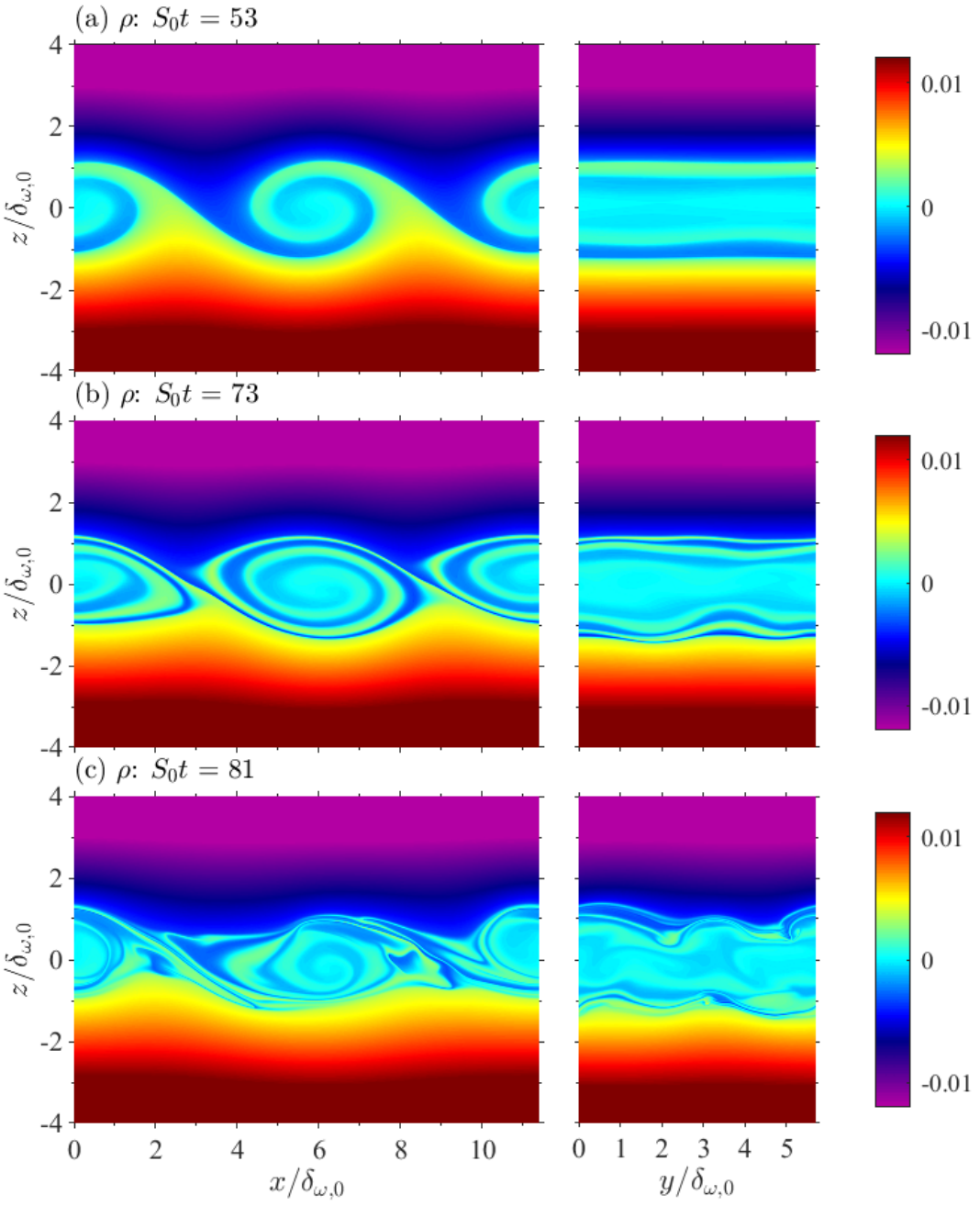

Figure 2.11: Cross-sectional snapshots of the density (ρ) field for the $Ri = 0.04$ case at various times: (a) $S_0t = 53$, (b) $S_0t = 73$, and (c) $S_0t = 81$. The $x/\delta_{\omega,0}$ - $z/\delta_{\omega,0}$ and $y/\delta_{\omega,0}$ - $z/\delta_{\omega,0}$ planes are extracted at the centerline spanwise and streamwise locations where $y/\delta_{\omega,0} = 0$ and $x/\delta_{\omega,0} = 5.7$, respectively.

decrease in potential energy. Figure 2.12(a) shows the evolution of the density deviation from the initial linear profile. As the KH billows develop, they transport heavy fluid upward and light fluid downward which stirs the density gradient. Consequently, density increases in the upper half of the shear layer while it decreases in the lower half. As the shear layer contracts, the density in the upper half of the shear layer decreases releasing the available potential energy that was previously gained. The density flux, which is positive during the growth of the KH billow, changes sign during the contraction suggesting the buoyancy flux becomes a source of TKE at this time (see figure 2.12(b)). The increase in the MKE can be seen in 2.12(c) which illustrates how the streamwise velocity ($\langle u \rangle$) deviates from the initial values during the contraction. Before the contraction, as the KH billows form, the velocity deviation increases in the upper half of the shear layer and decreases in the lower half. Recalling that the streamwise velocity is negative in the upper half and positive in lower half, the magnitude of the velocity decreases in both layers during the growth of the billows. As the billows contract, the magnitude of the velocity deviation decreases throughout the shear layer, and therefore, the velocity magnitude increases. The shear layer accelerates and MKE increases during the contraction period. A change in sign during the contraction period is also observed in the Reynolds stress, $\langle u'w' \rangle$ as shown in figure 2.12(d). Since the shear ($\partial \langle u \rangle / \partial z$) remains negative across the shear layer throughout the contraction period, the turbulent production changes sign. Before and after the contraction, shear production is a source of TKE while it is a source of MKE during the contraction. The negative $\langle u'w' \rangle$ and, therefore, the negative production are consistent with the relationship derived in equation 2.15.

To better understand the change in density flux during the contraction period, figure 2.13 compares snapshots of the flux during the contraction. Before the contraction, the density flux is negative in the braid region and in the billow core while positive density flux occupies the periphery of the billows. When averaged over the horizontal plane, the net density flux ($\langle \rho' w' \rangle$) is positive as shown in figure 2.13(a). As the KH billows deform during the contraction, the region with positive density flux becomes thinner while the peak positive value becomes significantly smaller. As a result, the horizontal average becomes negative near the center of the shear layer as shown in figure

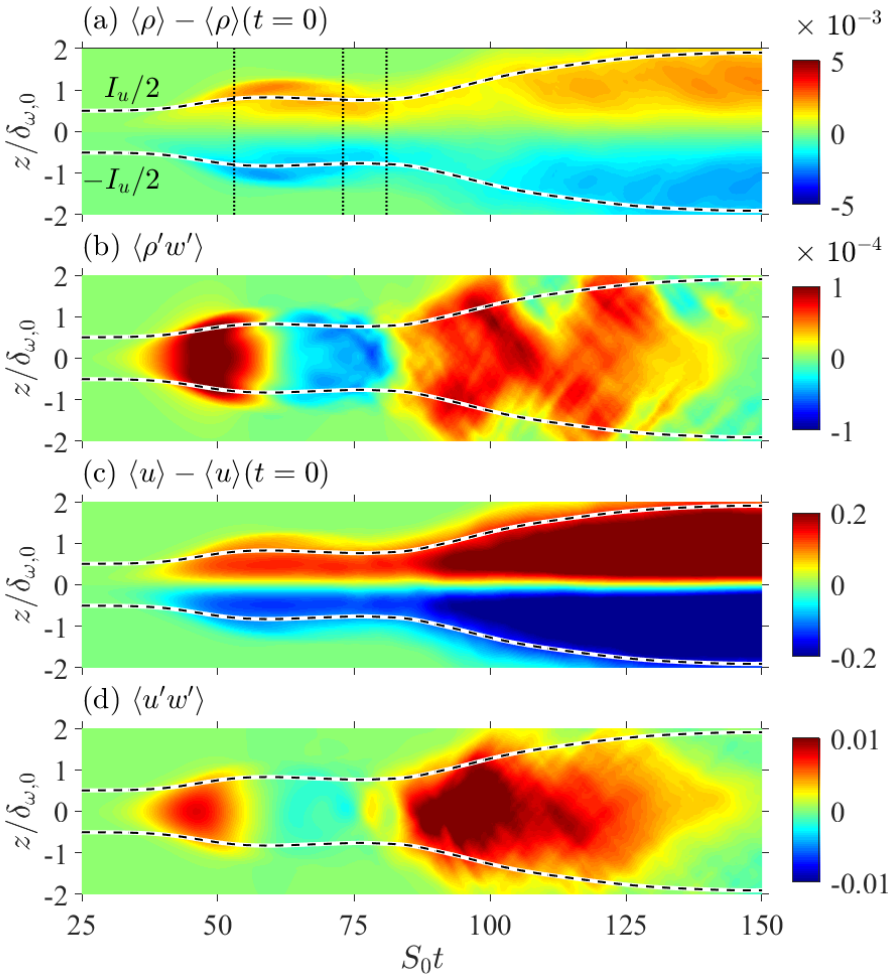

Figure 2.12: Evolution of the (a) density deviation from the initial profile ($\langle\rho\rangle - \langle\rho\rangle(t=0)$), (b) density flux ($\langle\rho' w'\rangle$), (c) Reynolds stress ($\langle u' w'\rangle$), and (d) buoyancy frequency (N^2) for the $Ri = 0.04$ case. Dashed lines in (a) marked the boundaries of the shear layer defined as $z = \pm I_u/2$. Vertical dotted lines denotes the three times at which snapshots of the KH billows are shown in figure 2.11. White regions in (d) denote $N^2 < 0$.

2.13(b,c). It is noted that a negative density flux gives rise to a positive buoyancy flux (B) which acts to extract energy from the potential energy and contributes to the negative turbulent production in the TKE budget. Furthermore, the negative production transfers energy from TKE to MKE as seen by the increase in the velocity magnitude in figure 2.12(c) during the contraction.

2.0.2.4 Effect of stratification on the TKE budget and mixing efficiency

The effect of the contraction on the TKE budget and mixing efficiency is illustrated in figure 2.14. When the stratification is weak as in the $Ri = 0.04$ and $Ri = 0.08$ cases, there are time intervals when the integrated production has significantly negative value. The magnitude of the peak negative values in these cases can be as large as 20% of the magnitude of the peak positive value. The production acts as a transfer term between MKE and TKE in two ways. During the growth of the KH billows as well as the growth of turbulence at the later time, production transfers energy from MKE to TKE. During the contraction, the transfer reverses in direction such that the available potential energy is released through positive buoyancy flux to generate TKE and negative production acts to increase the MKE. It is noted that, during the second contraction in the $Ri = 0.04$ case which commences at $S_0 t \approx 150$, the production has negative value and the buoyancy flux has positive value similar to what is observed during the first contraction and these anomalous values last for a longer time than during the first contraction. The difference between these two contractions is in the dissipation rate which is negligible during the first contraction. During the second contraction, the two KH billows evolve into two isolated turbulent patches that are able to meander far from the center of the shear layer due to the weak stratification. The meandering acts to increase MKE, e.g. the negative production, and at the same time reduce the available potential energy, e.g. the positive buoyancy flux. As stratification increases in the other cases, the turbulent shear layer does not meander and the second contraction is not seen.

The first contraction in the $Ri = 0.04$ case has a profound effect on the dissipation rate of the potential energy (ε_ρ). Figure 2.14(d) shows that ε_ρ has a local peak during the contraction period in this case while it increases monotonically in the other cases. Noting that the TKE dissipation

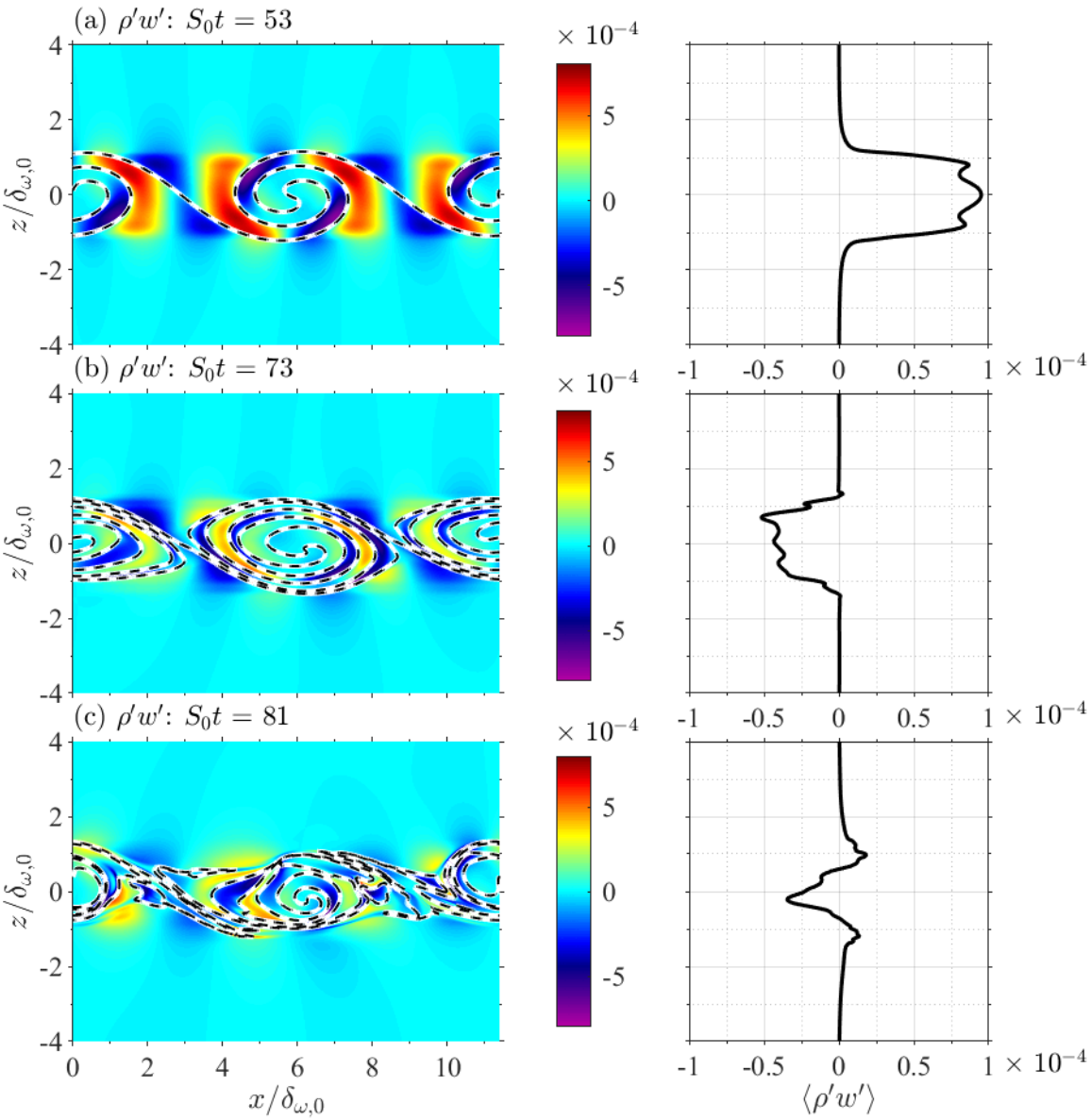

Figure 2.13: Cross-sectional snapshots of the density flux ($\rho'w'$) field for the $Ri = 0.04$ case at various times: (a) $S_0t = 53$, (b) $S_0t = 73$, and (c) $S_0t = 81$. The $y/\delta_{\omega,0}$ - $z/\delta_{\omega,0}$ planes are extracted at $x/\delta, \omega_0 = 5.7$. Dashed lines show the isopycnal contour of $\rho = 0$. Profiles of horizontally-averaged density flux ($\langle \rho'w' \rangle$) at the same times are shown in the panels on the right.

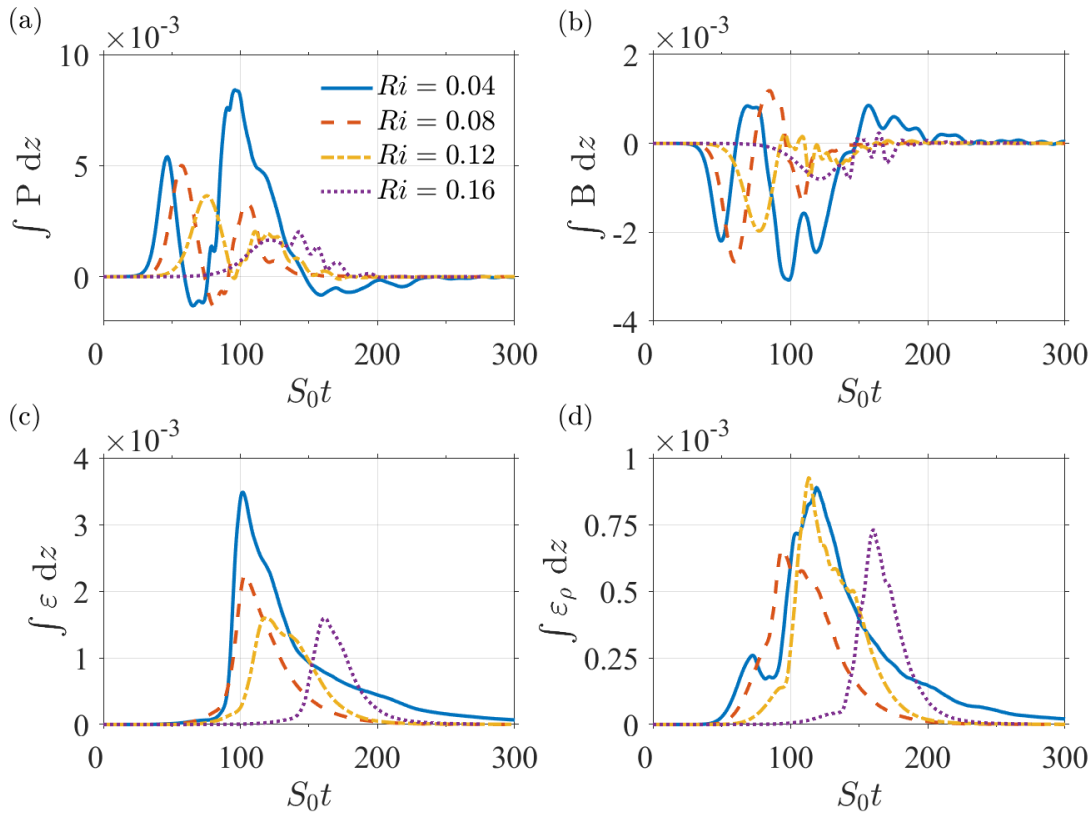

Figure 2.14: Evolution of the depth-integrated TKE budget and the potential energy dissipation for all *Ri*: (a) production (P), (b) buoyancy flux (B), (c) TKE dissipation (ε), and (d) dissipation of the potential energy, (ε_ρ). Integration is performed over the region bounded by $z = \pm 5$.

rate (ε) is insignificant during the period of the elevated ε_ρ, the mixing efficiency reaches up to 0.8 during this period. As previously shown, during the deformation of the KH billows, density filaments/wisps inside the billows become significantly thinner. The filaments reduce the density gradient in the shear layer down to the diffusive scale where it is dissipated by molecular diffusion. Interestingly, turbulence does not have a role in the mixing during this period despite the high Reynolds number.

Figure 2.15 shows the evolution of integrated mixing efficiency, $\Gamma = \int \varepsilon_\rho \, dz / (\int \varepsilon \, dz + \int \varepsilon_\rho \, dz)$ with *Ri*. We first examine the cumulative mixing efficiency (Γ_C) by integrating ε_ρ and ε over the time duration of the simulations. The maximum value of Γ_C is approximately equal to 0.34 and occurs in the $Ri = 0.12$ case. The $Ri = 0.08$ and $Ri = 0.16$ cases have smaller values. Relative to the results of Mashayek & Peltier (2013) (denoted in figure 2.15 as MCP13), the peak value

of Γ_C in the present study is smaller due to the stronger stratification associated with a uniform density gradient across the shear layer. A key result of the work by Mashayek & Peltier (2013) is that there exists a range of Ri for which the mixing efficiency is optimal. They report optimal mixing to occur at $Ri = 0.16$. When stratification deviates from this value, the mixing efficiency decreases. Interestingly, a similar trend is observed in the present study. Here, optimal mixing occurs in the $Ri = 0.12$ case in which there are rich dynamics of secondary instabilities during the transition from KH billows to turbulence. Relative to the results of Mashayek & Peltier (2013) in figure 2.15, optimal mixing occurs at a slightly smaller Ri due to the smaller critical Richardson number in the present study as discussed in the linear stability analysis section.

The mixing efficiency due to fully-developed three-dimensional turbulence (Γ_{3d}) is found by starting integration from the time of fully-developed turbulence, t_{3d}. The maximum value of Γ_{3d} also occurs in the $Ri = 0.12$ case and is slightly smaller than the value seen in Mashayek & Peltier (2013). The most notable difference between their work and the present study concerns the $Ri = 0.04$ case. Mashayek & Peltier (2013) suggest the mixing efficiency to decrease monotonically for $Ri < 0.12$. The results of this study do not yield a similar result when the shear layer is uniformly stratified. Dynamics during the first and second contraction of the shear layer in the $Ri = 0.04$ case provide an additional route to mixing, such that the mixing efficiency can be significant even at low values of Ri. It should be emphasized that Γ_{3d} is computed without the early elevation in ε_ρ during the first contraction shown in figure 2.14(d) and that Γ_{3d} in the $Ri = 0.04$ case is larger than that in the $Ri = 0.08$ case.

2.0.3 The transition layer

During the evolution of the turbulent shear layer as illustrated in the previous section, shear instabilities and the resulting turbulence transport a significant amount of momentum and energy toward the edges of the shear layer. Turbulent fluxes induce the formation of transition layers in which the local stratification has the largest value relative to any other location inside the shear layer. The shear also peaks inside the transition layers at late time. The previous examination of the

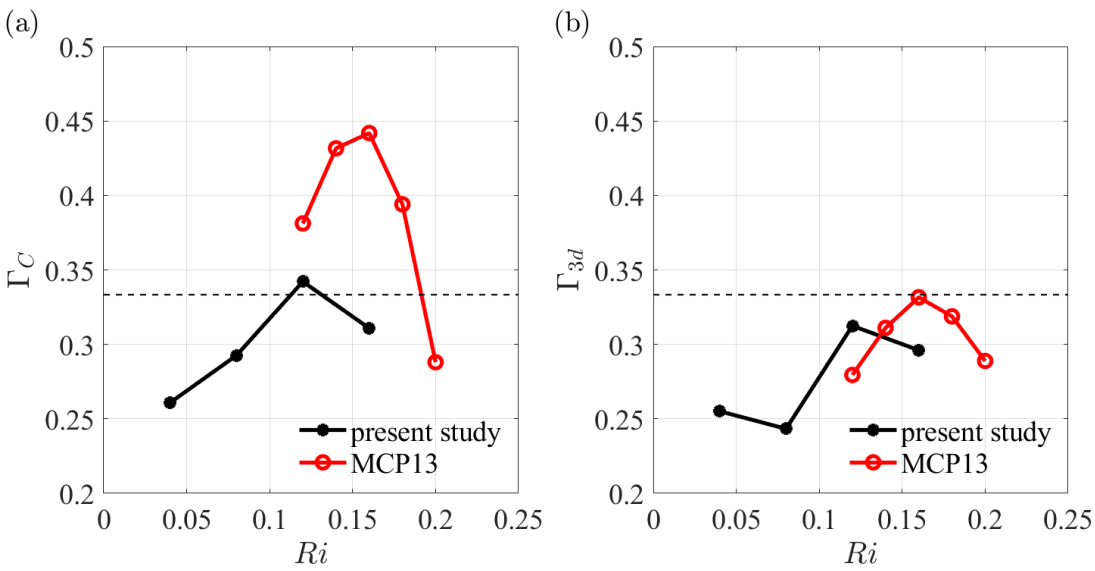

Figure 2.15: Effect of stratification on mixing efficiency: (a) Γ_C computed by integrating ε_ρ and ε over the time duration of the simulations and (b) Γ_{3d} computed by starting integration from the time of fully-developed turbulence, t_{3d}. Mixing efficiency in the two-layer simulations of Mashayek & Peltier (2013) (denoted MCP13) is shown for comparison. A dashed line indicates the optimal mixing efficiency suggested by the theory of Caulfield *et al.* (2004).

turbulent physics at the turbulent/non-turbulent interface (TNTI) by Watanabe *et al.* (2018) suggests a significant amount of TKE in the layer. Unlike Watanabe *et al.* (2018) who focus specifically on the TNTI (as an instantaneous spatially-varying interface inside the transition layer), this investigation takes a broader approach and evaluates the dynamics inside the entirety of the transition layer. In the following section, we examine the transition layer using horizontally-averaged flow statistics.

2.0.3.1 Mechanisms within the transition layer

For the purposes of this work, the transition layer boundaries are defined using the normalized buoyancy frequency, N^2/N_0^2. The inner and outer boundaries of the transition layer are identified by the locations at which N^2/N_0^2 is approximately equal to unity such that the interior of the transition layer has $N^2/N_0^2 > 1$. Figure 2.16 uses $S_0 t$ - $z/\delta_{\omega,0}$ contours to illustrate the half plane of the normalized buoyancy frequency (N^2/N_0^2) inside the transition layer for all Ri. The inner (TL$_i$) and outer (TL$_o$) transition layer boundaries are each identified using a dashed black and white line while the location of maximum N^2/N_0^2 inside the shear layer (TL$_m$) is shown with a

magenta and white line. Note that the maximum N^2/N_0^2 is variable and closer to the inner boundary of the transition layer at early time while located more centrally between the two boundaries at late time. There is a sharp increase in N^2/N_0^2 in the lower half of the transition layer before and during the growth stagnation and contraction regimes for the $Ri = 0.04$, $Ri - 0.08$, and $Ri = 0.12$ cases. In all cases, as the flow transitions from being dominated by two-dimensional instabilities to fully three-dimensional turbulence, there is a time period when the peak N^2/N_0^2 decreases (approximately $80 < S_0t < 160$ in the $Ri = 0.04$ case, $90 < S_0t < 110$ in the $Ri = 0.08$ case, $100 < S_0t < 150$ in the $Ri = 0.12$ case, and $140 < S_0t < 170$ in the $Ri = 0.16$ case). After turbulence decays at late time, N^2/N_0^2 increases and concentrates at the center of the transition layer with the transition layer edges characterized by lower N^2/N_0^2. The overall value of N^2/N_0^2 decreases with strengthening background stratification (N_0^2) due to the decreased turbulent mixing of momentum near the center of the shear layer when background stratification is increased. At late time, the flow has arranged itself into layers with varying N^2/N_0^2. Take the $Ri = 0.16$ case of figure 2.16 in which this is most evident. As seen in the vertical profile panel to the right of figure 2.16(d), at late time ($S_0t \approx 250$), there is a region at the center of the shear layer where $N^2/N_0^2 \approx 1$ above which is a layer with $N^2/N_0^2 < 1$. Moving outwards from this layer, there is a region of moderate N^2/N_0^2 before reaching the maximum value in the center of the transition layer of $N^2/N_0^2 \approx 1.8$. At the outer edge of the transition layer, N^2/N_0^2 is reduced and values of order unity are seen outside of the transition layer. In general, as background stratification increases, the transition layer becomes thinner while the local stratification becomes stronger.

The evolution of the normalized squared rate of shear (S^2/S_0^2 where $S = \partial\langle u\rangle/\partial z$) for all simulated cases is given in figure 2.17 using S_0t - $z/\delta_{\omega,0}$ contours. The lines bounding the transition layer are included for clarity. The transition layer develops as shear is reduced inside the shear layer by the influence of KH instabilities extracting kinetic energy from the flow at early time. However, at the peripheries of the shear layer, shear becomes elevated as turbulence induces momentum transport away from the center of the shear layer outwards. As such, the strongest shear at late time is located in the transition layer, close to its inner boundary, with shear intensity increasing

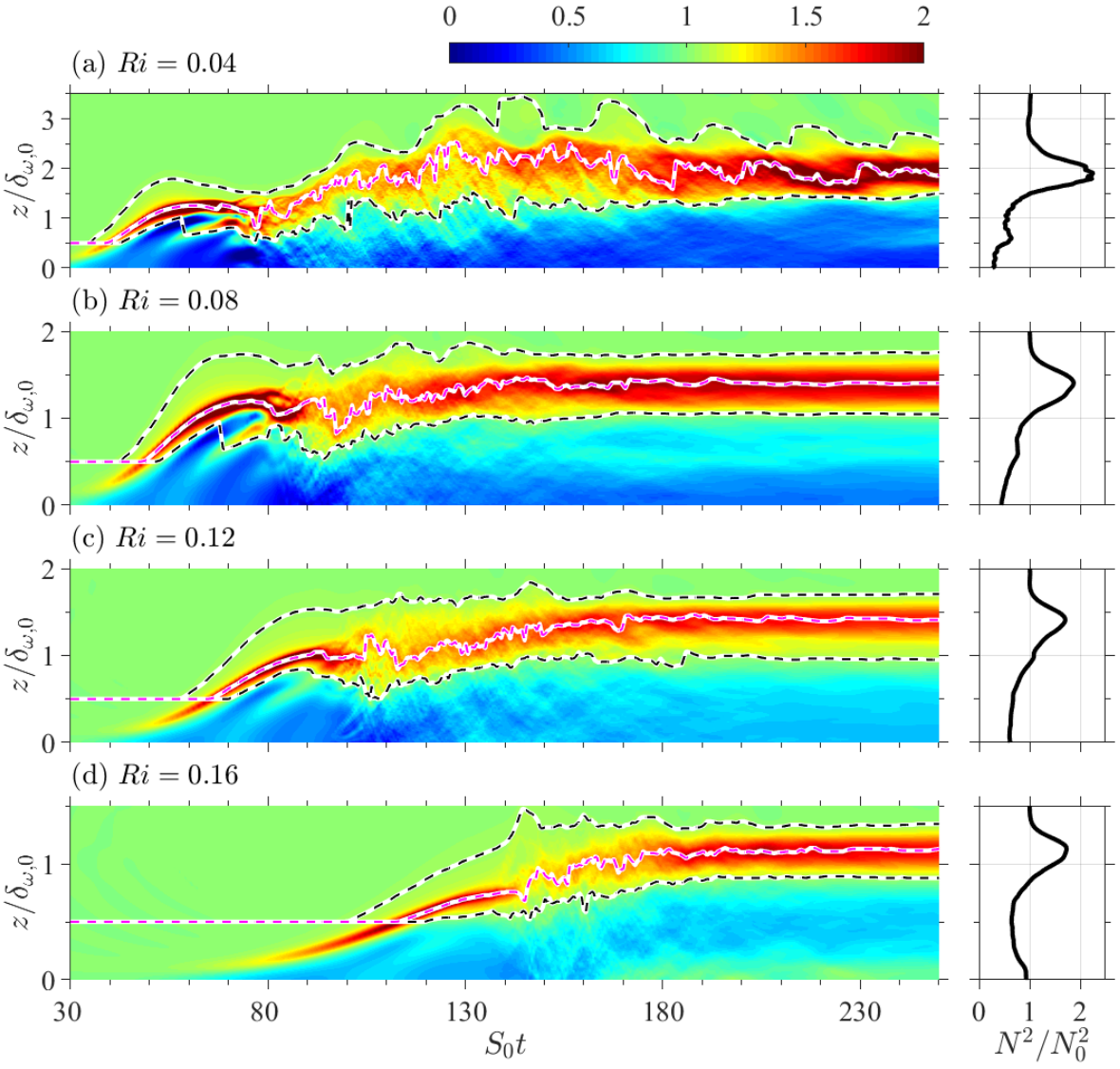

Figure 2.16: Evolution of the normalized squared buoyancy frequency (N^2/N_0^2) shown using $S_0 t$ - $z/\delta_{\omega,0}$ contours for the (a) $Ri = 0.04$, (b) $Ri = 0.08$, (c) $Ri = 0.12$, and (d) $Ri = 0.16$ cases. The inner (TL_i) and outer (TL_o) transition layer boundaries are each identified using a dashed black and white line while the location of maximum N^2/N_0^2 inside the shear layer (TL_m) is shown with a magenta and white line. Panels are given on the right for each case to illustrate vertical profiles of N^2/N_0^2 at late time, $S_0 t \approx 250$.

with strengthening background stratification (increased Ri). At early time in all cases, a region of strong shear directly corresponds to the region of large N^2/N_0^2 in the transition layer. The previously discussed reduction in N^2/N_0^2 coincides with a brief reduction in shear in the $Ri = 0.04$ and $Ri = 0.08$ cases. In the more strongly stratified cases, there is less signficant reduction in shear. At late time in the highly stratified cases, a similar layered structure to that described in figure 2.16 is observed. The panel to the right of figure 2.17 shows the center of the shear layer to have a region of moderate shear bounded by a layer of weaker shear. As we move farther from the center of the shear layer, shear increases to a peak value seen near the center of the shear layer ($S^2/S_0^2 \approx 0.35$). At the outer boundary and outside of the transition layer, S^2/S_0^2 becomes negligible.

The gradient Richardson number (Ri_g) given by $Ri_g = N^2/S^2$ is a measure of the balance between buoyancy and shear. Figure 2.18 uses $S_0 t$ - $z/\delta_{\omega,0}$ contours to illustrate Ri_g with the boundaries of the transition layer included. In all cases, the inner portion of the transition layer has lower Ri_g than the outer half. As expected, this indicates that the outer portion of the transition layer is dominated by buoyancy while inner region is most influenced by effects of shear. Linear stability theory suggests an assumed critical gradient Richardson number of $Ri_c \approx 0.25$ (Hazel, 1972). As the flow evolves, turbulence mixes the density and momentum fields thereby increasing Ri until is exceeds the critical value. In all cases, this behavior is observed within the transition layer with Ri_g beginning small and eventually becoming much larger than Ri_c, growing continuously in all but the $Ri = 0.04$ case. In the $Ri = 0.04$ case, mixing causes an increase in Ri_g until the increase in shear noted at late time, at which point, Ri_g decreases. At late time, in the $Ri = 0.16$ case, the interior of the shear layer is dominated by $Ri_g > 0.75$ while the inner boundary and lower half of the transition layer see slightly smaller values of $0.5 < Ri_g < 0.75$. Only in the $Ri = 0.04$ case does Ri_g attain values of approximately Ri_c at late time. In the $Ri = 0.12$ case, intermittent regions of $Ri_g > 0.75$ and $0.25 < Ri_g < 0.5$ are observed, in contrast to the two-layer simulations of Mashayek & Peltier (2013) who saw $Ri_g \approx 0.5$ across the entire shear layer at late time in their comparable simulation. The higher Ri_g found here is due to the large vertical fluxes of momentum and energy between the shear layer and the transition layers.

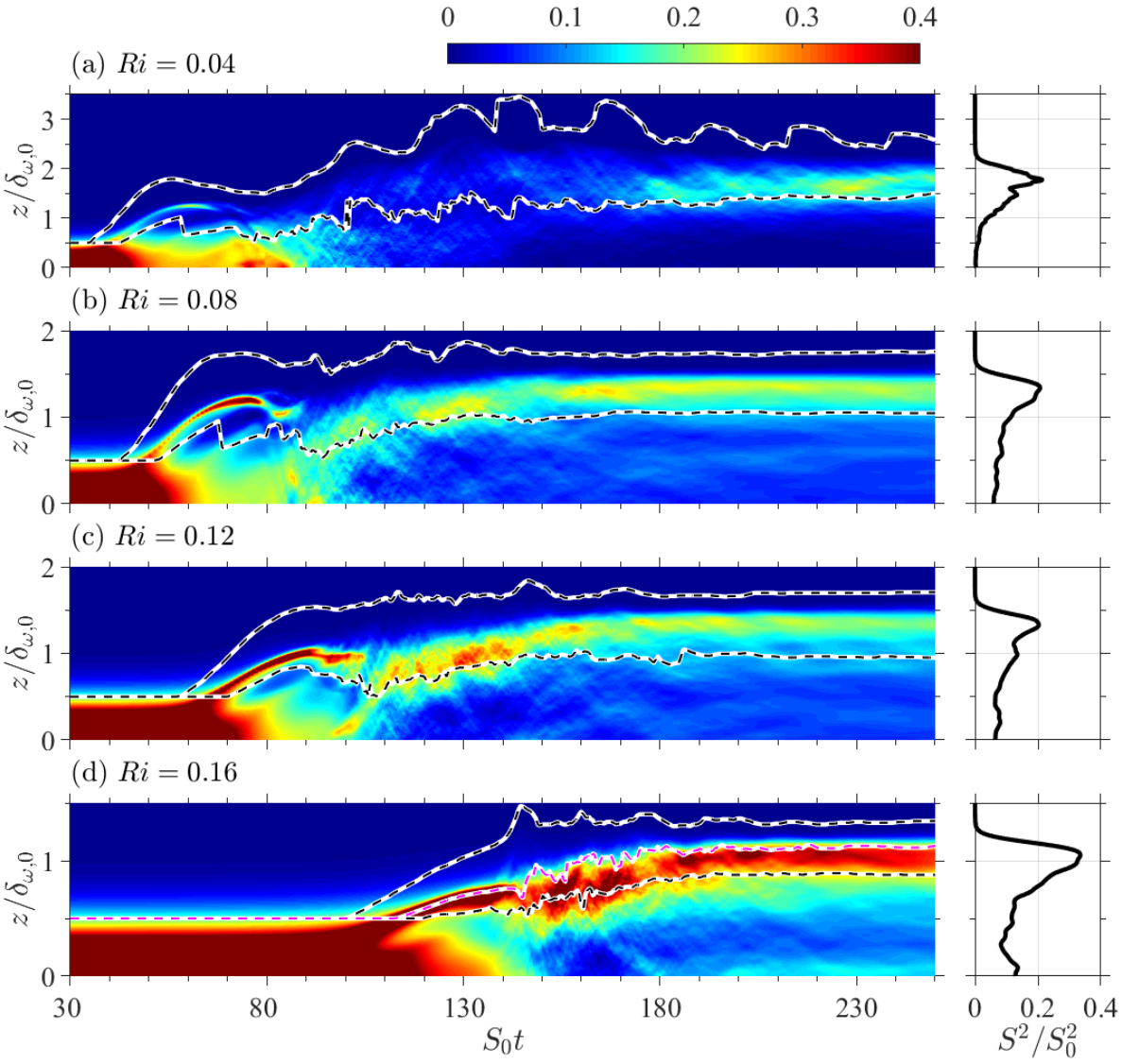

Figure 2.17: Evolution of the normalized squared rate of shear (S^2/S_0^2) shown using $S_0 t$ - $z/\delta_{\omega,0}$ contours for the (a) $Ri = 0.04$, (b) $Ri = 0.08$, (c) $Ri = 0.12$, and (d) $Ri = 0.16$ cases. Panels are given on the right for each case to illustrate vertical profiles of S^2/S_0^2 at late time, $S_0 t \approx 250$.

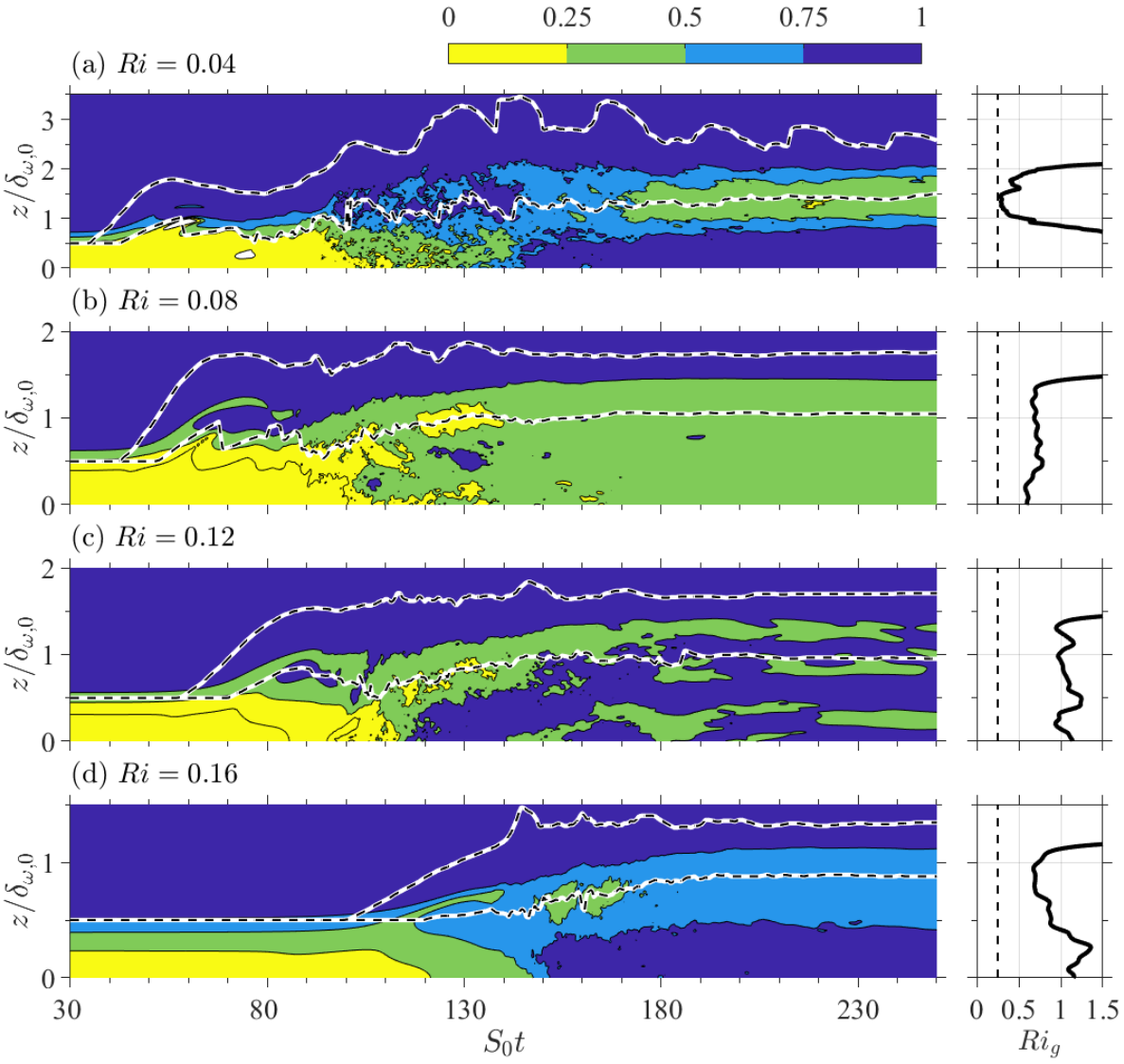

Figure 2.18: Evolution of the gradient Richardson number (Ri_g) shown using S_0t - $z/\delta_{\omega,0}$ contours for the (a) $Ri = 0.04$, (b) $Ri = 0.08$, (c) $Ri = 0.12$, and (d) $Ri = 0.16$ cases. Panels are given on the right for each case to illustrate vertical profiles of Ri_g at late time, $S_0t \approx 250$.

The development of small-scale fluctuations as the flow becomes fully turbulent leads to a rapid increase in the dissipation rate (ε) shown in figure 2.19. Peak ε is seen immediately before the KH billows are broken down to full turbulence at $S_0t \approx 100$ in the $Ri = 0.04$ and $Ri = 0.08$, $S_0t \approx 120$ in the $Ri = 0.12$ case, and $S_0t \approx 160$ in the $Ri = 0.16$ case. At late time, dissipation rate is strongest at the periphery near the inner boundary of the transition layer due to the evolving secondary instabilities. Because the shear layer core is relatively quiet at late time, ε is much smaller near the center of the shear layer. Dissipation rate is seen to be strongest at late time and persist longer in the $Ri = 0.04$ case.

The buoyancy Reynolds number (Re_b) can be used to quantify turbulent mixing and is given by $Re_b = \varepsilon/\nu N^2$. Figure 2.20 depicts the evolution of Re_b for all Ri. The peak magnitude of Re_b occurs during the development of KH billows and is largest in the most weakly stratified case ($Ri = 0.04$). As stratification increases, the magnitude of Re_b decreases. After transition to fully three-dimensional turbulence and as turbulence begins to decay, the magnitude of Re_b decreases though it remains strongest at the periphery of the shear layer near the inner boundary of the transition layer at late time. This is most clearly observed in the $Ri = 0.04$ case where Re_b remains relatively large at late time. Shih *et al.* (2005) employ simulations of a flow with homogeneous shear (uniform shear over an unbounded domain) to suggest a Re_b criterion for determining the extent of turbulent mixing. They assert that $Re_b > 10^2$ in order for there to be energetic mixing. Using this criterion, only the inner boundary of the transition layer sees energetic mixing as turbulence begins to develop in all cases. Despite the somewhat low values of Re_b seen in figure 2.20 throughout the region of the upper transition layer, turbulent mixing is still present in the case of localized shear as a result of the late-time shear instabilities previously discussed.

Turbulent mixing influences the density field by reducing the gradients near the center of the layer and enhancing those at the periphery. Figure 2.21 shows the evolution of the mixing efficiency (Γ) given by equation 2.11 using S_0t - $z/\delta_{\omega,0}$ contours for all Ri with the boundaries of the transition layer also depicted. Overall, mixing efficiency is much higher throughout the shear layer as KH billows are forming. As they break down into turbulence, strong mixing efficiency is

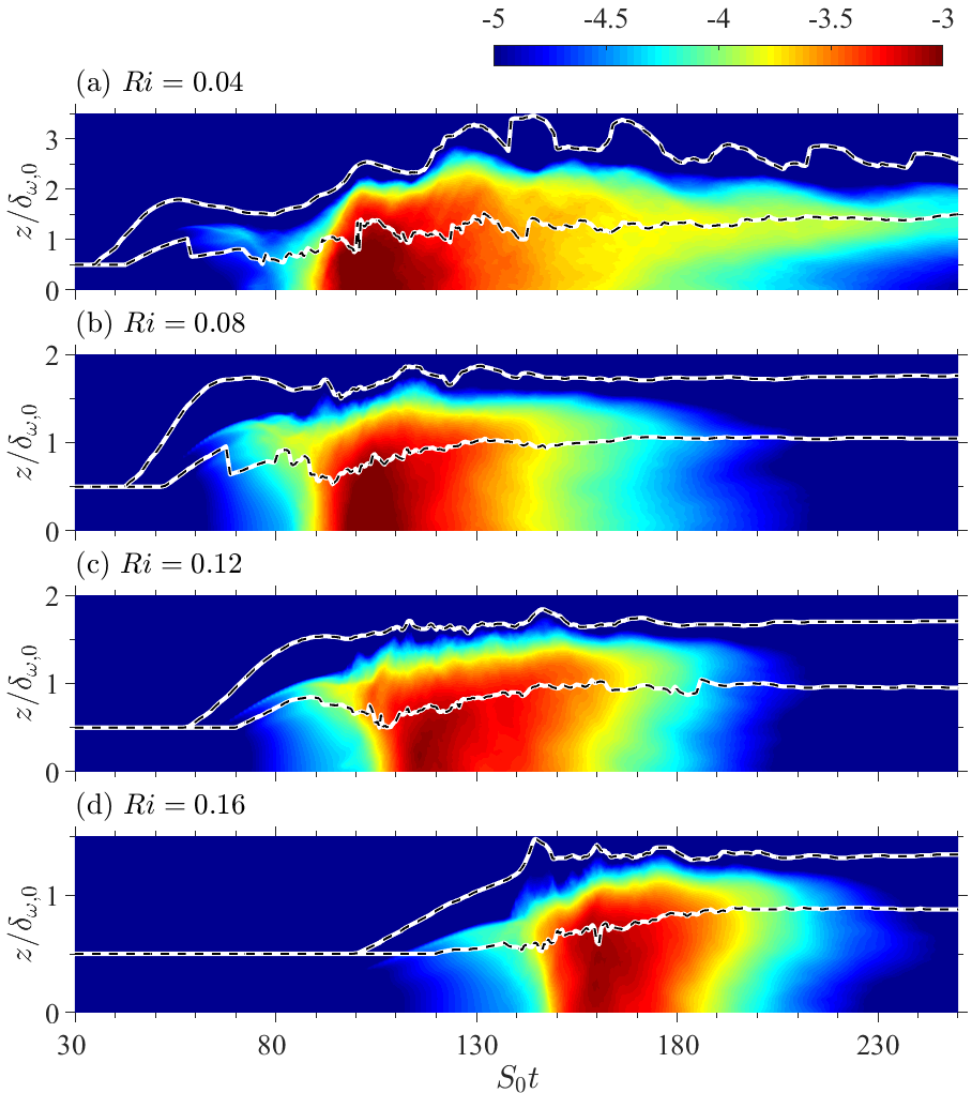

Figure 2.19: Evolution of the dissipation rate ($\log_{10}(\varepsilon)$) shown using $S_0 t$ - $z/\delta_{\omega,0}$ contours for the (a) $Ri = 0.04$, (b) $Ri = 0.08$, (c) $Ri = 0.12$, and (d) $Ri = 0.16$ cases.

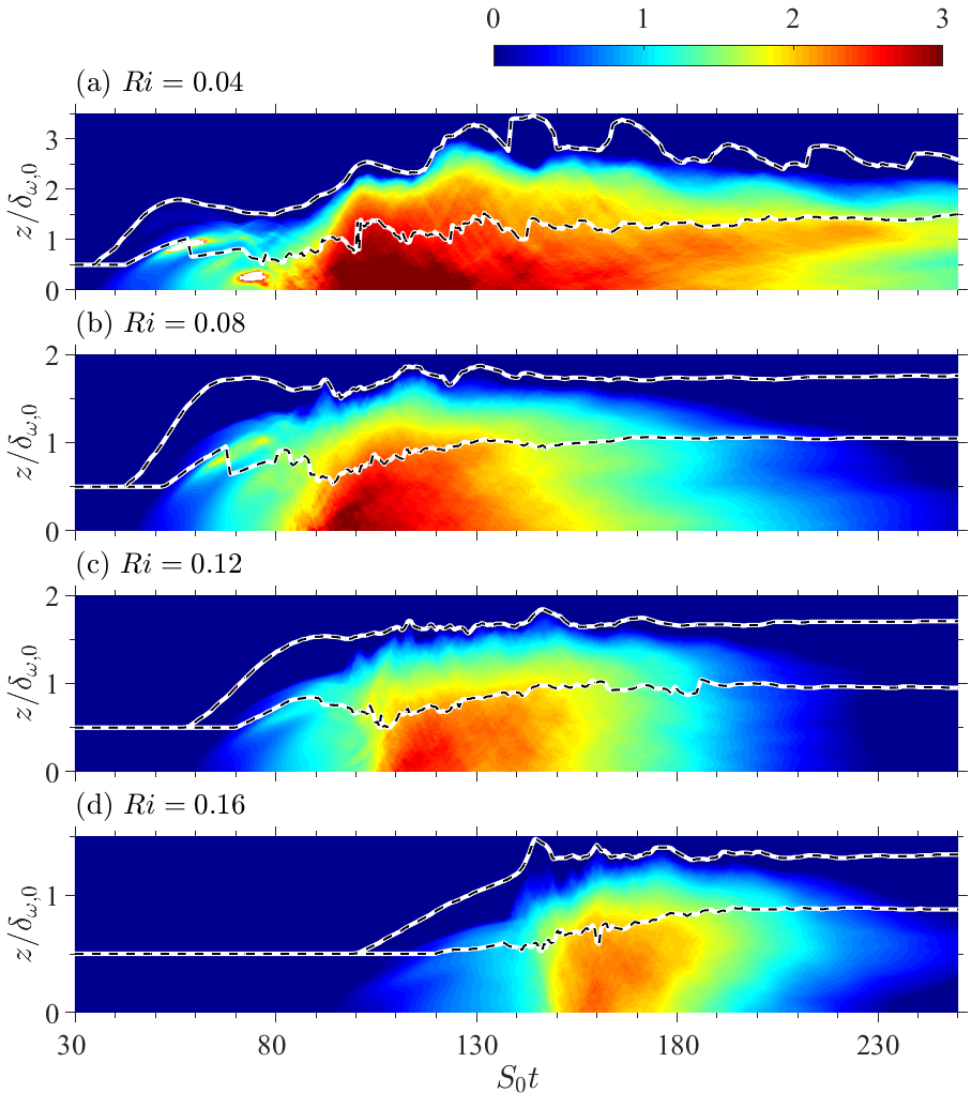

Figure 2.20: Evolution of the buoyancy Reynolds number ($\log_{10}(Re_b)$) shown using $S_0 t$ - $z/\delta_{\omega,0}$ contours for the (a) $Ri = 0.04$, (b) $Ri = 0.08$, (c) $Ri = 0.12$, and (d) $Ri = 0.16$ cases.

seen at the outer boundary of the transition layer while the core becomes relatively quiet with low mixing efficiency. This large mixing efficiency occurs after the secondary peak in production in the low Ri cases and is associated with the concentration of TKE in lobed structures. The inner boundary of the transition layer has comparably low mixing efficiency. As stratification increases and buoyancy effects suppress vertical motions, mixing efficiency becomes smaller as evidenced by the visualization of the $Ri = 0.16$ case of figure 2.21 at early time. At late time in all but the $Ri = 0.04$ cases, the majority of mixing occurs within or above the transition layer. In the $Ri = 0.04$ case, there is a reasonably high mixing efficiency remaining in the core as well with a region of low efficiency mixing above the core near the inner boundary of the transition layer. Turbulence-generated internal waves found outside of the transition layer in the background of the flow at late time have a high value of mixing efficiency. In these regions, Γ is approximately equal to 0.5 which implies $\varepsilon_\rho \approx \varepsilon$ for propagating internal waves. The presence of these internal waves is more apparent with increasing stratification as clearly seen at late time in figure 2.21 for all Ri.

Integrated mixing efficiency is shown in figure 2.22 for all Ri where the panels on the left are the result of integrating from the centerline of the shear layer up to the inner boundary of the transition layer (representing the core of the shear layer) and the panels on the right were obtained by integrating over the transition layer from the inner boundary (TL_i) to the outer boundary (TL_o) (representing the transition layer itself). In the core-integrated panel on the left, the peak mixing efficiency is associated with the KH billow formation and ranges from $\Gamma \approx 0.80$ in the weakly stratified case to only $\Gamma \approx 0.58$ in the strongly stratified case. Mixing efficiency significantly drops as the flow transitions to fully three-dimensional turbulence with all cases reaching a local minimum between approximately $100 \leq S_0 t \leq 120$ in the $Ri = 0.04$, $Ri = 0.08$, and $Ri = 0.12$ cases. This drop is less severe with increasing stratification and the $Ri = 0.16$ case sees a minimal drop to its local minimum at $S_0 t \approx 160$. All cases see late time mixing efficiency in the core of $\Gamma \approx 0.20$. Figure 2.22(b) indicates similar behavior in terms of the peak mixing efficiency during the KH billow formation for the $Ri = 0.04$, $Ri = 0.08$, and $Ri = 0.12$ cases. However, the $Ri = 0.16$ case shows a higher peak in the transition layer than in the core. Late time mixing efficiency in all cases

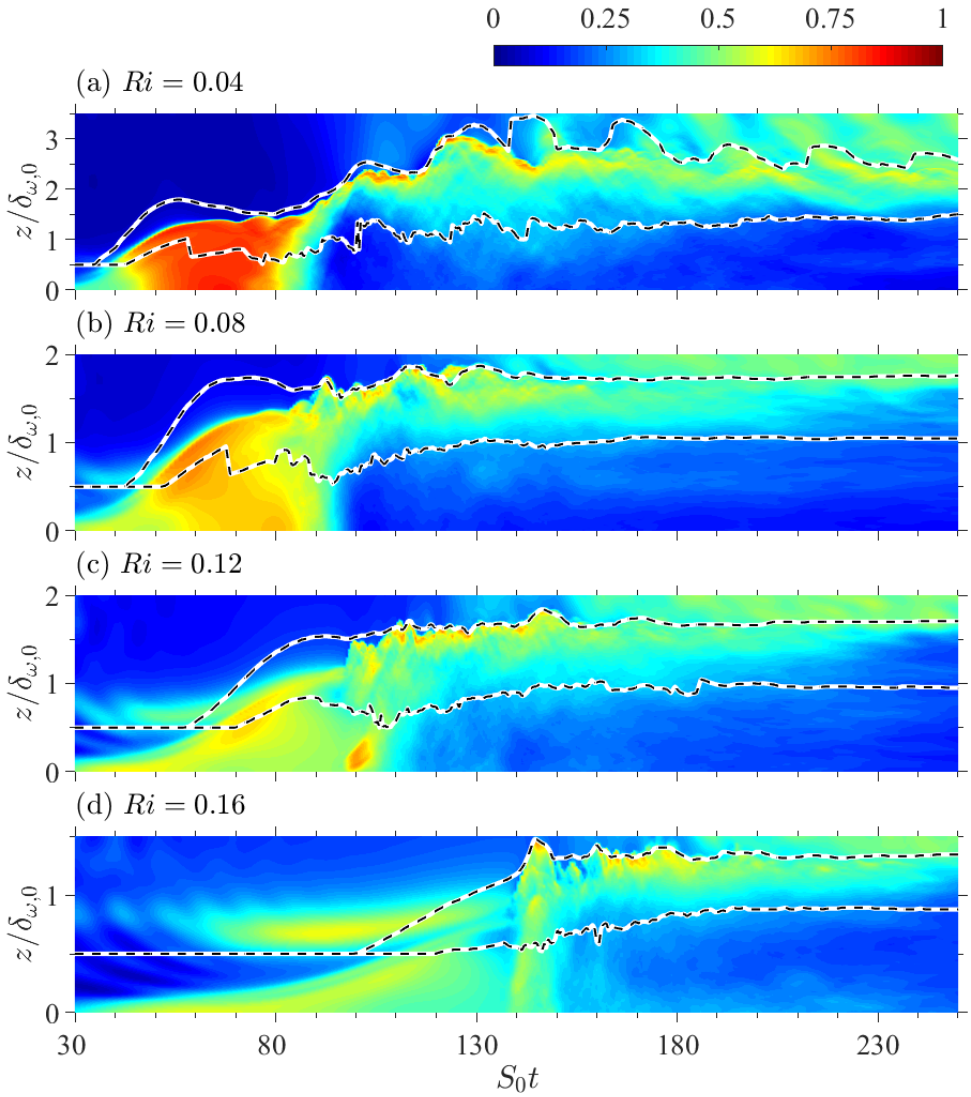

Figure 2.21: Evolution of mixing efficiency (Γ) shown using $S_0 t$ - $z/\delta_{\omega,0}$ contours for the (a) $Ri = 0.04$, (b) $Ri = 0.08$, (c) $Ri = 0.12$, and (d) $Ri = 0.16$ cases.

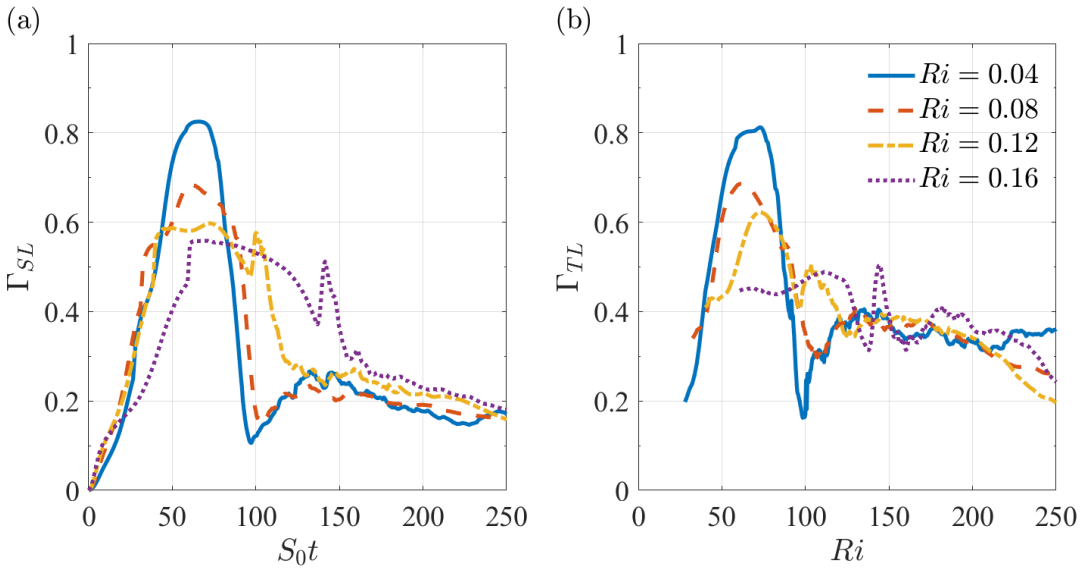

Figure 2.22: S_0t evolution of the mixing efficiency: (a) Γ_{SL} integrated from the center of the shear layer to the inner boundary of the transition layer (TL$_i$) and (b) Γ_{TL} integrated over the transition layer from the inner boundary (TL$_i$) to the outer boundary (TL$_o$) for all Ri.

is higher than in the core for all but the $Ri = 0.12$ case with approximately $0.25 \leq \Gamma \leq 0.35$.

In the highly stratified $Ri = 0.16$ case, at late time, the transition layer is energetic with significant turbulent activity. Small-scale instabilities (specifically SSI caused by the braid deformation of LCVI) can be clearly seen in the density and vorticity fields at late time ($S_0t = 229$) in figure 2.23. These residual instabilities grow and persist in the transition layer at the upper and lower periphery of the shear layer at late time. As such, Ri_g increases in this case. The presence of these instabilities indicates a much more energetic flow at late time in strongly stratified cases.

2.0.3.2 Internal wave flux

Simulations by Watanabe *et al.* (2018) suggest internal wave flux to be strong at the TNTI interface. They report that the peak value of $\langle p'w' \rangle$ can be as large as 50% of the integrated dissipation rate across the shear layer when the shear layer becomes turbulent. It is of interest to compare the role of internal wave flux as the Reynolds number increases from 6,000 to 24,000. Figure 2.24(a) illustrates the evolution of internal wave flux in the $Ri = 0.08$ case, in which, the magnitude of $\langle p'w' \rangle$ is largest during the transition from two-dimensional KH billows to three-

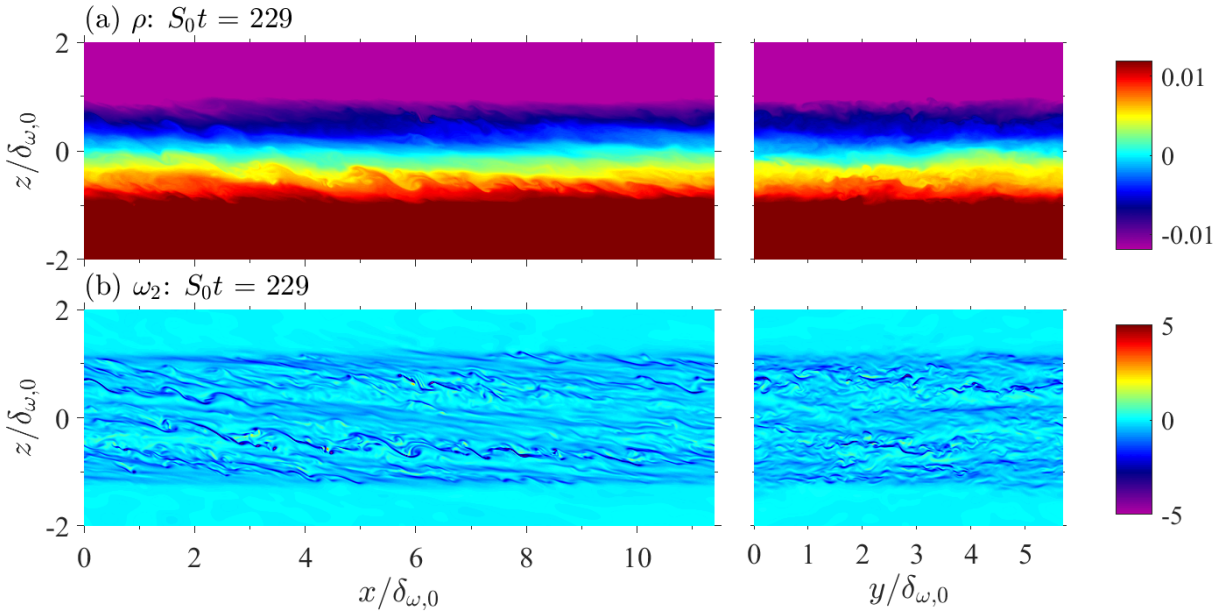

Figure 2.23: Cross-sectional snapshots of the (a) density (ρ) and (b) spanwise vorticity (ω_2) fields for the $Ri = 0.16$ case at $S_0t = 229$.

dimensional turbulence. As the billows grow, they create perturbations in the pressure and velocity fields that extend beyond the boundaries of the shear layer (denoted by the dashed lines in figure 2.24(a)). The perturbations generate evanescent waves whose amplitude decays exponentially with the distance away from the shear layer. The wave flux is initially positive in the upper shear layer and negative in the lower shear layer, and as a result, TKE is transported outside of the shear layer during the growth of the KH billows. It is noted that, since the waves are evanescent, energy does not propagate. As the shear layer grows in size, the energy that was previously transported outside contributes to the turbulence mixing in the transition layer. The wave flux in the transition layers is significantly weaker when the shear layer is turbulent.

The role of the wave flux is further examined by integrating the TKE budget from the lower transition layer to the upper transition layer. The result is shown in figure 2.24(b) where $\langle p'w' \rangle_I$ denotes the net wave energy that crosses the upper and lower transition layers. During the growth of the billows, waves transport energy outside the shear layer. As the shear layer becomes turbulent, the wave flux changes sign which extracts energy from the outside into the shear layer. During the period of turbulence, the peak inflow of the wave energy is approximately 33% of the peak integrated

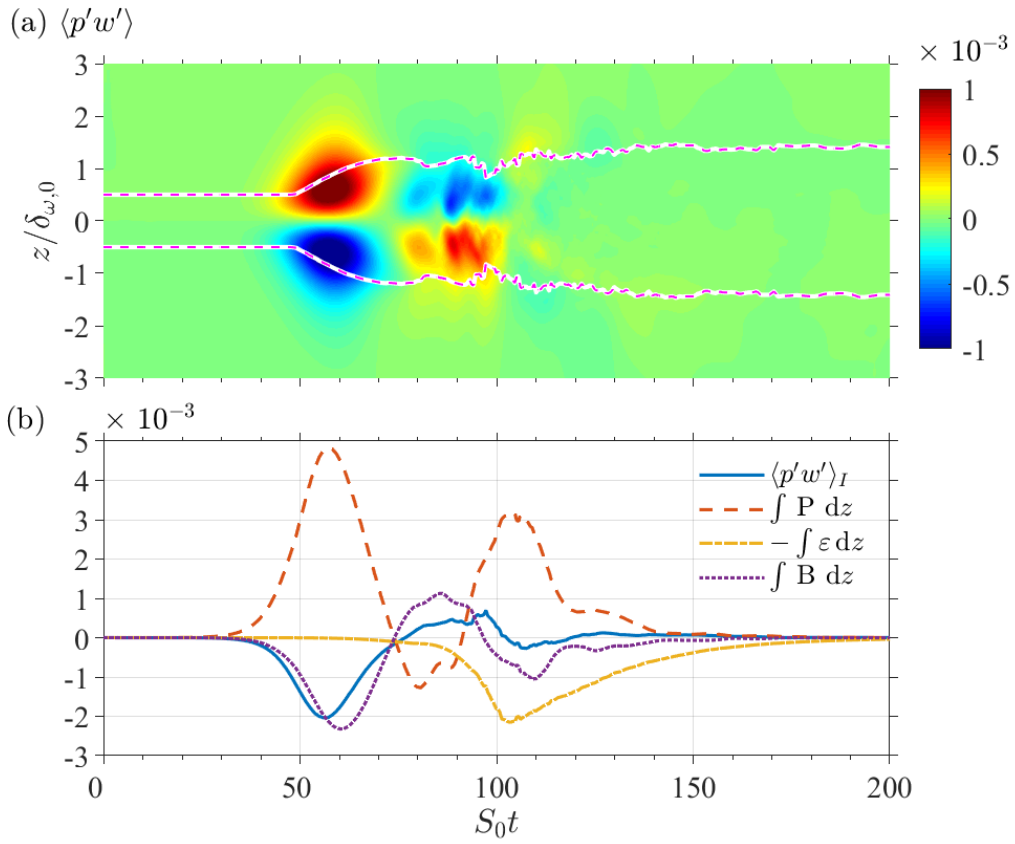

Figure 2.24: Evolution of the internal wave flux: (a) $S_0 t$ evolution of the internal wave flux ($\langle p'w' \rangle$) and (b) a comparison of the net internal wave flux across the upper and lower transition layers (the dashed boundaries shown in (a)) given by $\langle p'w' \rangle_I$ with respect to the other terms in the integrated TKE budget for the $Ri = 0.08$ case. White and magenta lines in (a) denote the location of maximum N^2/N_0^2 within the transition layer.

dissipation rate, 22% of the peak integrated production, and 70% of the peak integrate buoyancy flux. The wave flux seen in the present study is smaller than the value reported by Watanabe *et al.* (2018). Since the route to turbulence in the shear layer is different at high Reynolds number, so is the wave flux.

2.0.4 Conclusions

In the present study, DNS of a shear layer with uniform stratification were performed to investigate the evolution of turbulence and mixing in a stratified shear layer at Reynolds number, $Re_0 = 24,000$, a value considered high for DNS. The background density gradient is varied in four

cases to examine the effects of stratification, $Ri = [0.04, 0.08, 0.12, 0.16]$, where Ri is the Richardson number at the center of the shear layer. One of the objectives of the present work is to compare the rate of mixing in a shear layer between two layers with constant density as was investigated by Mashayek & Peltier (2013).

Linear stability analysis (LSA) of shear layers with uniform stratification as well as a two-layer density profile are performed to examine the fastest growing mode (FGM) of Kelvin-Helmholtz shear instabilities. While the inviscid linear stability theory of Hazel (1972) indicates that the critical Richardson number (Ri_c) is 0.25, when the effects of viscosity and a finite domain are included in the analysis, the value of Ri_c becomes smaller (approximately 0.18 in the two-layer case and approximately 0.15 in the uniform stratification case). At the same Richardson number less than the critical value, the FGM in the two-layer case has higher growth rate than the uniform stratification.

Results of the DNS indicate that routes to turbulence in the uniformly stratified shear layer are similar to those depicted in Mashayek & Peltier (2013). The transition from two-dimensional KH billows to three-dimensional turbulence consists of a large family of instabilities. The $Ri = 0.04$ case clearly illustrated the development of elliptical instabilities, SCI, and SCDI. Additional secondary instabilities were observed in the $Ri = 0.16$ case (eyelid instabilities, SCI, SSI, SPI, SVBI, and LCVI). SSI were seen to be far less prevalent in cases with weaker stratification in which SCI are the dominant driving instabilities. Mashayek & Peltier (2013) suggested the existence of an optimal range of Ri such that the mixing efficiency is maximized. They report that in the two-layer case, mixing efficiency is largest at $Ri = 0.16$ and that as Ri deviates from this value, the mixing efficiency decreases. For the case of uniform stratification, we found optimal mixing in the $Ri = 0.12$ case which is smaller than the value reported in the two-layer case. This lower value is due to the larger density gradients inside the shear layer and the smaller growth rate of the FGM as indicated by the LSA. It should be noted that although this work explores the dependence of mixing on Ri_g, other studies are being performed to establish the dependence of mixing efficiency on parameters other than Ri_g, e.g. Mater & Venayagamoorthy (2014).

The present study includes cases with weak stratification, e.g. $Ri = 0.04$ and $Ri = 0.08$. At low Ri, a contraction of the shear layer occurs when KH billows flatten in the streamwise direction without any development of turbulence. As the KH billows enlarge, the available potential energy in the shear layer increases. When the billows deform, the available potential energy is released back to the mean kinetic energy via a positive buoyancy flux and a negative turbulent production. During the period of contraction, density filaments inside the billows become so thin that the billow is dissipated by molecular diffusion in the absence of turbulence. As a result, the mixing efficiency reaches up to 0.8. The contraction is observed in the $Ri = 0.04$ and $Ri = 0.08$ cases but not in the other cases, indicating that background stratification plays an important role in this process. In the $Ri = 0.04$ case, there are two contractions, the second of which is driven by the meandering of turbulent patches resulting from the breakdown of the billows.

During the evolution of the shear layer, vertical fluxes result in the formation of transition layers at the edges of the shear layer. The transition layer is identified by large stratification and large shear due to turbulent mixing inside the shear layer. Analysis of the transition layer shows that, as the background stratification increases, the transition layer becomes thinner while the local stratification becomes stronger. Despite having the largest values of stratification, the transition layers see significant turbulence at late time long after turbulence at the center of the shear layer has subsided. The buoyancy Reynolds number in the transition layer is high, on the order of 10^2 while mixing in the transition layer is as efficient as near the center of the shear layer. Unlike the two-layer case reported by Mashayek & Peltier (2013) in which the Richardson number is equal to 0.5 throughout the shear layer at late time, the uniformly stratified shear layers considered herein evolve into multiple layers with differing gradient Richardson numbers. At late time, the Richardson number within the transition layer is observed to be smaller than the values found near the center of the shear layer.

Chapter 2 is a reprint of material in preparation for publication as follows: A. VanDine, H. T. Pham, S. Sarkar, “Evolution of turbulent shear layers with uniform stratification at high Reynolds number”, 2019. The author of this dissertation is the primary investigator and author of this work.

Chapter 3

Investigation of LES models for a stratified shear layer

As detailed in chapter 1, a comprehensive analysis of various LES models was performed in order to assess their performance in the modeling of a vertical shear layer. A DNS of a uniformly stratified shear layer with initial Reynolds number, $Re_0 = 24,000$, and initial centerline gradient Richardson number, $Ri_0 = 0.12$, is used as the benchmark for the LES models in this work. The initial Richardson number (Ri_0 as defined by equation 3.5b) is a measure of the stabilizing effect of stratification based on the squared ratio of the initial centerline buoyancy frequency to the initial centerline shear. Figure 3.1 depicts snapshots of density perturbations over the x - z plane at various times ($N_0 t$) in the DNS in order to illustrate the formation of KH billows and their transition into turbulence. Of particular interest are the creation and evolution of secondary instabilities which form along the braid of the billow and are clearly visible in the $N_0 t = 35$ snapshot. The instabilities and their breakdown into turbulence exhibited by the DNS are distinctive and this work assesses the ability of the LES models to capture said shear instabilities, depict transition to turbulence, and quantify turbulence decay. A detailed description of the SGS models used in this work is provided. The performance of the SGS models at varying grid resolutions is assessed while their relative computational costs are quantified.

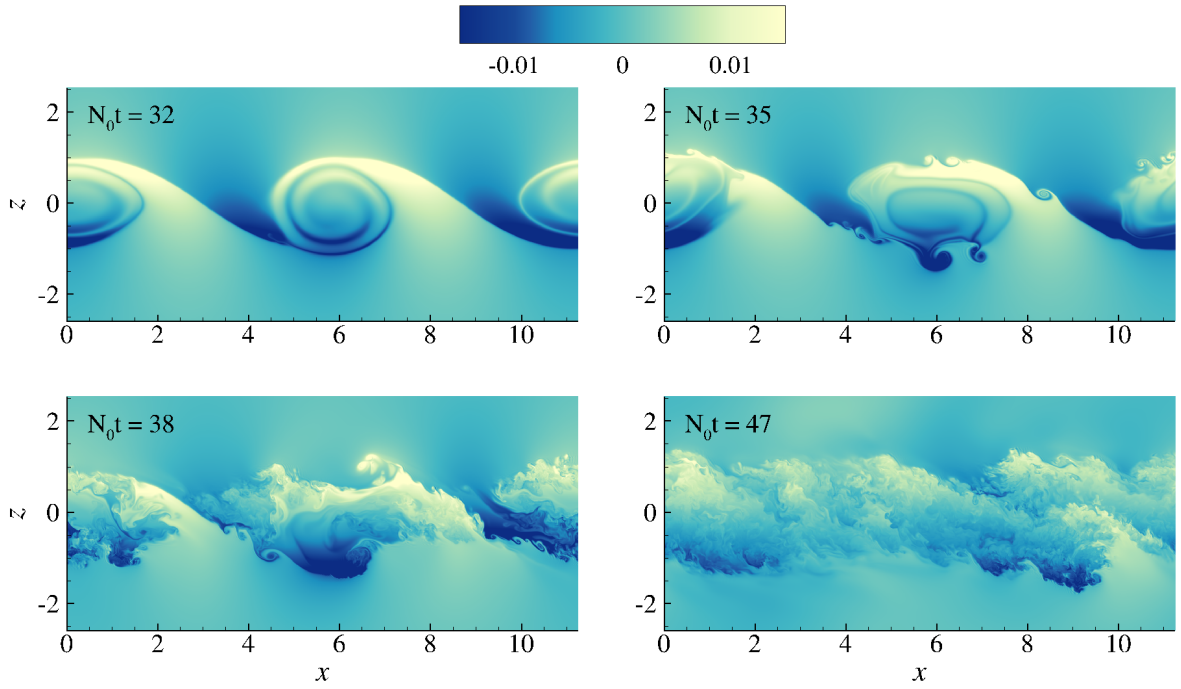

Figure 3.1: Snapshots of density perturbations over the x - z plane at various times in the DNS.

3.0.5 Formulation

3.0.5.1 Stratified shear layer

As in previous literature (Brucker & Sarkar, 2007; Pham & Sarkar, 2010, 2014), the temporally-evolving shear layer has an initial horizontal velocity (u) which varies continuously in the vertical direction (z). This initial profile at time, $t = 0$, is given by

$$\langle u^* \rangle (z^*, t = 0) = -\frac{\Delta U^*}{2} \tanh\left(\frac{2z^*}{\delta^*_{\omega,0}}\right) \tag{3.1}$$

where a superscript $*$ denotes a dimensional quantity, the $\langle\rangle$ operator indicates horizontal averaging, and ΔU^* indicates the velocity difference across the shear layer. The initial vorticity thickness of the shear layer is given by

$$\delta^*_{\omega,0}(z^*, t = 0) = \frac{\Delta U^*}{(d\langle u^* \rangle / dz^*)_{\max}}, \tag{3.2}$$

where the maximum shear at $t = 0$ occurs at the centerline ($z^* = 0$). The density profile at time, $t = 0$, corresponds to a uniformly stratified environment and is given by

$$\langle \rho^* \rangle (z^*, t = 0) = \frac{-\rho_0 N_0^{*2}}{g^*} z^*, \tag{3.3}$$

where N_0^{*2} is the squared buoyancy frequency of the ambient fluid which has constant value. Figure 2.1 provides a visualization of the stratified shear layer with key parameters noted for future reference.

3.0.5.2 Governing equations

The filtered three-dimensional Navier-Stokes equations for unsteady, incompressible flows with the Boussinesq treatment of density are utilized in their nondimensional form in equations 3.4a-3.4c. The overline $\bar{}$ operator is an indicator of spatial filtering. A Cartesian frame of reference is used such that $x_i = (x, y, z)$ and $u_i = (u, v, w)$ represent the streamwise, spanwise, and vertical directions and velocities, respectively. The nondimensional equations are as follows:

$$\frac{\partial \bar{u}_j}{\partial x_j} = 0 \tag{3.4a}$$

$$\frac{\partial \bar{u}_i}{\partial t} + \frac{\partial (\bar{u}_j \bar{u}_i)}{\partial x_j} = -\frac{\partial \bar{p}}{\partial x_i} + \frac{1}{Re_0} \frac{\partial^2 \bar{u}_i}{\partial x_j \partial x_j} - Ri_0 \bar{\rho}' g_i - \frac{\partial \tau_{ij}}{\partial x_j} \tag{3.4b}$$

$$\frac{\partial \bar{\rho}}{\partial t} + \frac{\partial (\bar{u}_j \bar{\rho})}{\partial x_j} = \frac{1}{Re_0 Pr} \frac{\partial^2 \bar{\rho}}{\partial x_j \partial x_j} - \frac{\partial \lambda_j}{\partial x_j} \tag{3.4c}$$

These equations were obtained using the following reference quantities: velocity difference (ΔU^*), initial thickness of the shear layer ($\delta^*_{\omega,0}$), and the constant background buoyancy frequency (N_0^*). Relevant nondimensional parameters are the initial Reynolds number (Re_0), initial gradient Richard-

son number at the center of the shear layer (Ri_0), and Prandtl number (Pr) given by

$$Re_0 = \frac{\Delta U^* \delta^*_{\omega,0}}{\nu^*}, \tag{3.5a}$$

$$Ri_0 = \frac{N_0^{*2} \delta^{*2}_{\omega,0}}{\Delta U^{*2}}, \tag{3.5b}$$

$$Pr = \frac{\nu^*}{\kappa^*}. \tag{3.5c}$$

Here, ν^* and κ^* are the kinematic viscosity and thermal diffusivity, respectively. Although $Pr = 5$ to 7 is typical for heat transport in water, the value of $Pr = 1$ is chosen as in several other studies so that, in the DNS, the scalar field does not require finer resolution than the velocity field.

The pressure (p) denotes deviation from the mean hydrostatic pressure. The Boussinesq approximation is employed such that density variations are considered only where they contribute to a gravitational force. Gravity acts in the vertical direction (z) and is given by g_i. Reynolds decomposition is used to decompose the velocity and pressure fields into mean and fluctuating components as follows where $\langle\rangle$ and $'$ indicate a mean and fluctuating value, respectively:

$$u_i(x_i,t) = \langle u_i \rangle (x_i,t) + u_i'(x_i,t)\,, \tag{3.6a}$$

$$p(x_i,t) = \langle p \rangle (x_i,t) + p'(x_i,t)\,. \tag{3.6b}$$

Density is composed of a constant reference density, a horizontally averaged mean component, and a fluctuating component as follows:

$$\rho(x_i,t) = \rho_0 + \langle \rho \rangle (z,t) + \rho'(x_i,t)\,. \tag{3.7}$$

The LES contributions to equations 3.4b and 3.4c are the subgrid stress (τ_{ij}) and the subgrid buoyancy flux (λ_j). The parameterization of these terms is detailed in a later section.

3.0.5.3 Numerical method

The numerical methods employed here are similar to those of our previous work (Brucker & Sarkar, 2007; Pham & Sarkar, 2010, 2014; VanDine *et al.*, 2018). Equations 3.4a-3.4c are solved using a staggered grid approach in which pressure and density are located at a cell center while normal velocities are located at cell faces. A second-order, central finite difference scheme is used for discretization of spatial derivatives. Time advancement is performed explicitly with the Williamson low-storage, third-order Runge Kutta method. A parallel multigrid solver which uses Red-Black Gauss-Seidel smoothing solves the Poisson pressure equation. A sponge region is employed in the regions $z > 10$ and $z < -10$ at the vertical boundaries in order to prevent reflections and damp propagating fluctuations. In this sponge region, a Rayleigh damping function gradually relaxes the density and velocities to their corresponding boundary conditions. This region does not inadvertently affect the simulation as it is sufficiently far from the shear layer.

Periodic boundary conditions are used in the streamwise (x) and spanwise (y) directions. In the vertical direction, a Dirichlet boundary condition is used for vertical velocity while Neumann boundary conditions are enforced for density, pressure, and the remaining velocities as follows:

$$\frac{\partial \rho}{\partial z}(-L_z/2) = \frac{\partial \rho}{\partial z}(L_z/2) = \frac{d\langle \rho^* \rangle}{dz^*}\,, \tag{3.8a}$$

$$\frac{\partial p}{\partial z}(-L_z/2) = \frac{\partial p}{\partial z}(L_z/2) = 0\,, \tag{3.8b}$$

$$\frac{\partial u}{\partial z}(-L_z/2) = \frac{\partial u}{\partial z}(L_z/2) = \frac{\partial v}{\partial z}(-L_z/2) = \frac{\partial v}{\partial z}(L_z/2) = 0\,, \tag{3.8c}$$

$$w(-L_z/2) = w(L_z/2) = 0\,. \tag{3.8d}$$

3.0.5.4 SGS models

The subgrid stress (τ_{ij}) and subgrid buoyancy flux (λ_j) are parameterized using eddy-viscosity type models with

$$\tau_{ij} = -2\nu_{sgs}\bar{S}_{ij}\,, \quad \lambda_j = -\kappa_{sgs}\frac{\partial\bar{\rho}}{\partial x_j}\,. \tag{3.9}$$

The velocity gradient tensor is composed of a symmetric component (the rate of strain tensor, S_{ij}) and an anti-symmetric component (the rate of rotation tensor, Ω_{ij}) which are given by

$$\bar{S}_{ij} = \frac{1}{2}\left(\frac{\partial\bar{u}_i}{\partial x_j} + \frac{\partial\bar{u}_j}{\partial x_i}\right)\,, \quad \bar{\Omega}_{ij} = \frac{1}{2}\left(\frac{\partial\bar{u}_i}{\partial x_j} - \frac{\partial\bar{u}_j}{\partial x_i}\right)\,. \tag{3.10}$$

Particulars concerning the calculation of subgrid eddy viscosity (ν_{sgs}) and subgrid thermal diffusivity (κ_{sgs}) in the Dynamic Smagorinsky, Ducros, and WALE LES models are given in sections 3.0.5.5, 3.0.5.6, and 3.0.5.7, respectively. In all models, a grid filter width is defined as Δ_f and taken to be $\Delta_f = (\Delta x\Delta y\Delta z)^{1/3}$ where Δx, Δy, and Δz indicate grid spacing along the orthogonal coordinates.

3.0.5.5 Dynamic Smagorinsky model

Although a number of variations on the Dynamic Smagorinsky model exist, the implementation in this work is adapted from that of Germano *et al.* (1991) and Lilly (1992). In the version of the model presented herein, eddy viscosity and thermal diffusivity are calculated locally using the smallest resolved scales of the flow in the velocity and density fields. In addition to the always present LES grid filter given by the overline $\bar{}$ operator, an additional spatial test filter is applied to the LES field. This coarser test filter given by the $\wedge$ operator uses the explicit trapezoidal rule with a three-point stencil. The ratio of the grid filter to the test filter is taken to be $\sqrt{6}$ as is typical. Eddy viscosity and thermal diffusivity are modeled as

$$\nu_{sgs} = C_d\Delta_f^2|\bar{S}|\,, \quad \kappa_{sgs} = C_\theta\Delta_f^2|\bar{S}|\,. \tag{3.11}$$

The dynamic coefficients are calculated using

$$C_d = -\frac{1}{2}\frac{\langle M_{ij}L_{ij}\rangle_s}{\langle M_{ij}M_{ij}\rangle_s}, \quad C_\theta = -\frac{1}{2}\frac{\langle P_jQ_j\rangle_s}{\langle Q_jQ_j\rangle_s}. \tag{3.12}$$

where

$$\begin{aligned} L_{ij} &= \widehat{\bar{u}_i\bar{u}_j} - \widehat{\bar{u}}_i\widehat{\bar{u}}_j, \quad M_{ij} = \widehat{\Delta_f}^2|\widehat{\bar{S}}|\widehat{\bar{S}}_{ij} - \widehat{\Delta_f^2|\bar{S}|\bar{S}_{ij}}, \\ P_j &= \widehat{\bar{\rho}\bar{u}_j} - \widehat{\bar{\rho}}\widehat{\bar{u}}_j, \quad Q_j = \widehat{\Delta_f}^2|\widehat{\bar{S}}|\widehat{\frac{\partial\bar{\rho}}{\partial x_j}} - \widehat{\Delta_f^2|\bar{S}|\frac{\partial\bar{\rho}}{\partial x_j}}. \end{aligned} \tag{3.13}$$

The $\langle\rangle_s$ operator in equation 3.12 indicates spanwise averaging. This is used to avoid issues with computational stability by smoothing outlier values of the coefficients. In the interest of preserving numerical stability, averaged coefficients with negative value are set to zero.

3.0.5.6 Ducros model

Implementation of the Ducros model is adapted from the work by Ducros *et al.* (1996). In the Ducros model, eddy viscosity is calculated using $\bar{F}_2^{(3)}$ which denotes a second-order structure function of the LES velocity field obtained after applying a high-pass filter to eliminate the larger scales of the field. Thus, the subgrid eddy viscosity is modeled as

$$\nu_{sgs} = 0.0014C_K^{-3/2}\Delta_f\left[\bar{F}_2^{(3)}\right]^{1/2}. \tag{3.14}$$

The high-pass filter is given by a four-neighbor formulation of a discrete Laplacian filter,

$$L\{\mathbf{u}_{i,j,k}\} = \mathbf{u}_{i+1,j,k} - 2\mathbf{u}_{i,j,k} + \mathbf{u}_{i-1,j,k} + \mathbf{u}_{i,j+1,k} - 2\mathbf{u}_{i,j,k} + \mathbf{u}_{i,j-1,k}. \tag{3.15}$$

This filter is applied three times sequentially to the LES field to obtain $\mathscr{U}$ as given by

$$\mathscr{U}_{i,j,k} = L^{(3)}\{\bar{\mathbf{u}}_{i,j,k}\}. \tag{3.16}$$

The second-order filtered structure function, $\bar{F}_2^{(3)}$, found in equation 3.14 is computed using the following four-neighbor formulation:

$$\begin{aligned}\bar{F}_2^{(3)} = \frac{1}{4}\Big[&||\mathscr{U}_{i+1,j,k} - \mathscr{U}_{i,j,k}||^2 + ||\mathscr{U}_{i-1,j,k} - \mathscr{U}_{i,j,k}||^2 \\ &+ ||\mathscr{U}_{i,j+1,k} - \mathscr{U}_{i,j,k}||^2 + ||\mathscr{U}_{i,j-1,k} - \mathscr{U}_{i,j,k}||^2\Big].\end{aligned} \tag{3.17}$$

The Kolmogorov constant (C_K) that appears in equation 3.14 is set to 0.5. Given an assumption of $Pr_{sgs} = 1$, the subgrid thermal diffusivity (κ_{sgs}) is equivalent to the subgrid eddy viscosity (ν_{sgs}).

3.0.5.7 WALE model

Implementation of the WALE model is adapted from the work by Nicoud & Ducros (1999). In the WALE model, eddy viscosity is calculated using a tensor invariant ($\mathscr{S}_{ij}\mathscr{S}_{ij}$) which incorporates the effects of both the rate of strain and rotation. This tensor invariant is sufficiently small in the case of pure shear and can reproduce laminar to turbulent flow transition which is a distinct advantage over other LES models. As the WALE model uses only local gradients and does not require filtering, this model is considered computationally inexpensive as compared to many existing models (Nicoud & Ducros, 1999; Posa & Balaras, 2018). Eddy viscosity is modeled as

$$\nu_{sgs} = C_\omega^2 \Delta_f^2 \frac{\left(\mathscr{S}_{ij}\mathscr{S}_{ij}\right)^{3/2}}{\left(\bar{S}_{ij}\bar{S}_{ij}\right)^{5/2} + \left(\mathscr{S}_{ij}\mathscr{S}_{ij}\right)^{5/4}} \tag{3.18}$$

where the tensor invariant is given by

$$\begin{aligned}&\mathscr{S}_{ij}\mathscr{S}_{ij} = \frac{1}{6}\left(S^2S^2 + \Omega^2\Omega^2\right) + \frac{2}{3}\left(S^2\Omega^2\right) + 2IV_{S\Omega}\,, \\ &S^2 = \bar{S}_{ij}\bar{S}_{ij}\,, \quad \Omega^2 = \bar{\Omega}_{ij}\bar{\Omega}_{ij}\,, \quad IV_{S\Omega} = \bar{S}_{ik}\bar{S}_{kj}\bar{\Omega}_{jl}\bar{\Omega}_{li}\,.\end{aligned} \tag{3.19}$$

In the above equations, the overline $\bar{}$ operator is an indicator of LES grid filtering. Unlike in the Dynamic Smagorinsky and Ducros models, a secondary filter is not employed in the WALE model. The coefficient C_ω is set to a reasonable value of 0.575 based upon the range, $0.55 \leq C_\omega \leq 0.60$, set

forth by Nicoud & Ducros (1999). Given an assumption of $Pr_{sgs} = 1$, the subgrid thermal diffusivity (κ_{sgs}) is equivalent to the subgrid eddy viscosity (ν_{sgs}).

3.0.5.8 Simulation setup and parameters

A total of six LES cases are performed and tested against an existing DNS (denoted in table 4.2 as DNS) which has $Re_0 = 24,000$, $Ri_0 = 0.12$, and $Pr = 1$. The DNS has an isotropic grid in the central region of the shear layer with mild stretching in the vertical. The grid spacing in the DNS at all times is less than 2.5η where $\eta = (\nu^3/\varepsilon)^{1/4}$ (ε denotes turbulent kinetic energy dissipation rate) is the Kolmogorov length scale. To better quantify the performance of the LES models, a grid influence study is performed wherein horizontal grids of both four times coarser and eight times coarser resolution than the DNS are utilized. These grids are respectively indicated in the case names of table 4.2 by either "x4" or "x8". The shear turbulence arising in the present problem is homogenous in the horizontal directions where LES subgrid models are known to perform well (Ducros *et al.*, 1996; Nicoud & Ducros, 1999; Germano *et al.*, 1991; Lilly, 1992). The vertical grid has the same resolution as in the DNS in order to resolve the large vertical gradients of mean velocity and density. Capturing secondary instabilities which develop due to these sharp gradients such as that noted at the approximate location $(x,z) = (8.5, 0.5)$ in the $N_0 t = 35$ panel of figure 3.1 requires a certain fineness of resolution which motivates this choice. The streamwise and spanwise grids have uniform spacing with $\Delta x = \Delta y = 0.03$ in the "x4" cases and $\Delta x = \Delta y = 0.06$ in the "x8" cases. The vertical grid is conservatively stretched outside of the uniformly-spaced region $-2.5 < z < 2.5$ around the center of the shear layer. A summary of the parameters for each simulation is provided in table 4.2.

Buoyancy preferentially affects the large scales of fluid motion. The Ozmidov scale defined by $L_{oz} = (\varepsilon/N^3)^{1/2}$ is a measure of the largest length scale of turbulent motions that is not directly affected by buoyancy. It is thought that LES of stratified turbulence should have a grid spacing that resolves L_{oz}. This is true for the vertical grid spacing (Δz) in both the "x4" or "x8" cases. In the "x4" cases with horizontal grid spacing Δx_f, the value of L_{oz} exceeds Δx_f over the entire period of

Table 3.1: Simulation parameters. The computational modeling approach used for each case is noted as either DNS, Dynamic Smagorinsky LES, Ducros LES, or WALE LES. The subscripts x, y, and z refer to the streamwise, spanwise, and vertical directions, respectively. The number of grid points in all directions (N_x, N_y, N_z) are given for each case. The initial Reynolds number is taken to be $Re_0 = 24{,}000$, initial Richardson number $Ri_0 = 0.12$, and Prandtl number $Pr = 1$ for all cases.

Case	Model	N_x	N_y	N_z
DNS	DNS	1536	768	1024
DSx4	Dynamic Smagorinsky LES	384	192	1024
Dx4	Ducros LES	384	192	1024
Wx4	WALE LES	384	192	1024
DSx8	Dynamic Smagorinsky LES	192	96	1024
Dx8	Ducros LES	192	96	1024
Wx8	WALE LES	192	96	1024

turbulence except at late time ($N_0 t > 70$) when TKE and dissipation are weak. During the period of strongest turbulence, the "x4" cases have grids which show excellent resolution of the large eddies with $L_{oz}/\Delta x_f \approx 10$ while the "x8" cases have grids which yield $L_{oz}/\Delta x_c \approx 5$ where x_c is the horizontal grid spacing of the "x8" cases. The "x8" grid has $L_{oz}/\Delta x_f > 1$ during the interval $35 < N_0 t < 60$, implying possibly inadequate resolution of the large eddies during the early and late time evolution of turbulence that falls outside this time interval.

3.0.6 LES performance at fine grid resolution

We begin with an analysis of the flow evolution and turbulent kinetic energy capture in the "x4" grid resolution LES cases as compared to the DNS.

3.0.7 Flow evolution

Of key importance is the ability of the LES models to capture the growth of the shear layer in time as well as the evolution of the mean velocity ($\bar{u}$). The evolution of momentum thickness,

$$\delta_\theta = \int_{-5}^{5} \left[\frac{1}{4} - \langle \bar{u} \rangle^2 \right] dz, \tag{3.20}$$

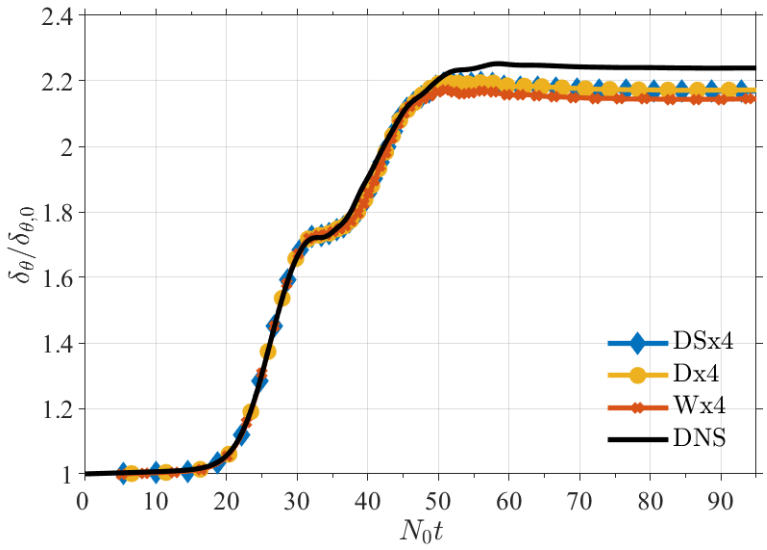

Figure 3.2: N_0t evolution of momentum thickness (δ_θ) normalized by initial momentum thickness ($\delta_{\theta,0}$) in the DNS and "x4" resolution LES cases.

normalized by its initial value ($\delta_{\theta,0}$) is given in figure 3.2. N_0t where N_0 is the background buoyancy frequency is used in plots throughout this work to quantify time in units of buoyancy time scale. For this and all future temporal integration profiles, quantities are obtained by averaging in the horizontal (x and y directions) and depth integrating in the vertical (z). In the DNS, approximately linear growth is noted between $20 < N_0t < 30$ when the KH billows form. After a short period of arrested growth, the layer resumes to thicken over $35 < N_0t < 50$ during which time there is a linear rate of growth due to a spurt of turbulence as will be discussed later. The momentum thickness stabilizes at $N_0t \approx 55$ and no further growth is noted. The capping of shear layer growth is a buoyancy effect that becomes sufficiently strong to cause turbulence decay and therefore a reduction of turbulent entrainment. All of the "x4" grid resolution LES models capture this effect of buoyancy on δ_θ although the onset of plateau at $N_0t = 50$ occurs slightly earlier than in the DNS. Consequently, the maximum momentum thickness of the LES cases is approximately 4% smaller than that of the DNS indicating a slight underestimation in turbulent entrainment. Despite this slight discrepancy, the momentum thicknesses yielded by the LES models are deemed acceptable.

Another indicator of mean flow evolution is shear, $S = d\langle\bar{u}\rangle/dz$. A direct comparison of the evolution of the normalized squared shear rate in the DNS and "x4" grid resolution LES

cases is provided in figure 3.3 using N_0t - z plots to illustrate both vertical and temporal variation. For this and all future N_0t - z plots, quantities are averaged over the spanwise (y) and streamwise (x) directions and then plotted as a function of z and N_0t where z is the vertical coordinate made nondimensional using the initial vorticity thickness ($\delta_{\omega,0}$). In both the DNS and "x4" grid resolution LES, a high concentration of shear is noted at the center of the shear layer until $N_0t \approx 20$ at which point the Kelvin-Helmholtz (KH) shear instabilities extract kinetic energy from the flow and reduce the shear. After $N_0t = 20$, weaker shear is noted in the core of the shear layer as the result of the mixing of momentum. At the same time, transition layers of enhanced shear develop at the top and bottom of the shear layer. Here, oceanographic practice is adopted wherein the transition layer refers to the layer over which there is a transition from a mixed region to a stratified background (Johnston & Rudnick, 2009). Elevated shear at the edges is induced by momentum transport from the center of the shear layer toward the periphery by turbulence. The LES models are able to capture the thickness and magnitude of the shear in these thin layers. This is possible because a fine grid spacing equivalent to that of the DNS was chosen in the vertical. The transition layer seen here is similar to the turbulent/non-turbulent interfacial layer reported by Watanabe *et al.* (2018). In the DNS as well as the LES, there is a period ($30 < N_0t < 35$) when the boundaries of the sheared region stop expanding and shear weakens at the edges. At $N_0t \approx 35$ in the DNS and slightly later in the LES, the boundaries resume expansion in the vertical. The vertical expansion continues until $N_0t \approx 55$ at which point the mean shear gradually weakens throughout the shear layer. The phases evident in the evolution of shear are consistent with those noted in the previous discussion of the momentum thickness.

To ensure that the LES models are able to capture the large eddies, the local stratification is also studied. Figure 3.4 shows N_0t - z plots of the local buoyancy frequency ($N^2(z,t)$) normalized by the background buoyancy frequency (N_0^2) for the DNS and "x4" resolution LES cases where $N^2 = -g/\rho_0 \partial \langle \rho \rangle \partial z$, and $N_0^2 = 0.12(\Delta U^*/\delta^*_{\omega,0})^2$. In figure 3.4, the DNS and "x4" grid resolution LES cases show similar evolution. The turbulent mixed core of the shear layer is well captured in all LES cases. Larger values of buoyancy frequency are observed at the edges of the shear layer after

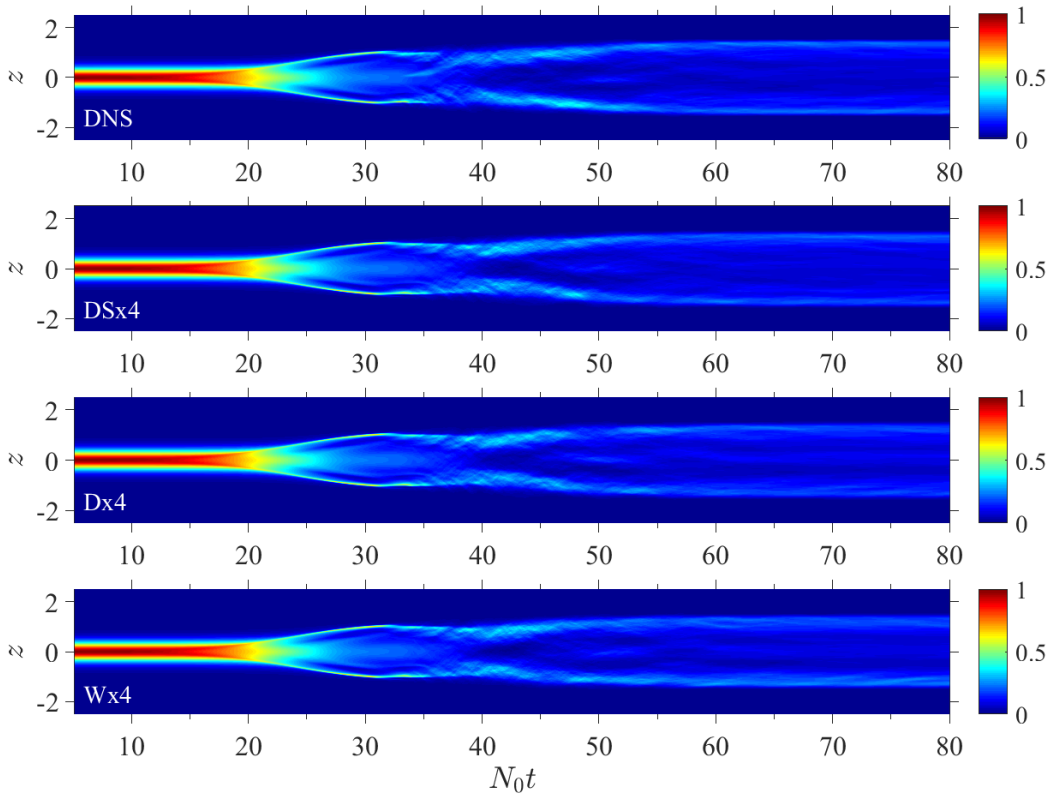

Figure 3.3: Comparison of squared shear rate (S^2) normalized by initial squared shear (S_0^2) using N_0t - z contours in the DNS and "x4" resolution LES cases. For this and all future N_0t - z plots, quantities are averaged over the spanwise and streamwise directions and then plotted as a function of z and N_0t where z is the vertical coordinate made nondimensional using the initial vorticity thickness ($\delta_{\omega,0}$).

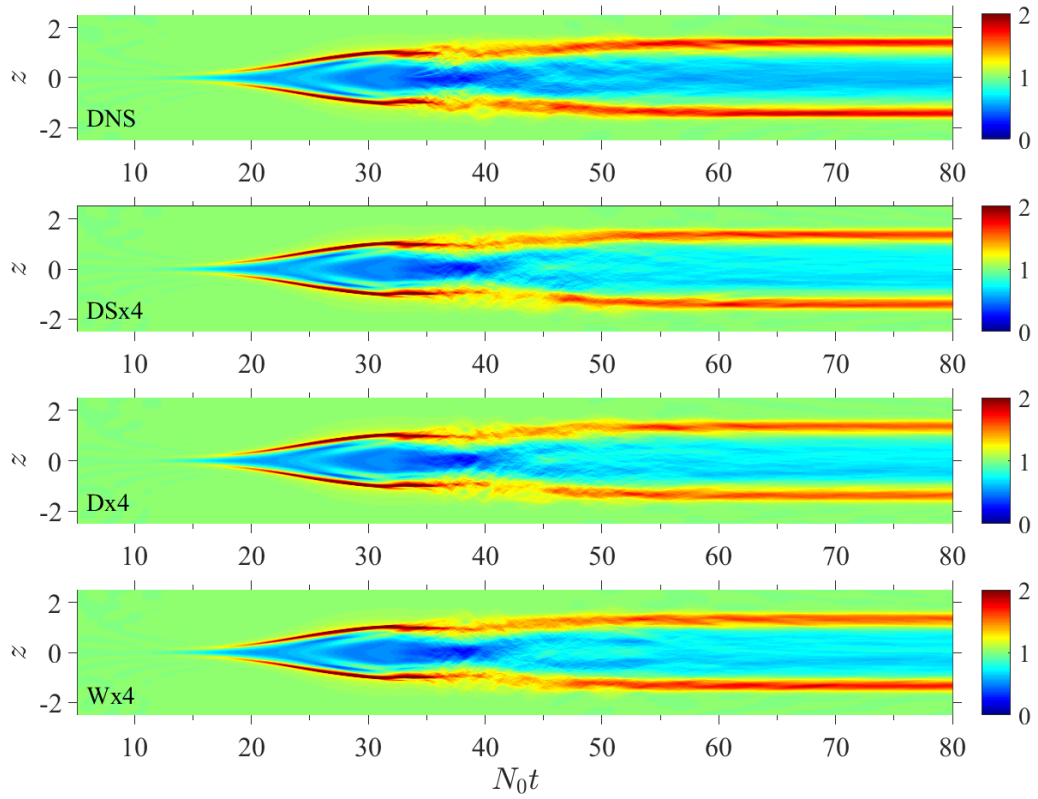

Figure 3.4: Comparison of local buoyancy frequency (N^2) normalized by the background buoyancy frequency (N_0^2) using $N_0 t$ - z contours in the DNS and "x4" resolution LES cases.

transition to turbulence. Similarly to the results for shear, stratification is enhanced in the transition layers at the top and bottom of the shear layer. Turbulent mixing reduces the density gradient in the center of the shear layer while enhancing gradients at the periphery. The LES models are able to capture the development of the strongly stratified sheared transition layer and show excellent agreement with the DNS.

The gradient Richardson number, $Ri_g = N^2/S^2$, measures the relative strength of the stabilizing density gradient and the destabilizing shear. From linear stability theory, KH shear instabilities develop from a laminar shear flow when $Ri < 0.25$ (Hazel, 1972). As the flow evolves, the local shear and stratification changes to create patches that become less or more susceptible to instability. An overall effect of turbulence is that it mixes the momentum and density fields such that Ri increases and eventually exceeds the critical value throughout the shear layer. Figure 3.5 gives

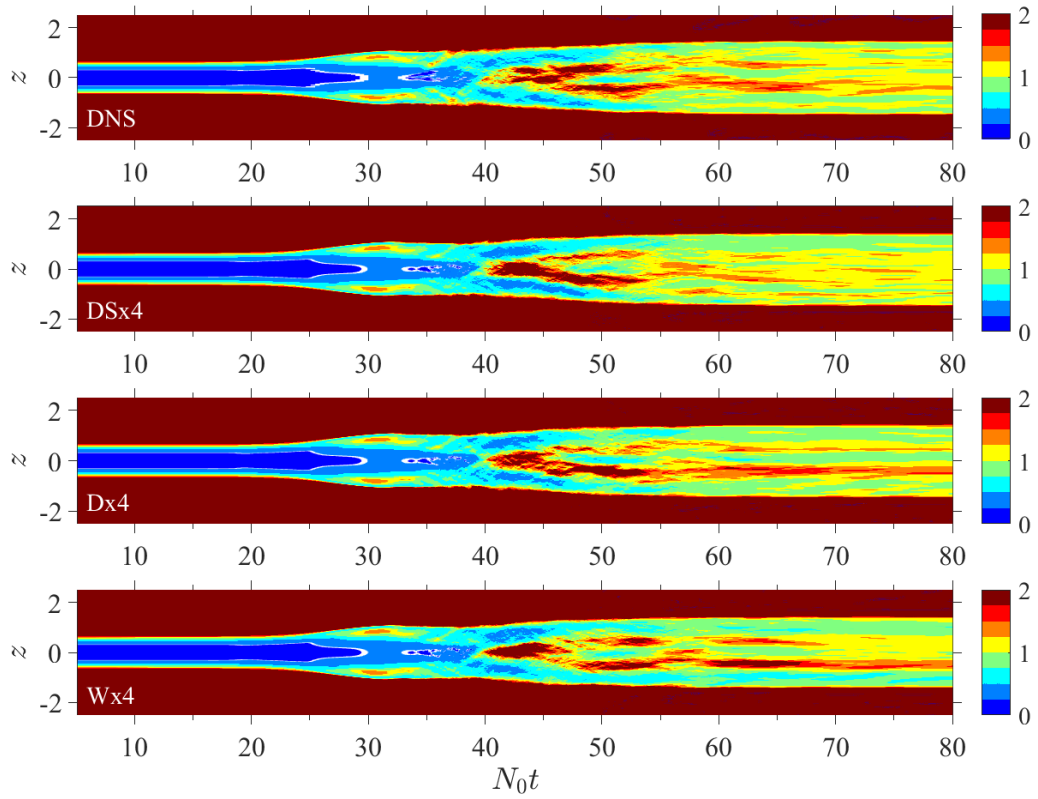

Figure 3.5: Comparison of the gradient Richardson number (Ri_g) using N_0t - z contours in the DNS and "x4" resolution LES cases.

the N_0t - z plots of Ri_g for the DNS and "x4" grid resolution LES cases. In the DNS, as the KH billows grow and amalgamate during the period $20 < N_0t < 30$, Ri_g increases from its subcritical value of $Ri_g = 0.12$ in the core of the shear layer while decreasing at the periphery. The central value of Ri_g exceeds 0.25 at $N_0t \approx 30$ which is also when the initial phase of linear growth of the momentum thickness tapers off (figure 3.2). Later, between $40 < N_0t < 45$, Ri_g decreases in the sheared transition layers. While the "x4" grid resolution LES cases are able to capture the behavior of Ri_g and show good agreement with the DNS, there are slight differences after $N_0t \approx 40$.

3.0.8 Turbulent kinetic energy evolution

The capture of turbulence is of paramount importance in assessing the performance of the LES models. The TKE is averaged in the horizontal (x and y directions) and depth integrated in the

vertical (z) to obtain its temporal evolution as shown in figure 3.6a with TKE given by $K = \frac{1}{2}\langle \bar{u}_i' \bar{u}_i' \rangle$. Transition to turbulence at $N_0 t \approx 15$ is captured by the LES and the rapid growth of the TKE until $N_0 t \approx 30$ occurs at the same rate in both the DNS and "x4" resolution LES cases. It is worth noting that this phase between $20 < N_0 t < 30$ of rapid growth of integrated TKE coincides with the initial phase of the linear growth of momentum thickness. The "x4" grid resolution LES cases and the DNS peak at $N_0 t \approx 40$ followed by a period of consistent decay. Apart from a slight overestimation between $35 < N_0 t < 45$, the LES models capture well the TKE evolution.

The LES models contribute two relevant subgrid terms to the TKE budget equation, namely the subgrid dissipation and transport. The TKE budget equation used in this work is given by

$$\frac{dK}{dt} = P - \varepsilon + B - \frac{\partial T_3}{\partial z} - \varepsilon_{sgs} - \frac{\partial T_{3,sgs}}{\partial z}. \tag{3.21}$$

with production (P), dissipation (ε), buoyancy flux (B), and transport term (T_3) specified as follows

$$\begin{aligned} P &= -\langle \bar{u}' \bar{w}' \rangle \tfrac{\partial \langle \bar{u} \rangle}{\partial z}, \quad \varepsilon = \tfrac{2}{Re_0} \langle \bar{S}_{ij}' \bar{S}_{ij}' \rangle, \quad \bar{S}_{ij}' = \tfrac{1}{2} (\tfrac{\partial \bar{u}_i'}{\partial x_j} + \tfrac{\partial \bar{u}_j'}{\partial x_i}), \\ B &= -Ri_0 \langle \bar{\rho}' \bar{w}' \rangle, \quad T_3 = \tfrac{1}{2} \langle \bar{w}' \bar{u}_i' \bar{u}_i' \rangle + \tfrac{1}{\rho_0} \langle \bar{w}' \bar{p}' \rangle - \tfrac{2}{Re_0} \langle \bar{u}_i' \bar{S}_{3i}' \rangle \end{aligned} \tag{3.22}$$

and the subgrid dissipation (ε_{sgs}) and transport ($T_{3,sgs}$) contributions given by

$$\varepsilon_{sgs} = -\langle \tau_{ij}' \tfrac{\partial \bar{u}_i'}{\partial x_j} \rangle, \quad T_{3,sgs} = \langle \tau_{i3}' \bar{u}_i' \rangle. \tag{3.23}$$

After horizontally averaging and depth integrating the TKE budget terms as was done with the TKE, a direct comparison between the DNS and LES results is performed. Figure 3.6 gives the temporal evolution of integrated production, total dissipation, and buoyancy flux for the DNS and LES cases. It should be noted that integration yields resolved and subgrid transport terms which are nearly zero and for that reason, they are neglected. In figure 3.6b, there is good agreement in production capture between the DNS and "x4" grid resolution LES cases. In the DNS, there are two notable peaks in the production. The first occurs at $N_0 t = 25$ and corresponds to the development of

two-dimensional secondary instabilities along the braid of the KH billows. The second, occurring at $N_0 t \approx 40$ concerns the transition to fully three-dimensional turbulence. This is known because, at the time of the first peak in production, there is no dissipation as would be the case in the development of two-dimensional KH instabilities. However, the second peak in production corresponds to the peak in dissipation indicating transition to fully three-dimensional turbulence. This point will be elaborated upon later. Although the LES cases perfectly capture the first peak, there is a slight delay in the second peak of production attributed in part to the positive buoyancy flux noted at this time and not observed in the DNS. The initial negative peak in buoyancy flux at $N_0 t \approx 25$ and subsequent decay to zero (figure 3.6c) is well captured in the "x4" grid resolution LES cases. Slight differences with the DNS are noted during the short period of positive integrated buoyancy flux between $35 < N_0 t < 40$ as well as at later time. There is little difference among the LES models in capturing either production or buoyancy flux. In contrast, there is variability in the capture of dissipation by the different LES models. In the dissipation plot of figure 3.6e, a 12% underestimation of peak dissipation by the Dynamic Smagorinsky and WALE models is observed. The Ducros model results in 6% stronger peak dissipation than the DNS. Of the three LES models, the Dynamic Smagorinsky and WALE models are the least dissipative while the Ducros model is the most dissipative. Despite the discrepancies in peak value at $N_0 t \approx 40$, the overall dissipation growth and decay are well captured in the "x4" grid resolution LES cases. The ratio of the subgrid dissipation in the LES models to the resolved dissipation ($\varepsilon_{sgs}/\varepsilon$ where $\varepsilon_{sgs} = 0$ in the DNS) is shown in figure 3.6f. The Ducros model yields the largest subgrid dissipation relative to resolved dissipation with the peak ratio reaching approximately 2.3. In contrast, the Dynamic Smagorinsky and WALE models showed nearly equivalent quantities of subgrid and resolved dissipation at their peak with ratios of 0.7 and 0.9, respectively.

The LES models also capture well the internal wave energy fluxes as indicated by the pressure-vertical velocity correlation, $-\langle p'w' \rangle$, in figure 3.6d. The wave energy flux is a sink of TKE, i.e. internal waves carry energy away from the shear layer. Since stratification in the ambient fluid is weak, wave energy fluxes are more than two orders of magnitude smaller than other terms in

the integrated budget. During the evolution of a stratified shear layer, internal waves are excited by two sources: first by KH instabilities and subsequently by broadband turbulence when billows break down with the instabilities producing a large wave flux. Furthermore, in order for KH instabilities to excite internal waves, the stratification must be sufficiently strong so that $Ri_0 > 0.18$ (Pham *et al.*, 2009). Since $Ri_0 = 0.12$, the KH instability in the present study does not excite internal waves. The wave energy flux is produced by the broadband turbulence where it should be noted that the peak energy fluxes occur after peak integrated dissipation. The evolution of the internal waves in the LES models shows good agreement with the DNS. In figure 3.6d, the peak wave fluxes produced by the LES fall within 5% of the value of the DNS.

The horizontally averaged and depth integrated values of TKE and terms in the TKE budget provide an overall view of LES model performance. We now move to the evolution of vertical profiles to better characterize the spatial dependence of LES model performance. Figure 3.7 shows the temporal evolution of TKE in the vertical using N_0t - z plots for the DNS and "x4" grid resolution LES cases. In the DNS, after transition to turbulence at $N_0t \approx 20$, TKE is concentrated in the core of the shear layer until $N_0t \approx 40$ at which time a double-lobed configuration is apparent with TKE concentrated at the edges of the billows in the transition layer. In the LES models, this trend is well captured although the concentration of TKE noted in the lobes at the billow edges between $40 < N_0t < 45$ is stronger than in the DNS.

Figure 3.8 shows the development of TKE production using N_0t - z plots for the DNS and "x4" grid resolution LES cases. In the DNS, production increases after transition to turbulence while its centerline value peaks at $N_0t \approx 25$. This behavior is also observed in the LES cases. Also apparent in the DNS is a near total collapse of production at $N_0t \approx 35$ followed by a secondary period of TKE production which persists until $N_0t \approx 50$. This late time production is contained in a double-lobed structure corresponding to the transition layers near the billow edges where shear intensifies. It is worth noting that the doubled-lobed feature in production has a counterpart in the N_0t - z plot of TKE. The "x4" resolution LES cases shown in figure 3.8 are able to capture the collapse in production followed by a period of recovery in the form of a double-lobed feature as

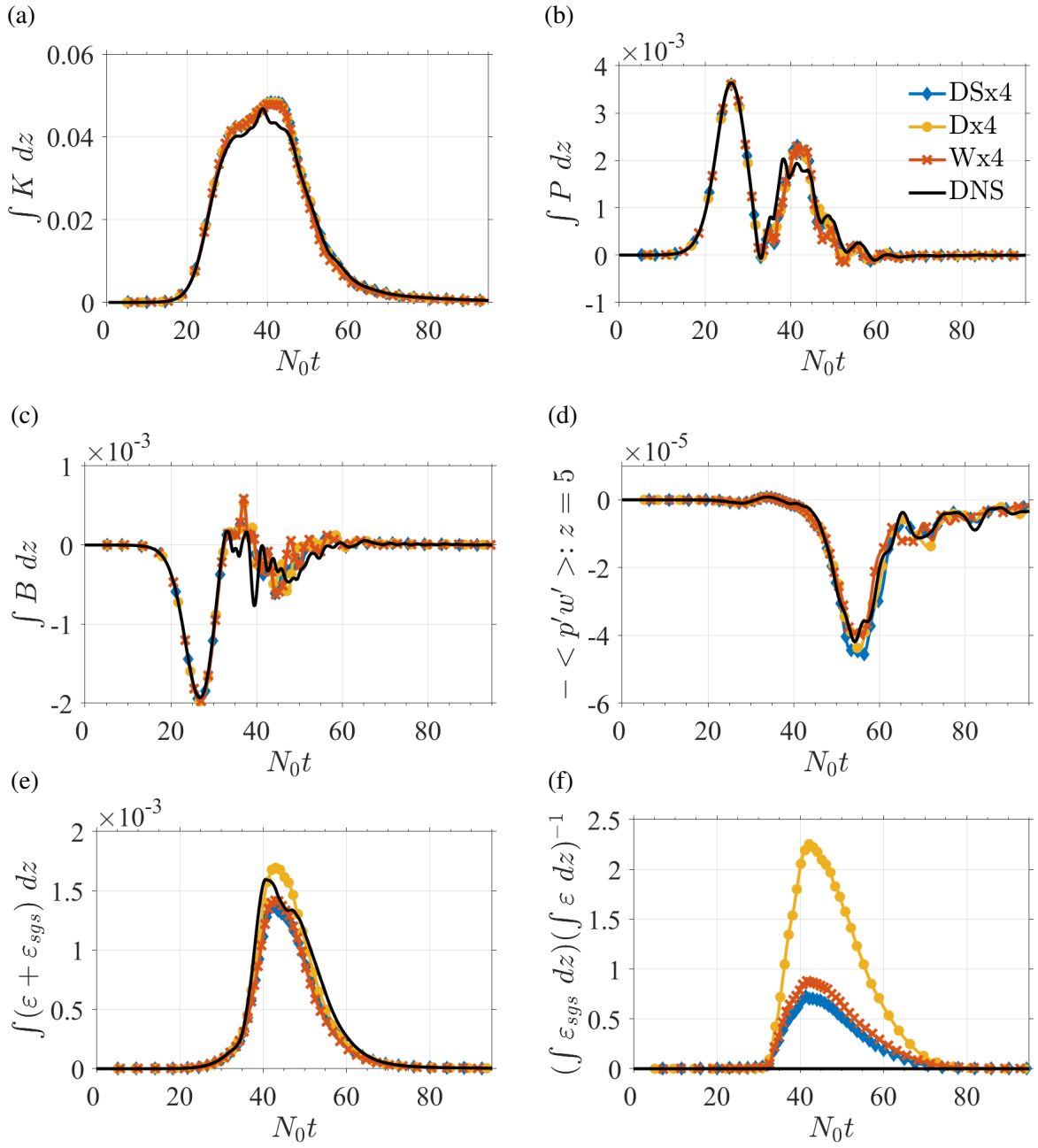

Figure 3.6: $N_0 t$ evolution of the nondimensional integrated TKE and TKE budget terms in the DNS and "x4" resolution LES cases: (a) TKE, (b) production, (c) buoyancy flux, and (e) total dissipation. The $N_0 t$ evolution of (d) $-\langle p'w' \rangle$ at $z = 5$ as well as (f) $\varepsilon_{sgs}/\varepsilon$ are also shown. TKE is normalized by $\Delta U^{*2} \delta^*_{\omega,0}$ while production, buoyancy flux, and dissipation are normalized by ΔU^{*3}. Values of $-\langle p'w' \rangle$ are normalized by $\rho_0 \Delta U^{*3}$.

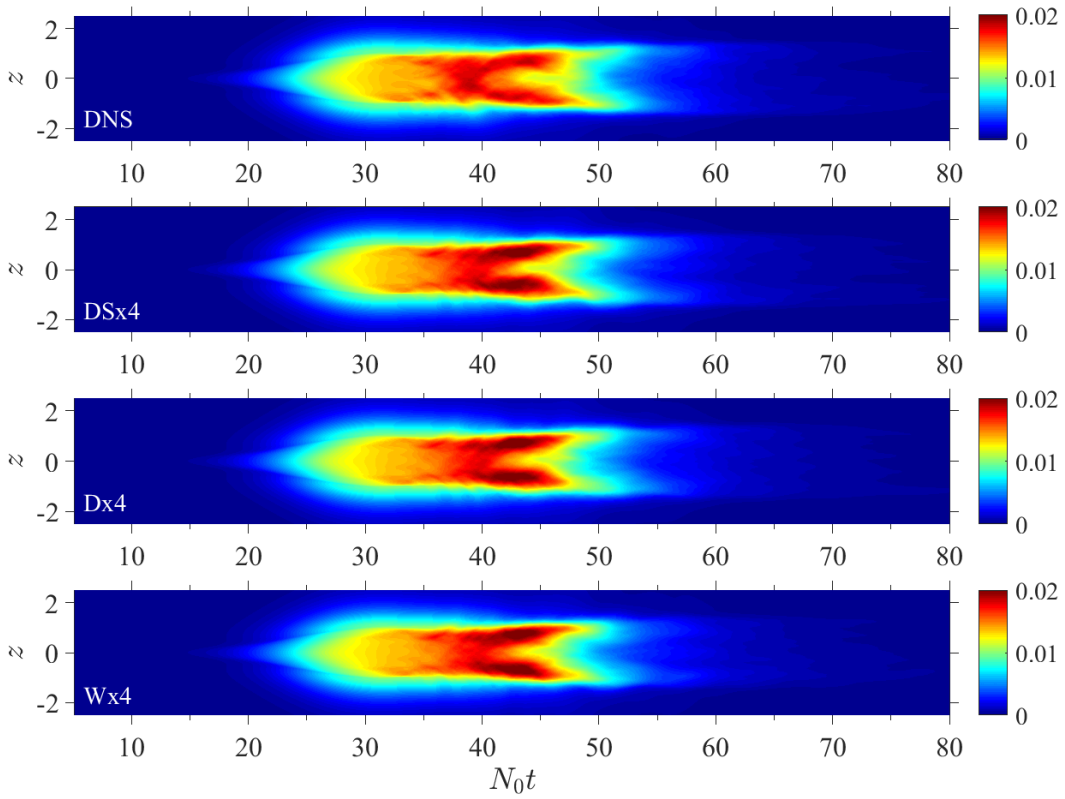

Figure 3.7: Comparison of TKE (K) using $N_0 t$ - z contours in the DNS and "x4" resolution LES cases.

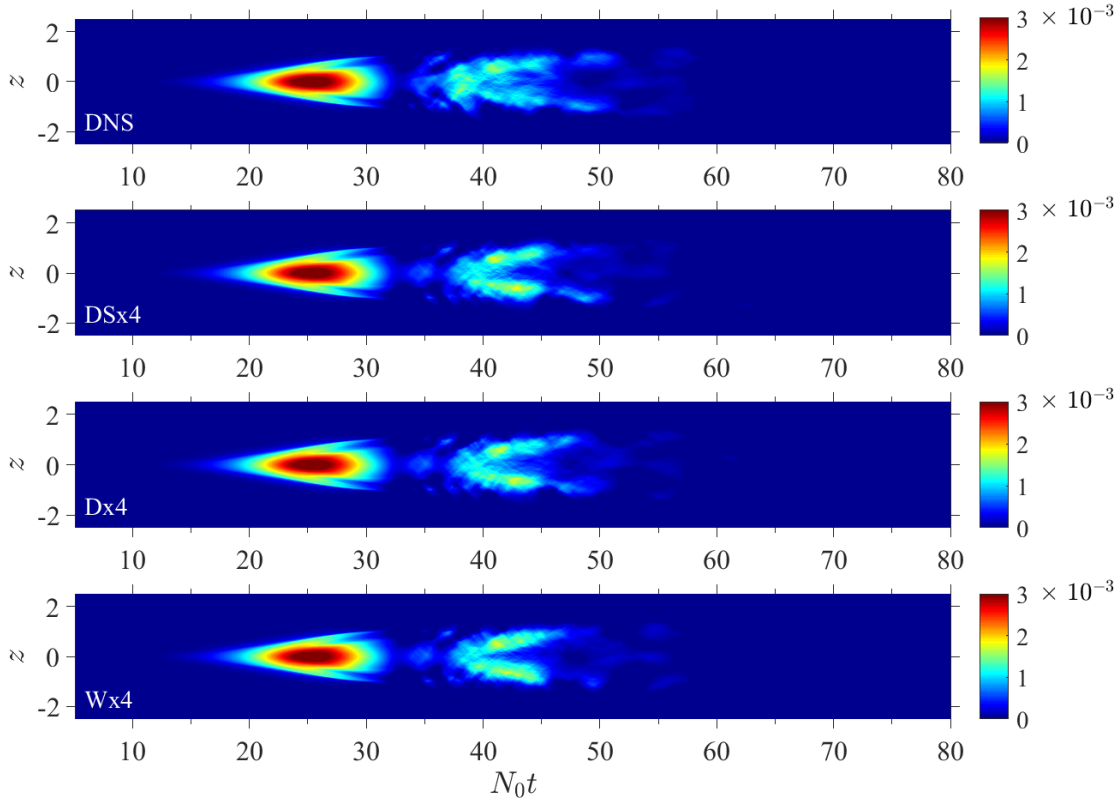

Figure 3.8: Comparison of TKE production (P) using N_0t - z contours in the DNS and "x4" resolution LES cases.

noted in the DNS.

Concurrent with the strong production at $N_0t = 25$ is the peak negative buoyancy flux seen in the DNS panel of figure 3.9. This behavior is well captured in the "x4" grid resolution LES cases. In the LES, there is stronger positive buoyancy flux at the center of the shear layer at $N_0t \approx 35$ which is consistent with the previous discussion of LES capture of integrated flux in figure 3.6c.

The development of total dissipation rate ($\varepsilon + \varepsilon_{sgs}$ where $\varepsilon_{sgs} = 0$ in the DNS) of TKE is depicted in figure 3.10 using N_0t - z plots. Here, clear differences are noted between the DNS and LES cases. The turbulent dissipation is significant during the second phase of production, after $N_0t \approx 35$, and not the earlier phase of turbulent production when the KH billows form. Although peak dissipation occurs at $N_0t \approx 40$ in all cases, there are differences in magnitude among the different models. A subtle double-lobed structure is observed in both the DNS and "x4" grid

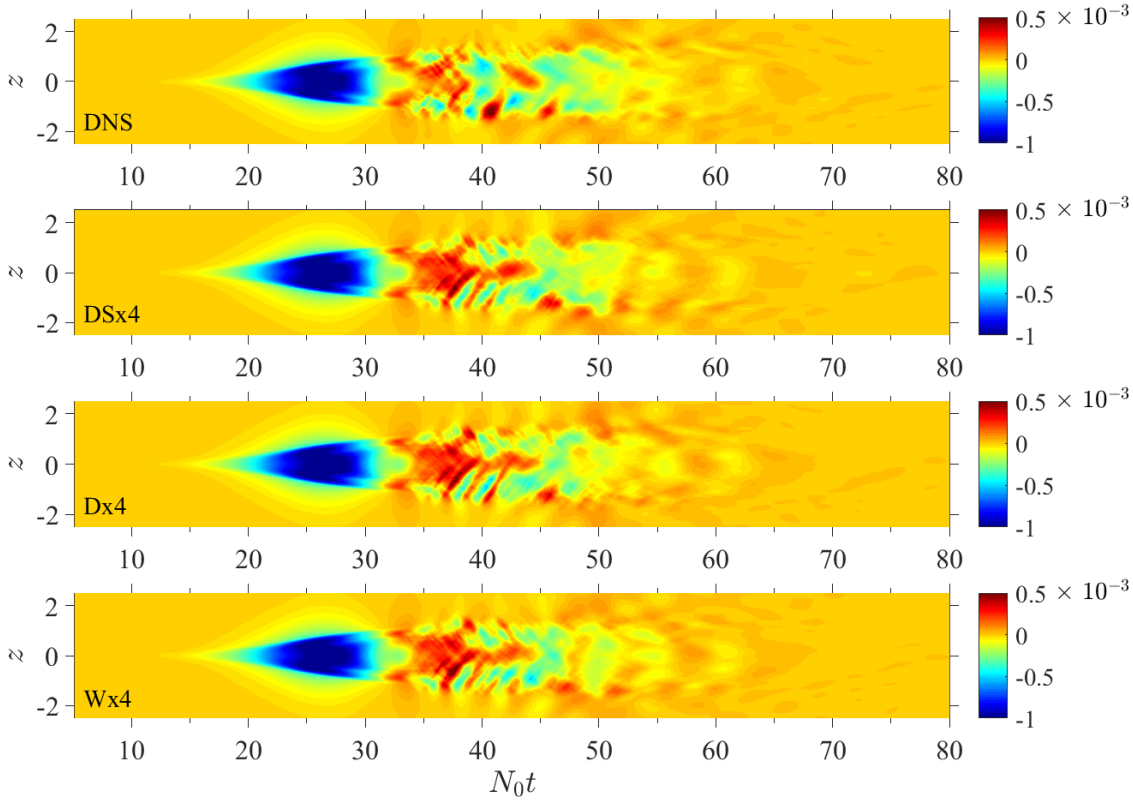

Figure 3.9: Comparison of TKE buoyancy flux (B) using $N_0 t$ - z contours in the DNS and "x4" resolution LES cases.

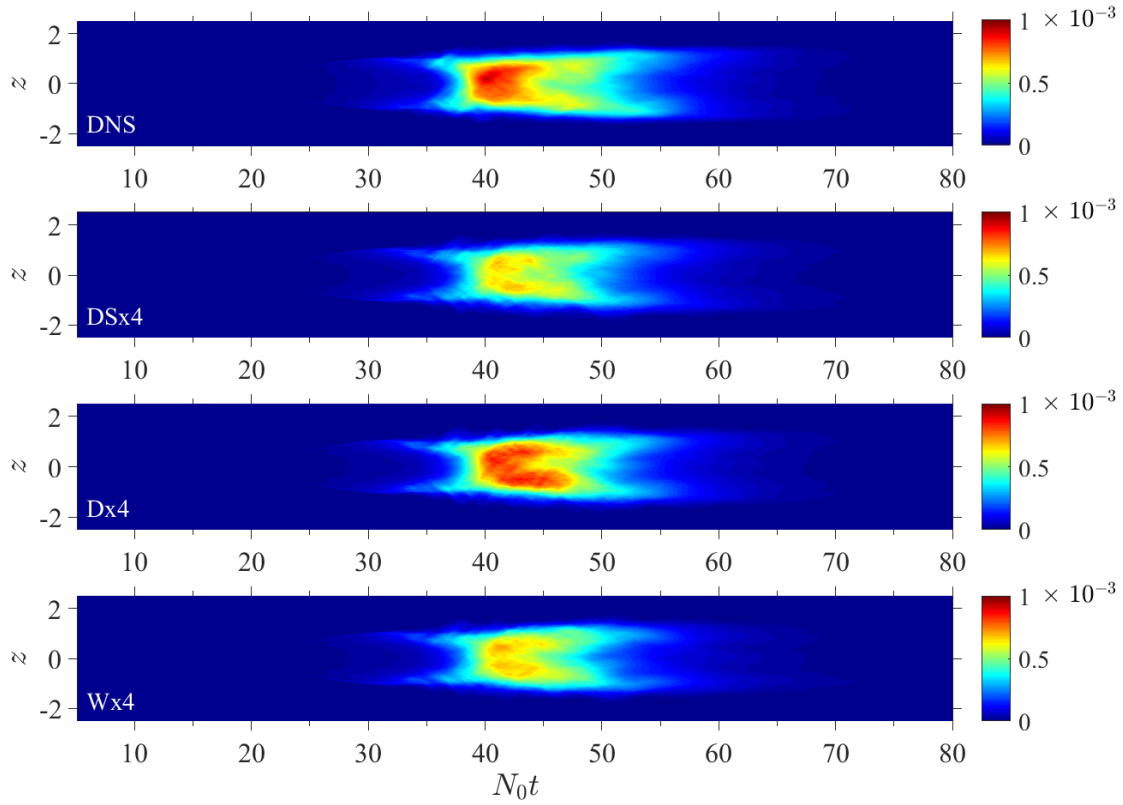

Figure 3.10: Comparison of TKE dissipation ($\varepsilon + \varepsilon_{sgs}$ where $\varepsilon_{sgs} = 0$ in the DNS), using N_0t - z contours in the DNS and "x4" resolution LES cases.

resolution LES cases. This indicates that, at certain times, turbulence is not being dissipated as strongly at the center of the shear layer. The Ducros model is shown to be better performing than the Dynamic Smagorinsky or WALE models at capturing dissipation rate and local dissipation magnitudes.

The depth integrated TKE budget terms can be further reduced to single, overall values by time integration where *iP* represents the value for production, *iD* the value for dissipation, and *iB* the value for buoyancy flux. Table 3.2 lists these values for the DNS and "x4" grid resolution LES cases. Using the DNS values as a benchmark, it is clear that all of the LES models sufficiently resolve the large scales of motion given that their maximum deviation from the value for production in the DNS is 6% while that of buoyancy flux is less than 1%. In the case of dissipation, which is dominated by smaller unresolved scales and is a more stringent test of subgrid model performance,

there are clear differences in the performance of the various LES models. Deviation from the DNS benchmark value ranges from nearly 20% in the Dynamic Smagorinsky and WALE cases to less than 4% in the Ducros case.

Table 3.2: Capture of TKE budget terms for the "x4" grid resolution LES cases. Singular values are obtained via trapezoidal time integration of the depth integrated TKE budget terms with results given for production (*iP*), dissipation (*iD*), and buoyancy flux (*iB*), in the DNS and "x4" grid resolution LES cases.

Case	Model	*iP*	*iD*	*iB*
DNS	DNS	0.1542	0.0806	0.0622
DSx4	Dynamic Smagorinsky LES	0.1506	0.0656	0.0624
Dx4	Ducros LES	0.1456	0.0777	0.0616
Wx4	WALE LES	0.1485	0.0647	0.0617

3.0.9 LES performance at coarse grid resolution

In an effort to quantify the performance of the LES models for a variety of circumstances, additional simulations were performed for each of the three subgrid models with a horizontal grid that is coarser that the "x4" grid resolution cases by a factor of two. The following section reports the evolution of the shear layer captured in these "x8" grid resolution LES cases as compared to the DNS.

3.0.10 Flow evolution

Even with "x8" grid resolution, all of the LES models are able to capture the evolution of the primary KH shear instabilities which have large horizontal wavelengths. Take for instance, the density perturbations at time $N_0 t = 32$ in figure 3.11 depicting the instabilities over the x - z plane in the Ducros LES case. The nonlinear development of the KH instabilities into billows is well captured by the LES with coarser grid resolution. However, the development of secondary shear instabilities along the braids between the billows which is observed in the DNS and well captured by the finer grid resolution LES, is obscured at the coarser grid resolution. This is evident on comparison of the DNS (braid and billow periphery between $4 < x < 7$ in the $N_0 t = 35$ panel of

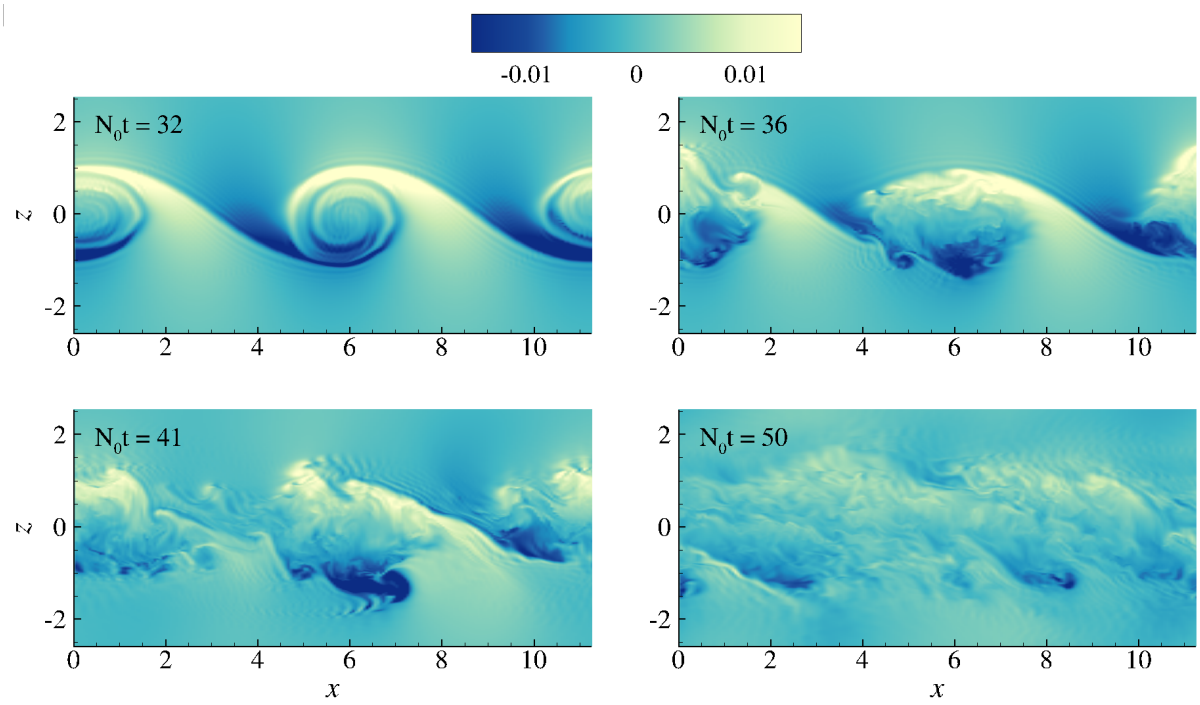

Figure 3.11: Snapshots of density perturbations over the x - z plane at various times in the Ducros "x8" grid resolution LES case.

figure 3.1) with the corresponding region in the LES ($N_0t = 36$ panel of figure 3.11). Furthermore, the distinct pockets of heavier (lighter) fluid in the upper (lower) side apparent in the DNS at the two later times are mixed in the LES.

As in the "x4" grid resolution LES cases, momentum thickness (δ_θ) normalized by initial momentum thickness ($\delta_{\theta,0}$) is used to illustrate the growth of the shear layer. Figure 3.12 gives a comparison of the "x8" grid resolution LES cases with the DNS. The periods of linear growth of δ_θ noted between $20 < N_0t < 30$ and $35 < N_0t < 50$ are again captured by the LES cases as are the plateaus indicative of growth stagnation. As in the "x4" grid resolution LES cases, the final plateau commences slightly earlier in the "x8" grid resolution LES cases than in the DNS. However, the maximum momentum thickness in the LES is again only 4% less than the DNS and as such, the coarser grid resolution LES cases still pick up the evolution of the mean velocity.

There were no significant differences in the capture of shear (S^2), local buoyancy frequency (N^2), or gradient Richardson number (Ri_g) between the "x4" and "x8" grid resolution LES cases. These results are not included for conciseness.

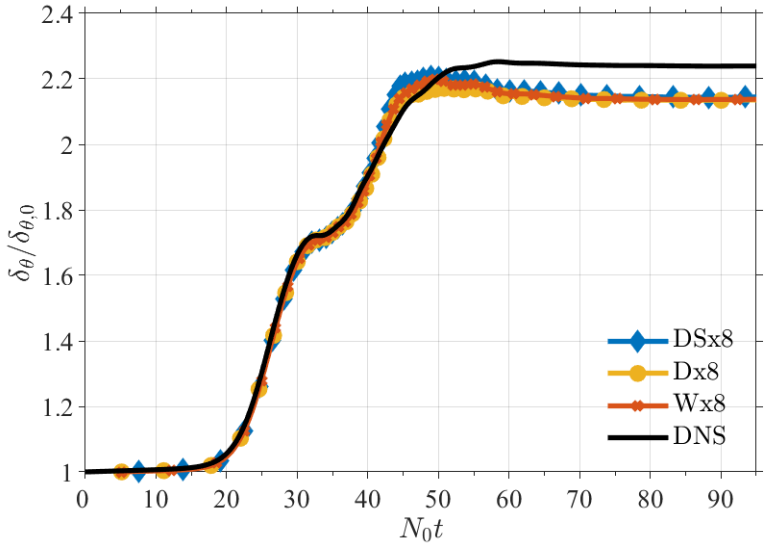

Figure 3.12: N_0t evolution of momentum thickness (δ_θ) normalized by initial momentum thickness ($\delta_{\theta,0}$) in the DNS and "x8" resolution LES cases.

3.0.11 Turbulent kinetic energy evolution

The temporal evolution of TKE and TKE budget terms are shown using horizontally averaged and depth integrated values in figure 3.13. Although the trends in the DNS are captured by "x8" grid LES cases, there are some quantitative differences with the finer resolution cases as elaborated below.

In figure 3.13a, the transition to turbulence and the final decay rate are well captured, although the peak TKE in the "x8" grid resolution LES cases is larger in magnitude than in the "x4" grid resolution LES cases by nearly 15%. Figure 3.13b gives the evolution of integrated production. The initial peak in production at $N_0t \approx 25$ is well captured indicating proper representation of the primary and secondary instabilities. However, the fully three-dimensional regime associated with the secondary peak in production is not well represented and the second peak at $N_0t \approx 40$ is much higher than either the DNS or the "x4" grid resolution LES cases. In particular, the maximum value of the second peak is nearly 25% larger than in the finer resolution LES cases. The buoyancy flux profiles of figure 3.13c also show increased discrepancies between the DNS and "x8" grid resolution LES cases. There is overestimation of the positive buoyancy flux between $30 < N_0t < 35$

as in the finer resolution LES cases. However, there is now a much larger overestimation in the secondary peak of negative buoyancy flux at $N_0t \approx 45$. This is consistent with the overestimation of production around this time. Figure 3.13e shows the temporal evolution of total dissipation for the DNS and "x8" grid resolution LES cases. The location of peak dissipation at $40 < N_0t < 43$ in the different models is consistent with the DNS and the finer resolution LES cases. There was negligible change in the magnitude of peak dissipation between the "x4" and "x8" grid resolution Dynamic Smagorinsky and WALE cases. However, there was an approximately 10% increase in the magnitude of peak dissipation in the "x8" grid resolution Ducros model case. Also of interest are the steeper (relative to the DNS) decay rates of dissipation in the "x8" grid resolution LES cases. At coarser grid resolution, the subgrid stresses become stronger and the resolved turbulence decays at a faster rate relative to the turbulence in the DNS. This is consistent with the larger ratios (relative to the "x4" grid resolution LES cases) of subgrid dissipation in the LES models to the resolved dissipation ($\varepsilon_{sgs}/\varepsilon$ where $\varepsilon_{sgs} = 0$ in the DNS) shown in figure 3.13f. In the case of the Ducros model, the ratio of these quantities nearly tripled those of the "x4" grid resolution results while the values in both the Dynamic Smagorinsky and WALE cases doubled.

Finally, coarsening the grid resolution increases the internal wave energy flux as indicated in figure 3.13d. Recall, the peak wave fluxes in the "x4" grid resolution LES cases are at most 5% larger than the value seen in the DNS (figure 3.6d). As seen in the "x8" grid resolution LES cases shown in figure 3.13d, the discrepancy increases to 30% with the Dynamic Smagorinsky and Ducros models having the largest difference with the DNS. The larger internal wave flux in the LES is due to increased production at $N_0t \approx 40$ in figure 3.13b. When the billows break down into turbulence, the LES models produce a stronger Reynolds stress, $\langle u'w' \rangle$, and thus, a stronger production. Stronger Reynolds stress also results in a stronger internal wave field. Nevertheless, since the wave energy fluxes are small relative to other terms in the TKE budget, the discrepancy in the wave flux between the LES and the DNS does not affect the overall evolution of the TKE.

Focusing now on the spatial variation of TKE, figure 3.14 depicts the temporal evolution of TKE in the vertical using N_0t - z plots for the DNS and "x8" grid resolution cases. While the

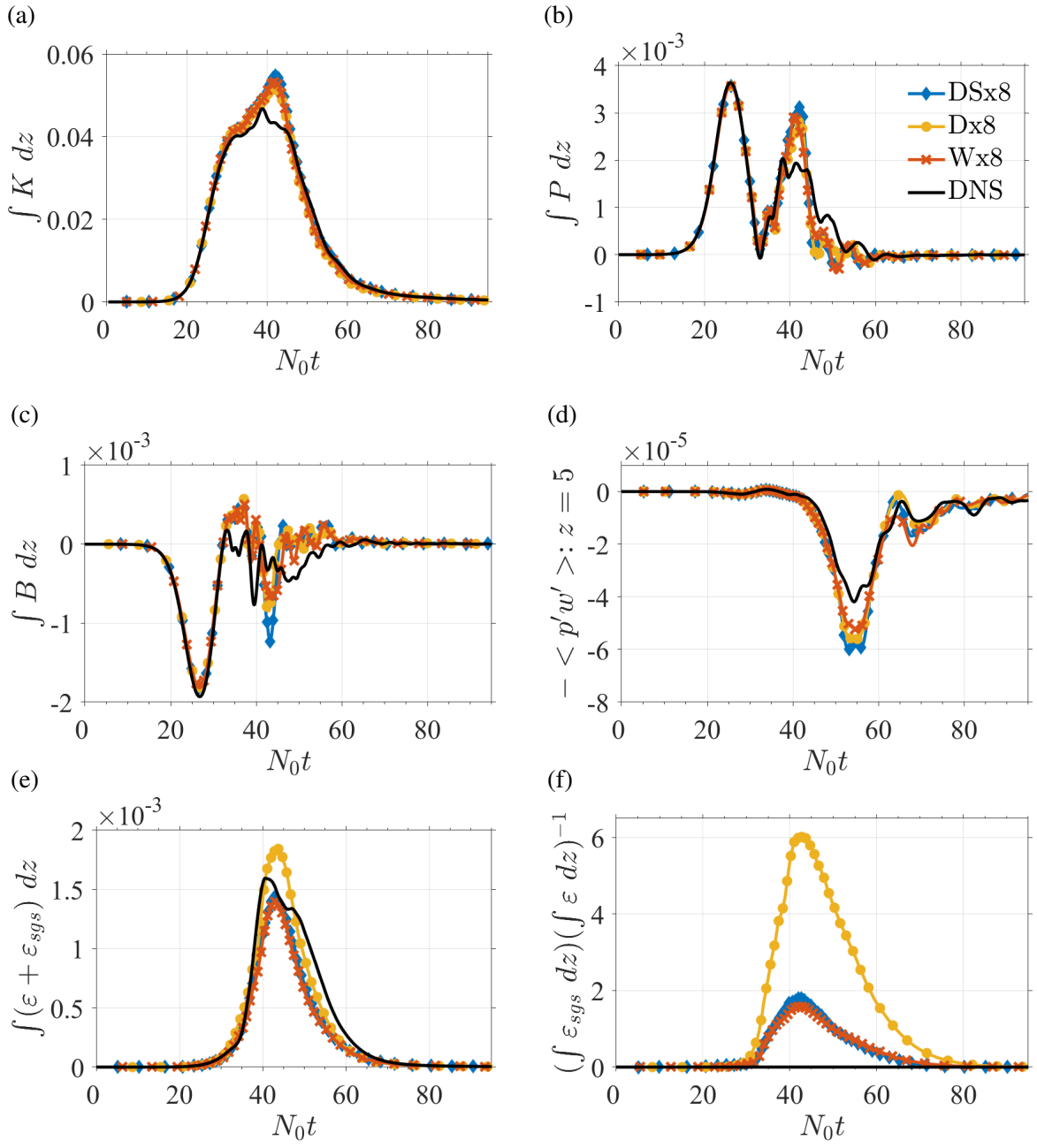

Figure 3.13: $N_0 t$ evolution of the nondimensional integrated TKE and TKE budget terms in the DNS and "x8" resolution LES cases: (a) TKE, (b) production, (c) buoyancy flux, and (e) total dissipation. The $N_0 t$ evolution of (d) $-\langle p'w' \rangle$ at $z = 5$ as well as (f) $\varepsilon_{sgs}/\varepsilon$ are also shown. TKE is normalized by $\Delta U^{*2} \delta^*_{\omega,0}$ while production, buoyancy flux, and dissipation are normalized by ΔU^{*3}. Values of $-\langle p'w' \rangle$ are normalized by $\rho_0 \Delta U^{*3}$.

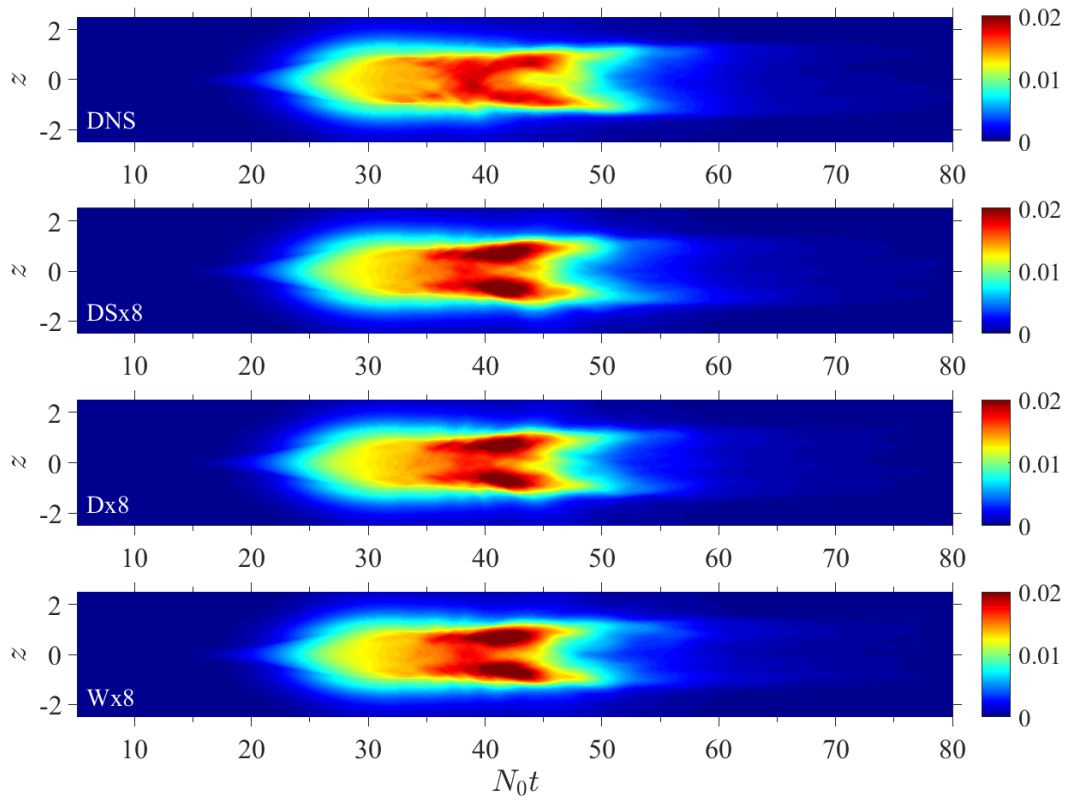

Figure 3.14: Comparison of TKE (K) using N_0t - z contours in the DNS and "x8" resolution LES cases.

redistribution of shear to the billow edges at $N_0t \approx 40$ is captured in the coarser resolution LES, even stronger packets of TKE are noted in the lobes at the billow edges between $40 < N_0t < 45$ than in the DNS or finer resolution LES cases.

Taking a closer look at the spatial variation of the budget terms, figure 3.15 shows the N_0t evolution of vertical profiles of turbulent production for the DNS and "x8" grid resolution LES cases. Although the peak and subsequent collapse at $N_0t = 35$ are correctly represented, production is noted to have higher concentration in the lobes of the "x8" grid resolution LES cases than in the DNS or finer resolution LES cases. The subsequent decay of production is also observed to be much more rapid in the "x8" grid resolution LES cases.

The buoyancy flux N_0t - z plots of figure 3.16 tell a similar story. While the overall behavior is consistent with the DNS and finer resolution LES cases, the pockets of strong positive buoyancy

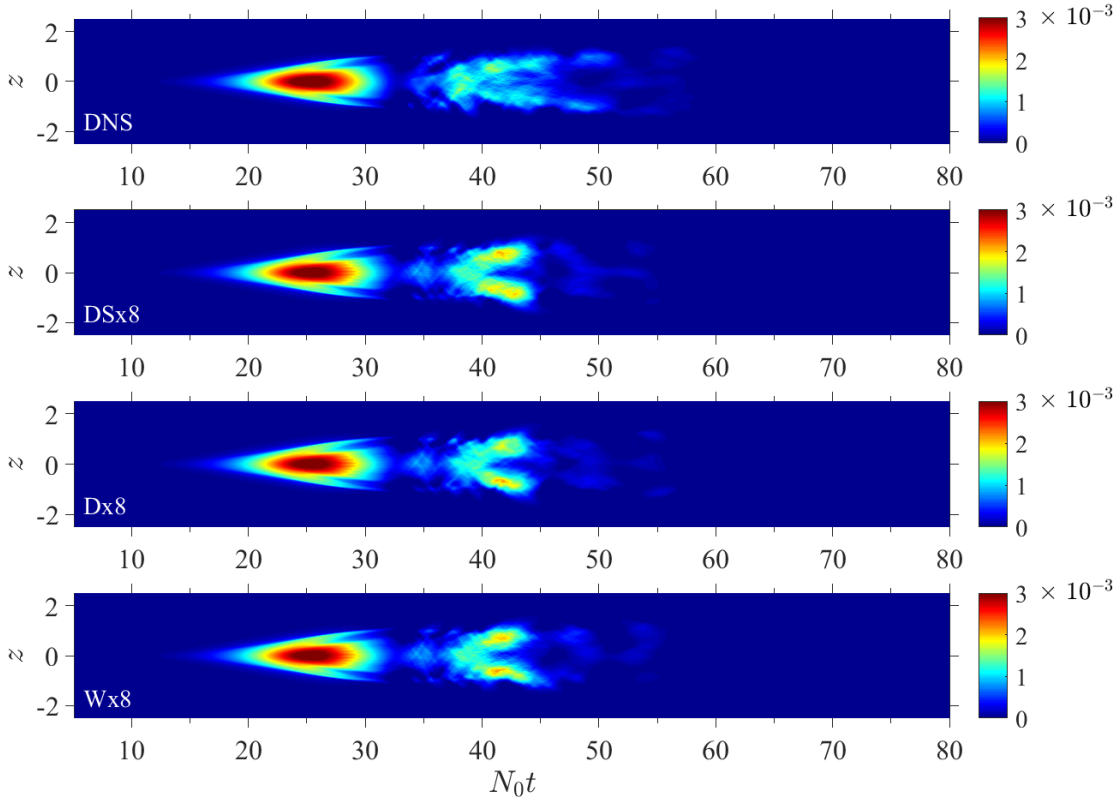

Figure 3.15: Comparison of TKE production (P) using N_0t - z contours in the DNS and "x8" resolution LES cases.

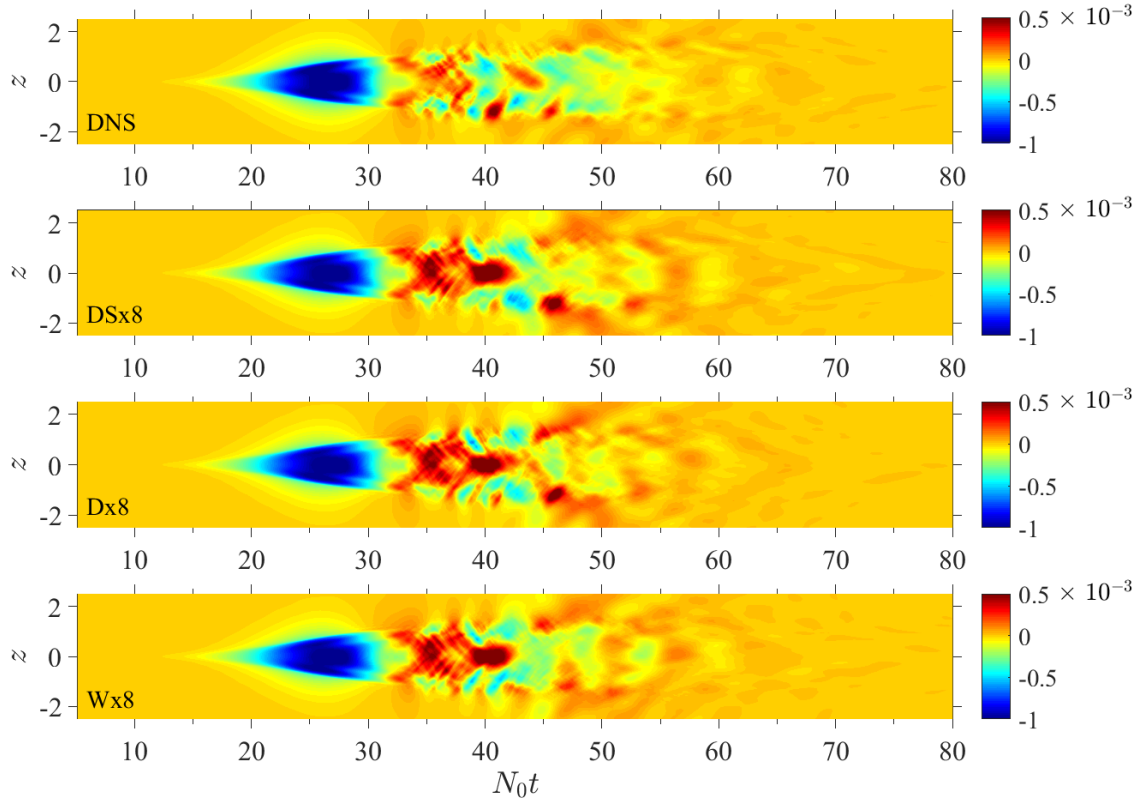

Figure 3.16: Comparison of TKE buoyancy flux (B) using N_0t - z contours in the DNS and "x8" resolution LES cases.

flux are enhanced in the "x8" grid resolution LES cases.

The total dissipation rate ($\varepsilon + \varepsilon_{sgs}$ where $\varepsilon_{sgs} = 0$ in the DNS) of TKE is analyzed in the N_0z - t plots of figure 3.17. Although the Ducros model remains the best performing of the three LES models employed, dissipation decays more rapidly with smaller dissipation seen at the edges of the shear layer in the "x8" grid resolution LES cases. The Dynamic Smagorinsky and WALE model cases have lost much of their double-lobed structure indicating that dissipation is occurring fairly evenly throughout the shear layer as opposed to being concentrated at the billow edges and turbulent core in the DNS. Thus, the spatial distribution of the dissipation is not well captured at such coarse grid resolution as that in the "x8" LES cases.

As in the case of the "x4" grid resolution LES cases, integration in time can be used to reduce the depth integrated TKE budget terms to single values where iP represents the value for

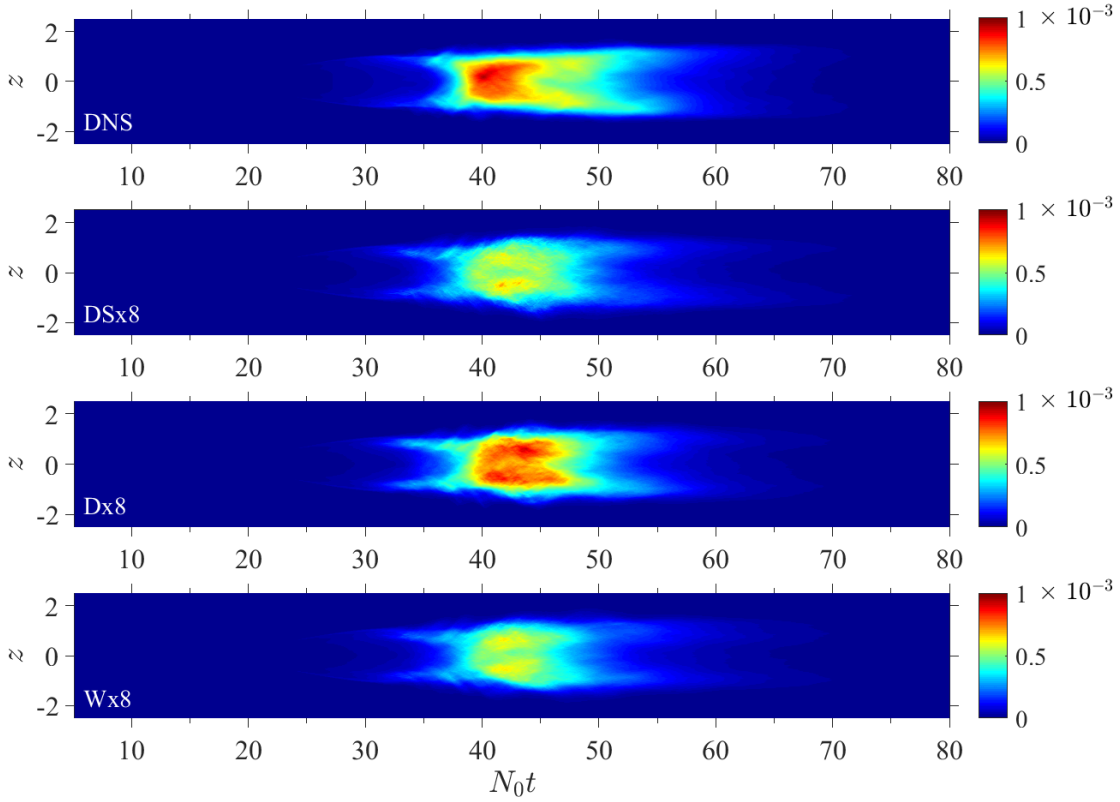

Figure 3.17: Comparison of TKE dissipation ($\varepsilon + \varepsilon_{sgs}$ where $\varepsilon_{sgs} = 0$) in the DNS, using N_0t - z contours in the DNS and "x8" resolution LES cases.

production, *iD* the value for dissipation, and *iB* the value for buoyancy flux. Table 3.3 lists these values for the DNS and "x8" grid resolution LES cases. As in the "x4" grid resolution LES cases, the results of the coarser simulations indicate that all of the LES models still sufficiently resolve the large scales of motion given that their maximum deviation from the DNS value for production is 7% while that of buoyancy flux is approximately 3%. Clear differences in the performance of the various LES models are again apparent in the capture of dissipation. Deviation from the DNS benchmark value ranges from 28% in the WALE case to less than 4% in the Ducros case. Interestingly, the WALE model exhibits high variability with differing grid resolution. It yields a 8% drop in dissipation capture with the coarsened grid resolution in contrast to the smaller percentage losses of the Dynamic Smagorinsky and Ducros cases. The Ducros case shows negligible change in dissipation with the coarsened grid and little variability among production and buoyancy flux suggesting possibly higher reliability when utilizing different grids than the other models.

Table 3.3: Capture of TKE budget terms for the "x8" grid resolution LES cases. Singular values are obtained via trapezoidal time integration of the depth integrated TKE budget terms with results given for production (*iP*), dissipation (*iD*), and buoyancy flux (*iB*), in the DNS and "x8" grid resolution LES cases.

Case	Model	*iP*	*iD*	*iB*
DNS	DNS	0.1542	0.0806	0.0622
DSx8	Dynamic Smagorinsky LES	0.1560	0.0614	0.0628
Dx8	Ducros LES	0.1429	0.0766	0.0601
Wx8	WALE LES	0.1559	0.0580	0.0618

3.0.12 Turbulent transport in the LES

In previous sections, it was demonstrated that the evolution of the shear layer is similar between the DNS and various LES models in terms of the shear layer thickness and mean statistics as well as the first and second moment turbulence statistics. In this section, a comparison is performed to investigate whether the LES models are successful in capturing the turbulent transport coefficients that are produced in the DNS. Specifically, the evolution of the eddy viscosity (ν_T) and eddy diffusivity (κ_T) are quantified. These terms are responsible for mixing of the momentum and

density fields, respectively, and are defined as follows

$$\nu_T = \nu_{sgs} + \frac{\langle u'w' \rangle}{d\langle u \rangle / dz}, \tag{3.24a}$$

$$\kappa_T = \kappa_{sgs} + \frac{\langle \rho'w' \rangle}{d\langle \rho \rangle / dz}, \tag{3.24b}$$

where the second terms on the right hand side of both equations are the contribution of resolved eddy motions.

Figure 3.18a compares the evolution of the subgrid viscosity (ν_{sgs}) at the center of the shear layer among the simulations with "x4" grid resolution. Since the LES are well resolved, ν_{sgs} is at most twice as large as the molecular viscosity (ν). The Ducros model produces the largest ν_{sgs} which is consistent with the large subgrid dissipation noted for this model when compared to the other LES models. It is noted that the subgrid viscosity of the WALE model is elevated during the growth period of the KH instability, i.e. between $20 < N_0 t < 35$. During this time period, the KH instabilities generate fluctuations in the velocity and density fields although the fluctuations occur at scales that are orders of magnitude larger than the diffusive scale, e.g. the Kolmogorov length scale. The fluctuations generate strain and vorticity fields which cause the WALE model to produce its increased ν_{sgs}. The subgrid viscosity increases as the grid resolution becomes coarser as demonstrated in figure 3.18b. In the "x8" grid resolution LES cases, the peak ν_{sgs} in the Ducros model reaches up to 5.5 times larger than ν while the values in the other two models are approximately 1.5 times larger. The larger value of ν_{sgs} in the Ducros model is responsible for producing more turbulent dissipation than seen in the DNS as shown in the "x8" grid resolution cases in contrast to the underestimate by the other two models.

The evolution of eddy viscosity normalized by the molecular value (ν_T/ν) at the center of the shear layer ($z = 0$) is compared among the cases in figures 3.18c-3.18d. Overall, the LES models capture the evolution of ν_T/ν well during the growth period of the KH shear instabilities until $N_0 t \approx 35$ regardless of grid resolution. When the KH rollers break down into turbulence at $N_0 t = 40$, the value of ν_T/ν in the LES models surpasses that of the DNS. For the "x4" grid

resolution LES cases, the WALE model produces the largest peak value of eddy viscosity while the value in the Ducros model is closest to that of the DNS. During the turbulence decay period, i.e. after $N_0 t \approx 40$, the values of ν_T/ν in the LES cases decrease at a faster rate relative to the DNS. The eddy viscosities in the LES also decrease faster than the subgrid viscosity during this period. This suggests that the reduction in eddy viscosity is dominated by the fast reduction of the resolved turbulence. The overshoot of peak eddy viscosity in the LES cases at $N_0 t = 40$ causes the turbulence to decay faster than in the DNS. As the grid resolution is coarsened, the difference in the peak value of ν_T/ν between the DNS and LES becomes more pronounced as shown in figure 3.18d. The Dynamic Smagorinsky and WALE models show peak values nearly three times larger than that of the DNS while the peak value in the Ducros model is in closer agreement. With the increased overshoot of peak ν_T/ν, turbulence in the "x8" grid resolution LES cases decays significantly faster than in the "x4" grid resolution LES cases.

Since the Ducros and WALE models use a subgrid Prandtl number of unity, i.e. ν_{sgs} (already reported in figures 3.18a-3.18b) and subgrid diffusivity (κ_{sgs}) are equal, attention is focused on the performance of the eddy diffusivity (κ_T) in the LES cases. Figures 3.18e-3.18f compare the evolution of κ_T/κ at the center of the shear layer. It is clear that the evolution of κ_T/κ is quite different from that of ν_T/ν, notably during the later stage of turbulence driven linear growth of δ_θ when the transport of momentum and density are driven by different physics. During the earlier stage corresponding to the growth period of the KH instabilities, a positive $\langle \rho' w' \rangle$ is produced as the instability disturbs the density interfaces. While values of ν_T in the LES agree well with DNS during this early period, κ_T is similarly under predicted by the LES models. Differences between the LES and the DNS suggest that $Pr_{sgs} < 1$ during $N_0 t < 25$, i.e. the use of a unity Pr_{sgs}, may not be appropriate during this period when the flow is dominated by large-scale instability fluctuations. As the KH billows develop between $35 < N_0 t < 40$, heavier fluid from the lower half of the shear layer is transported upward while lighter fluid from the upper half is transported downward resulting in an unstable density gradient with a significant amount of available potential energy to drive convective turbulence, i.e. the negative $\langle \rho' w' \rangle$ during this period. All of the LES models overshoot

the magnitude of negative eddy diffusivities in the DNS during this period. This is consistent with the large positive buoyancy flux previously noted. The magnitude of negative κ_T becomes larger in the "x8" grid resolution LES cases. Coarser grid resolution further exaggerates the effects of convective turbulence resulting in an overestimation of the density field mixing. Overall, the LES models do not accurately capture density transport during the stage of the stratified shear layer in which convective turbulence dominates.

3.0.13 Computational cost

The relative computational cost of the LES models is assessed by calculating the required CPU time per grid point per time step (T_{CPU}) given by

$$T_{CPU} = \frac{N_p \times T_{wall,275}}{N_t \times N_g} \tag{3.25}$$

where N_p is the total number of processes, $T_{wall,275}$ is the simulation wall time required to reach $t = 275$, N_t is the total number of time steps, and N_g is the total number of grid points ($N_x \times N_y \times N_z$). The total cost of each simulation (T) is thus calculated using $T = T_{CPU} \times N_t \times N_g$. The values of T_{CPU} (given in CPU seconds/time step/grid point) and T (given in CPU hours) are summarized in table 3.4 for the DNS and LES cases. All simulations (DNS and LES) were performed on the Cray XC40 Navy DSRC machine, Gordon.

Table 3.4: Computational cost assessment. An estimation of the required CPU time per grid point per time step (T_{CPU}) and the total computational cost (T) are given for the DNS and LES cases. The units for T_{CPU} are CPU seconds/time step/grid point while T is given in CPU hours.

Case	Model	T_{CPU}	T
DNS	DNS	3.95×10^{-6}	3.7×10^{4}
DSx4	Dynamic Smagorinsky LES	2.34×10^{-5}	5.1×10^{3}
Dx4	Ducros LES	4.60×10^{-6}	9.7×10^{2}
Wx4	WALE LES	5.39×10^{-6}	1.1×10^{3}
DSx8	Dynamic Smagorinsky LES	1.83×10^{-5}	7.5×10^{2}
Dx8	Ducros LES	4.89×10^{-6}	1.9×10^{2}
Wx8	WALE LES	5.45×10^{-6}	2.2×10^{2}

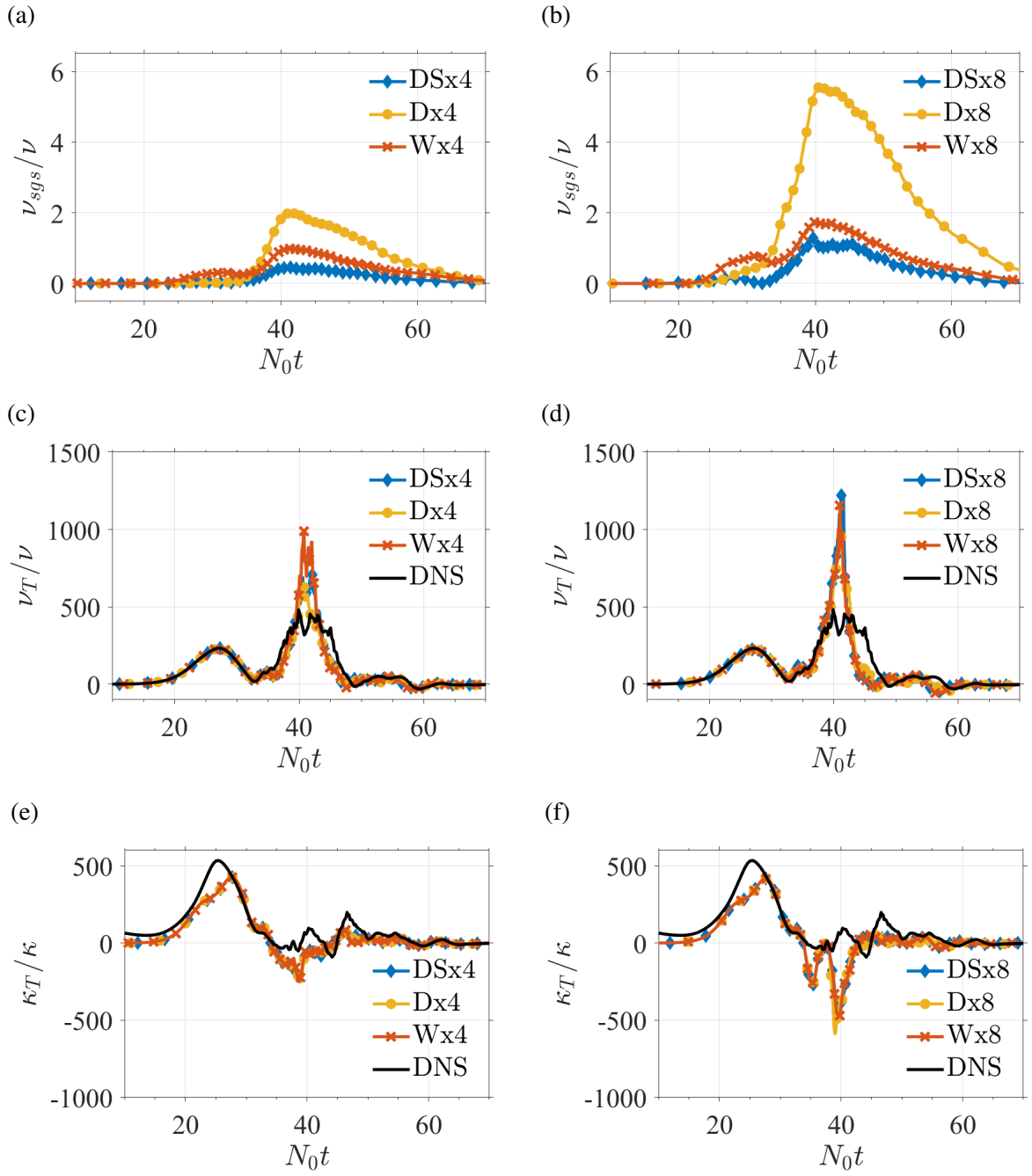

Figure 3.18: N_0t evolution of (a,b) normalized subgrid viscosity (ν_{sgs}/ν), (c,d) normalized eddy viscosity (ν_T/ν), and (e,f) normalized eddy diffusivity (κ_T/κ) at the center of the shear layer where $z = 0$ in the DNS and LES cases: (a,c,e) "x4" grid resolution LES cases and (b,d,f) "x8" grid resolution LES cases.

Of the LES models, the Dynamic Smagorinsky model incurs the highest computational cost with T_{CPU} values on the order of $O(10^{-5})$. In contrast, the WALE and Ducros models have T_{CPU} values 3 - 5 times smaller. The WALE model is slightly more computationally costly ($T_{CPU} \approx 5.4 \times 10^{-6}$) than the Ducros model ($T_{CPU} \approx 4.7 \times 10^{-6}$).

From the values of T in table 3.4, the computational cost of the DNS is 3.7×10^4 CPU hours to reach $t = 275$. As expected, the LES models are shown to be much less computationally costly. The "x4" grid resolution cases require anywhere from approximately 7 - 40 times fewer CPU hours than the DNS with the Ducros model requiring the least amount of CPU hours and the Dynamic Smagorinsky the most. Coarsening the horizontal grid resolution by a factor of two between the "x4" and "x8" grid resolution LES cases results in at least an order of magnitude difference in the total computational cost. The "x8" grid resolution cases require approximately 50 - 200 times fewer CPU hours than the DNS. The Ducros model required only 200 CPU hours, a small fraction of the 3.7×10^4 CPU hours required in the DNS to reach $t = 275$.

3.0.14 Conclusions

A comprehensive investigation of three LES models was performed to assess their ability in simulating the evolution of a localized layer of vertical shear in a uniformly stratified background. The Dynamic Smagorinsky, Ducros, and WALE models were chosen due to their use in previous literature and a comparison was performed to assess potential advantages for future work. The results of simulations with moderate Reynolds number, $Re_0 = 24,000$, were compared to a DNS at the same Re_0 to assess their performance. The LES were conducted on a fine grid ("x4" series) with a fourth of the DNS grid spacing in the horizontal and also another grid coarsened by another factor of two ("x8" series). Flow evolution was quantified using plots of momentum thickness which showed good agreement between the DNS and all LES cases. The LES models were also shown to accurately capture the vertical profiles of mean shear, buoyancy frequency, and gradient Richardson number, thereby assuring that the mean flow was well handled by the models. Billow evolution and development of secondary instabilities were consistent with DNS results although the "x8" grid

resolution tended to obscure small-scale features present in the DNS such as secondary billows and pockets of relatively unmixed fluid.

The growth and decay of turbulent kinetic energy are well captured by all of the LES models although there was a 10% increase in the magnitude of peak TKE in the "x8" grid resolution LES cases when compared to their finer resolution counterparts. The TKE production in the DNS exhibits two distinctive peaks with a collapse in between. Both peaks in production as well as the total collapse observed at $N_0 t \approx 30$ are well captured in the LES models, regardless of grid resolution, although there are some differences in the magnitude of the second peak. The first phase of TKE production is associated with the roll up of the KH billow and has negligible dissipation. The dissipation becomes appreciable later during the second phase of TKE production. An analysis of the dissipation revealed discrepancies between the DNS and the LES models. The Ducros model is found to better capture the dissipation rate profiles.

The buoyancy flux is negative definite during the initial development ($N_0 t < 30$), a period when the LES results are accurate. Later in time, there are regions of convective turbulence where the magnitude of the buoyancy flux is overestimated leading to a discrepancy in the horizontally averaged and depth integrated value that is minor in the "x4" series but larger in the "x8" series.

When comparing turbulent transport of the momentum and density fields, it was found that the all three LES models capture well the eddy viscosity during the growth period of the KH billows, i.e., the first phase of TKE production. When the KH billows break down, the LES models overshoot the value of eddy viscosity seen in the DNS with the Ducros model producing the smallest discrepancy. Similarly, the eddy diffusivity of density attains larger values than those of the DNS. The LES models do not sufficiently capture the physics of convective turbulence.

Recent work, e.g. Khani (2018), has shown the Dynamic Smagorinsky model capable of capturing turbulence evolution in homogenous stratified turbulence. The evolution of the stratified shear layer configuration of the present study involves a combination of physics characteristic to both shear driven and convectively driven turbulence. Future development of subgrid models and their evaluation over a broad range of flows will help make progress in LES of stratified turbulent

flow.

An analysis of the relative computational costs revealed the LES models to require anywhere between 7 - 200 times fewer CPU hours than the DNS. The Ducros model is shown to be the least expensive LES model employed in terms of CPU time per grid point per time step as well as overall CPU hours while the Dynamic Smagorinksy is deemed the most expensive. Although the Dynamic Smagorinksy and WALE models have benefits and may be appropriate choices for certain flow configurations, given the results presented, the Ducros model is the most appropriate choice for future work similar to the problem described in this work.

Chapter 3 is a reprint of material under review for publication as follows: A. VanDine, H. T. Pham, S. Sarkar, "Investigation of LES models for a stratified shear layer", *Comput. Fluids*, 2019. The author of this dissertation is the primary investigator and author of this work.

Chapter 4

Hybrid spatially-evolving DNS model of flow past a sphere

The specific case of the wake produced behind a towed sphere is considered for the introduction of the hybrid spatially-evolving DNS model. Experiments for a towed wake are typically conducted by towing the body and taking measurements in a region that is fixed in space. In a frame that moves with the body, the velocity profile of the fluid behind the body shows a defect with respect to the free-stream velocity of the surrounding fluid (U_∞). The representation of a towed wake utilized in this work is shown in figure 4.1 with a mean streamwise velocity profile, $\langle u_1(x_2,x_3)\rangle$. A spatially-evolving approximation of the flow is given, whereby streamwise evolution of statistics rather than their temporal evolution may be examined. In comparisons with corresponding temporally-evolving simulations, the downstream distance (x_1) relates to time (t) as $x_1 = tU_\infty$. As such, a nondimensional time unit (used in averaging during the calculation of statistics) can be defined as tU_∞/D where D is the characteristic diameter of the sphere.

As previously discussed, highly resolved body-inclusive simulations have been successfully used to analyze key features of a towed wake. However, due to the drawbacks discussed, there is need for a tool which can simulate as effectively but with less computational expense than a body-inclusive simulation. Detailed herein is a hybrid spatially-evolving model which addresses the

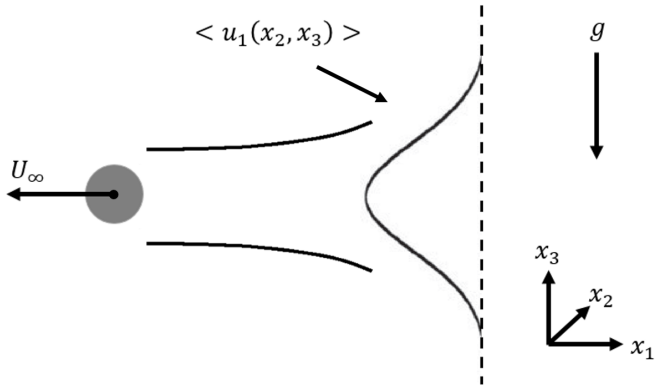

Figure 4.1: Illustration of a towed wake in a Cartesian frame of reference with a corresponding mean streamwise velocity profile ($\langle u_1(x_2,x_3)\rangle$) and gravity ($g$) acting in the negative x_3 direction.

limitations of body-inclusive models while still satisfactorily capturing key flow features. It should be emphasized that this hybrid investigation remains a spatial development study and thus cannot necessarily compete with temporally-evolving models which are able to extend far downstream of the body. The presented work extends to a downstream distance of approximately ninety body diameters with comparisons given for nearly fifty body diameters. Temporally-evolving simulations have provided results much farther downstream to distances of $O(1000D)$. The proposed model is, however, a computationally less intensive tool than has previously been used in spatial development studies and allows for analysis farther from the body, though perhaps still not as far as in certain temporal investigations. The current study is a validation of the hybrid method which lays the groundwork for utilization of the model in future work.

4.0.15 Formulation

4.0.15.1 Hybrid model

The hybrid model utilized in this work addresses the computational limitations of both temporally-evolving and spatially-evolving body-inclusive simulations. In this model, cross-sectional data planes are extracted from a spatially-evolving body-inclusive simulation at some point downstream of the body and over a time interval that starts after the flow has achieved

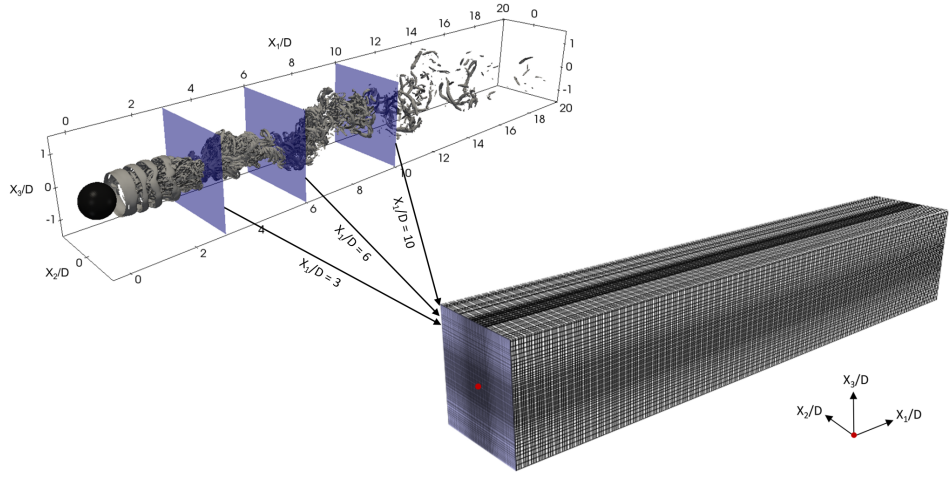

Figure 4.2: Illustration of the setup for the hybrid simulation showing a three-dimensional view of the body-inclusive domain and planes at $x_1/D = 3$, $x_1/D = 6$, and $x_1/D = 10$ indicating the different starting point choices for the hybrid model simulation domain. The Cartesian grid and corresponding coordinate reference frame are noted.

statistical steady-state. Data at a chosen downstream location are used as inlet conditions in a spatially-evolving simulation without a body which has a coarser grid than that of the body-inclusive simulation. The body-inclusive simulations from which inlet planes were extracted for the purposes of this work are documented extensively by Pal *et al.* (2017). A spatially-evolving approximation of the flow is used, whereby streamwise evolution of statistics may be examined. Figure 4.2 illustrates the setup for the hybrid model simulation.

It is first necessary to choose a location at which to extract data in the body-inclusive simulation. In order to investigate the flow sensitivity to extraction location, three locations downstream of the body were analyzed, $x_1/D = 3$, 6, and 10. Figure 4.2 depicts these locations with reference to the body in an unstratified body-inclusive simulation. Note the location of $x_1/D = 3$ is at the tail end of the recirculation region. These locations are chosen to include the near wake dynamics captured by the body-inclusive simulation. However, the richer spectrum of turbulence in this region demands higher computational cost and sufficiently refined grid resolution. Data planes are extracted over a specified time interval during which the body-inclusive flow is deemed to be at steady state. Time steps, Δt, in the body-inclusive simulation are determined by a *Courant-Friedrichs-Lewy (CFL)* condition resulting in a variable Δt between 0.0002 and 0.0009. Planes

are extracted every one hundred time steps in the body-inclusive simulation thus corresponding to $0.02 \leq \Delta t \leq 0.09$ between inlet planes in the hybrid model simulation. This choice of a coarser (relative to the body-inclusive simulation) time step in the hybrid simulation is sufficient to resolve the dynamics downstream of the inlet plane as will be demonstrated. Inlet planes are interpolated to a coarser grid as described in the subsequent section and fed as inflow in a spatially-evolving simulation with far less computational cost than a comparable body-inclusive simulation.

4.0.15.2 Governing equations

For an unsteady, incompressible flow subject to the Boussinesq approximation in which density variations are considered only where they give rise to gravitational force, the nondimensional conservation equations for mass, momentum, and density are taken in a Cartesian coordinate frame as follows:

$$\frac{\partial u_k}{\partial x_k} = 0, \tag{4.1a}$$

$$\frac{\partial u_i}{\partial t} + \frac{\partial (u_k u_i)}{\partial x_k} = -\frac{\partial p}{\partial x_i} + \frac{1}{Re}\frac{\partial^2 u_i}{\partial x_k \partial x_k} - \frac{1}{Fr^2}\tilde{\rho}\,\delta_{i3}, \tag{4.1b}$$

$$\frac{\partial \rho}{\partial t} + \frac{\partial (u_k \rho)}{\partial x_k} = \frac{1}{RePr}\frac{\partial^2 \rho}{\partial x_k \partial x_k} \tag{4.1c}$$

In the above equations, $x_k = (x_1, x_2, x_3)$ represent the streamwise, spanwise, and vertical directions, respectively. Density is decomposed into a constant reference density, mean, and fluctuating components respectively designated as follows where an $*$ indicates a dimensional value,

$$\rho^* = \rho_0 + \bar{\rho}^*(x_3, t) + \tilde{\rho}^*(x_i, t)\,. \tag{4.2}$$

The equations were nondimensionalized using the following characteristic scales:

$$t = t^* U_\infty / D, \quad x_i = {x_i}^* / D, \quad u_i = {u_i}^* / U_\infty,$$
$$\rho = \rho^* / \rho_0, \quad \tilde{\rho} = \tilde{\rho}^* / (DC^*), \quad p = \tilde{p}^* / (\rho_0 {U_\infty}^2). \tag{4.3}$$

Here, $C^* = |d\bar{\rho}^*/d{x_3}^*|(t=0)$ is the dimensional density gradient. The nondimensional parameters Reynolds number (Re), Froude number (Fr), and Prandtl number (Pr) are given by

$$Re = U_\infty D/\nu, \qquad Fr = U_\infty/(N^* D), \qquad Pr = \nu/\kappa. \tag{4.4}$$

Here, U_∞ is the characteristic body velocity, D is the characteristic sphere diameter, ν is the kinematic viscosity, and κ is the thermal diffusivity. The buoyancy frequency is given by $N^* = [-gC^*/\rho_0]^{1/2}$. $Pr = 1$ for all simulations.

4.0.15.3 Numerical method

The governing equations given in equation 4.1 are solved using direct numerical simulation on a staggered grid, where pressure and density are stored at the cell centers and velocities are stored at the cell edges. It should be noted that after the simulation during post-processing and the calculation of statistics, all variables are interpolated to the cell center.

Discretization of spatial derivatives is performed with a second-order, central finite difference scheme. Time is advanced explicitly using the Williamson (1980) low-storage Runge Kutta method. Convergence of the Poisson pressure equation used to project velocity into divergence-free space is accelerated via a parallel multi-grid solver which employs Red-Black Gauss-Seidel (RBPGS) smoothing. During coarsening, an increasing number of relaxation sweeps accelerates convergence. Detailed information concerning the spatial discretization, time integration, and multi-grid solver can be found in the work by Brucker (2009).

A sponge region of thickness equivalent to 1.2 body diameters in the body-inclusive simulations is utilized in the form of a Rayleigh damping function at the spanwise and vertical boundaries

to prevent reflections of internal gravity waves (Brucker & Sarkar (2010)). Velocities and densities are gradually dampened using the damping terms

$$-\phi(x_i)[u_i(x_i,t)-U_{i,\infty}] \quad , \quad -\phi(x_i)[\rho(x_i,t)-\rho_\infty(x_3)] \tag{4.5}$$

which are added to the momentum and density equations given respectively in 4.1. Here, $\phi(x_i)$ behaves quadratically over the specified region, free-stream velocity is given by $U_{i,\infty}=[1,0,0]$, and $\rho_\infty(x_3)=-\rho_0 C^* x_3/D$. This sponge region does not affect the flow given its distance from the wake. This damping function relaxes all variables in the interior of the domain to their value at the boundary. Brucker (2009) also provides a detailed description of this sponge implementation.

The codes used in this work are parallelized over multiple nodes which communicate using MPI libraries. A domain decomposition method divides the domain into blocks, assigns each block ghost cells for padding, and distributes the blocks to specific nodes. Simulations are carried out using supercomputers managed by the Department of Defense High Performance Computing Modernization Program (DoD HPCMP).

Density gradients corresponding to a specific Froude number are used to initialize the background density field in the domain. The density and velocities at $t=0$ in the hybrid spatially-evolving simulation are prescribed as follows. The first realization of ρ, u_1, u_2, and u_3 from the extracted inlet plane time series is imposed at the $x_1=0$ plane. The field variables at all subsequent downstream planes are taken to be equal to those at $x_1=0$ so that, at $t=0$, there are no streamwise (x_1) gradients in ρ, u_1, u_2, or u_3. The time series of instantaneous density fluctuations and three instantaneous velocity components (u_1, u_2, and u_3) extracted from the body-inclusive simulations are then fed into the domain at the inlet.

Neumann boundary conditions are enforced for the velocity components and density at the spanwise and vertical boundaries. Pressure is assigned a Dirichlet boundary condition. In the streamwise direction, pressure is subject to a Dirichlet condition at the inflow and a Neumann boundary condition at the outflow. Inflow-outflow boundary conditions are employed for the velocity

components and density in the streamwise direction where the inflow is read from an inlet data file and outflow is treated using a second-order extrapolation boundary condition with numerical error of $O(\Delta x_1^2)$. A summary follows in table 4.1.

Table 4.1: Boundary conditions. L_1, L_2, and L_3 are the domain lengths in the streamwise (x_1), spanwise (x_2), and vertical (x_3) directions, respectively. The subscript m given in the outflow conditions represents the coordinate index in the streamwise (x_1) direction while the subscript n indicates time level.

Boundary Location	Velocity, u_i	Pressure, p	Density, ρ
$x_1 = 0$	read	$p = 0$	read
$x_1 = L_1$	$u^n_{i,m+1} = 2u^n_{i,m} - u^n_{i,m-1}$	$\partial p/\partial x_1 = 0$	$\rho^n_{i,m+1} = 2\rho^n_{i,m} - \rho^n_{i,m-1}$
$x_2 = \pm L_2/2$	$\partial u_i/\partial x_2 = 0$	$p = 0$	$\partial \rho/\partial x_2 = 0$
$x_3 = \pm L_3/2$	$\partial u_i/\partial x_3 = 0$	$p = 0$	$\partial \rho/\partial x_3 = -\rho_0 C^*/D$

As time steps used in the hybrid model are given by the time lapse between every one hundred time steps of the body-inclusive simulation, adherence to the *CFL* condition limits the grid spacing of the hybrid model. Grid spacing cannot be arbitrarily small without violating the *CFL* condition. Thus, when using grids with finer resolution, the time steps must also be altered (either by saving data more frequently from the body-inclusive simulation or interpolation in time) to accommodate the reduction in grid spacing.

Statistics are calculated via time-averaging over a nondimensional time $t \approx 80$. This time interval is the exact interval used by the body-inclusive simulations documented by Pal *et al.* (2017) for calculations, occurring after the flow had reached statistical steady-state. The fully three-dimensional statistics are decomposed into mean and fluctuating components using Reynolds decomposition given by

$$u_i = \langle u_i \rangle + u_i^{'}, \qquad \rho = \langle \rho \rangle + \rho^{'}, \qquad p = \langle p \rangle + p^{'} \tag{4.6}$$

where a $\langle\rangle$ denotes a mean quantity.

4.0.15.4 Simulation parameters

A total of nine hybrid model simulations are presented for $Fr = \infty$, 3, and 1. Each Fr case was simulated three times with differing inlet extraction locations, $x_1/D = 3$, $x_1/D = 6$, and $x_1/D = 10$. The naming convention for the cases is the Froude number followed by the extraction location, e.g. Fix3, Fix6, and Fix10 represent the $Fr = \infty$ cases with extraction locations, $x_1/D = 3$, 6, and 10, respectively. The original body-inclusive simulations are denoted FiBI, F3BI, and F1BI for $Fr = \infty$, 3, and 1, respectively. For all cases, the hybrid model simulation uses a Cartesian grid with streamwise (x_1), spanwise (x_2), and vertical (x_3) directions. However, the body-inclusive simulations were performed using a cylindrical computational domain given by the radial (r), azimuthal (θ), and streamwise (z) directions. As the originally extracted data planes are on a cylindrical grid, coordinate mapping using a cubic spline interpolation scheme is used to map the data from cylindrical to Cartesian coordinates.

Tables 4.2 and 4.3 detail the parameters for the hybrid model simulations and body-inclusive simulations, respectively. The Reynolds number, Froude number, number of grid points, domain sizes, and minimum grid spacing in each direction are specified. More specific information concerning the body-inclusive simulations can be found by referring to Pal *et al.* (2017). For the hybrid model simulations, the streamwise grid distribution is uniform while the spanwise and vertical grids are stretched at 1.6% outside of the uniformly-stretched regions $-2.0 < x_2/D < 2.0$ and $-2.0 < x_3/D < 2.0$. In the stretched regions, this indicates a ratio of 1.016 between a stretched grid cell and its smaller neighboring cell. Grid spacing in the streamwise direction is $\Delta x_1 = 0.06$ while the minimum grid spacing in the spanwise and vertical directions is $\min(\Delta x_2) = \min(\Delta x_3) = 0.04$. The minimum streamwise grid spacing is approximately forty times larger than the body-inclusive simulation minimum streamwise grid spacing of $\min(\Delta z) = 0.0016$. It should be noted that the grid spacing in the body-inclusive simulations is smallest close to the sphere where higher resolution is required to resolve the boundary layer. This grid size increases with downstream distance. Take for instance the extraction location of $x_1/D = 6$ where the grid spacing in the body-inclusive simulations is $\Delta z = 0.0121$. This is approximately five times smaller than the grid cell size of the

hybrid model simulations at the same location. Note that the final number of grid points required in the body-inclusive simulations is approximately 400×10^6 grid points while the hybrid simulations use around 100×10^6 grid points.

An investigation of flow physics farther downstream than previously studied using spatially-evolving simulations is planned but is not the focus of this work. Validation is performed to approximately eighty body diameters downstream based solely on the downstream distance of the body-inclusive simulations used for direct comparison. Given the end of the near wake regime at $Nt \approx 2$ and the start of the quasi-two-dimensional regime at $Nt \approx 50$, the current simulations seek only to validate the use of the hybrid model for study of the intermediate wake and the so-called nonequilibrium regime in stratified wakes.

Table 4.2: Hybrid simulation parameters. The subscript x_1 refers to the streamwise direction while x_2 and x_3 refer to the spanwise and vertical directions, respectively. The Reynolds number (Re), Froude number (Fr), number of grid points ($N_{x_1}, N_{x_2}, N_{x_3}$), domain lengths ($L_{x_1}, L_{x_2}, L_{x_3}$), and minimum grid spacing ($\min(\Delta x_1), \min(\Delta x_2), \min(\Delta x_3)$) in all directions are given for each case. The total number of grid points, N is also given where $N = N_{x_1} \times N_{x_2} \times N_{x_3}$.

Case	Re	Fr	N_{x_1}	N_{x_2}, N_{x_3}	L_{x_1}	L_{x_2}, L_{x_3}	$\min(\Delta x_1)$	$\min(\Delta x_{2,3})$	N
Fix3, Fix6, Fix10	3700	∞	1536	256	92.2	15.6	0.06	0.04	$\approx 101 \times 10^6$
F3x3, F3x6, F3x10	3700	3	1536	256	92.2	15.6	0.06	0.04	$\approx 101 \times 10^6$
F1x3, F1x6, F1x10	3700	1	1536	256	92.2	15.6	0.06	0.04	$\approx 101 \times 10^6$

Table 4.3: Body-inclusive simulation parameters. The subscript z refers to the streamwise direction while r and θ refer to the radial and azimuthal directions, respectively. The Reynolds number (Re), Froude number (Fr), number of grid points (N_r, N_θ, N_z), domain lengths (L_r, L_θ, L_z), and minimum grid spacing ($\min(\Delta r), \min(r\Delta\theta), \min(\Delta z)$) in all directions are given for each case. The total number of grid points, N is also given where $N = N_r \times N_\theta \times N_z$.

Case	Re	Fr	N_r	N_θ	N_z	L_r	L_θ	L_z	$\min(\Delta r)$	$\min(r\Delta\theta)$	$\min(\Delta z)$	N
FiBI	3700	∞	630	128	4608	16.3	2π	93.9	0.0016	4×10^{-5}	0.0016	$\approx 372 \times 10^6$
F3BI	3700	3	690	128	4608	59.8	2π	93.9	0.0016	4×10^{-5}	0.0016	$\approx 407 \times 10^6$
F1BI	3700	1	690	128	4608	59.8	2π	105.9	0.0016	4×10^{-5}	0.0016	$\approx 407 \times 10^6$

As previously mentioned, inlet planes are extracted every one hundred time steps of the body-inclusive simulation. The time steps of the body-inclusive simulations are quite small so as not to violate the *CFL* condition. A range of time steps and estimated *CFL* numbers are given in

table 4.4. Note that the *CFL* ranges are locally calculated at a downstream distance of $z/D = 6$ in the body-inclusive simulations and at the inlet of the hybrid model simulations with extraction location $x_1/D = 6$. The given *CFL* numbers are estimated using a representative average of the velocity field (free-stream velocity, U_∞) and streamwise grid spacing by

$$CFL = \frac{U_\infty \Delta t}{\Delta z} \quad , \quad CFL = \frac{U_\infty \Delta t}{\Delta x_1} \tag{4.7}$$

for the the body-inclusive simulations and hybrid model simulations, respectively.

The decrease in the total number of grid points, coarser minimum grid cell size, and increase in time step owing to extraction at every one hundred of the original time steps results in a computational run time measurable in hours as opposed to weeks. For instance, the $Fr = 3$ body-inclusive simulation required approximately 256,000 CPU hours while the corresponding hybrid simulations required only 1,400 CPU hours.

Table 4.4: Time step and *CFL* ranges for the hybrid model simulations extracted at $x_1/D = 6$ and the body-inclusive simulations. Note the time steps between the hybrid model simulations and body-inclusive simulations differ by a factor of one hundred as data planes were extracted every one hundred time steps. The range of *CFL* numbers for the body-inclusive cases is calculated locally using Δz at $z/D = 6$.

Case	Δt	CFL
Fix6	$0.029 \leq \Delta t \leq 0.083$	$0.49 \leq CFL \leq 1.39$
F3x6	$0.026 \leq \Delta t \leq 0.084$	$0.44 \leq CFL \leq 1.40$
F1x6	$0.032 \leq \Delta t \leq 0.087$	$0.54 \leq CFL \leq 1.44$
FiBI	$0.00029 \leq \Delta t \leq 0.00083$	$0.02 \leq CFL \leq 0.07$
F3BI	$0.00026 \leq \Delta t \leq 0.00084$	$0.02 \leq CFL \leq 0.07$
F1BI	$0.00032 \leq \Delta t \leq 0.00087$	$0.03 \leq CFL \leq 0.07$

4.0.16 Extraction location

As mentioned, the sensitivity of extraction location is explored using three streamwise points, $x_1/D = 3$, 6, and 10. Figures 4.3a - 4.3c show the evolution of streamwise mean defect velocity (U_D)

where $U_D = U_\infty - \langle u_1 \rangle$ at the centerline where $x_2/D = x_3/D = 0$ for $Fr = \infty, 3$, and 1, respectively. While the monotonic decay trend expected for $Fr = \infty$ is captured, there is some deviation from the body-inclusive simulation at all extraction locations. This is attributed to differences in the grid resolution: first, the streamwise grid used in the hybrid model is approximately five times coarser than the body-inclusive simulation as seen from the minimum grid spacing parameters in tables 4.2 and 4.3 and, second, the cylindrical grid of the body-inclusive simulation leads to an azimuthal grid spacing which becomes progressively larger with radial distance. The smallest scales of turbulent motion increase in size with downstream distance from the body and it is clear in figures 4.3a - 4.3c that while extraction at $x_1/D = 3$ is the least successful case, agreement between the body-inclusive and hybrid simulations improves as the extraction location is moved farther downstream. In the $Fr = 3$ cases of figure 4.3b, the first minimum is achieved at a streamwise location corresponding to half of the buoyancy period, $x_1/D = \pi Fr$, also noted by Chongsiripinyo & Sarkar (2017). Figure 4.3c shows the "oscillatory modulation" indicative of a steady body-generated lee wave as identified by Pal *et al.* (2017) and Chongsiripinyo & Sarkar (2017). These modulations are magnified in figure 4.4 to clearly show successive minima and maxima, and a wavelength which is consistent with the body-inclusive simulation. Figure 4.4a shows the intermediate wake until a downstream distance of $x_1/D = 40$ while figure 4.4b extends into the far wake until a downstream distance of $x_1/D \approx 70$. While the amplitude of oscillatory modulations differs slightly from the body-inclusive simulation, the discrepancy gradually improves until $x_1/D \approx 35$ where the amplitude is almost identical to the body-inclusive simulation for the cases of extraction at $x_1/D = 6$ and $x_1/D = 10$. Only in the strongly stratified $Fr = 1$ cases are differences between extraction at $x_1/D = 6$ and $x_1/D = 10$ notable and these differences become minor farther from the body. Even the extraction location of $x_1/D = 3$ appears to improve in amplitude farther downstream although it remains the case of least agreement with the body-inclusive simulations.

From these results, it is concluded that the extraction location $x_1/D = 3$ is too close to the body to accurately capture flow physics. Here, at the tail end of the recirculation region, the bell-shaped mean wake signature is not completely formed because of the presence of transient

(a)

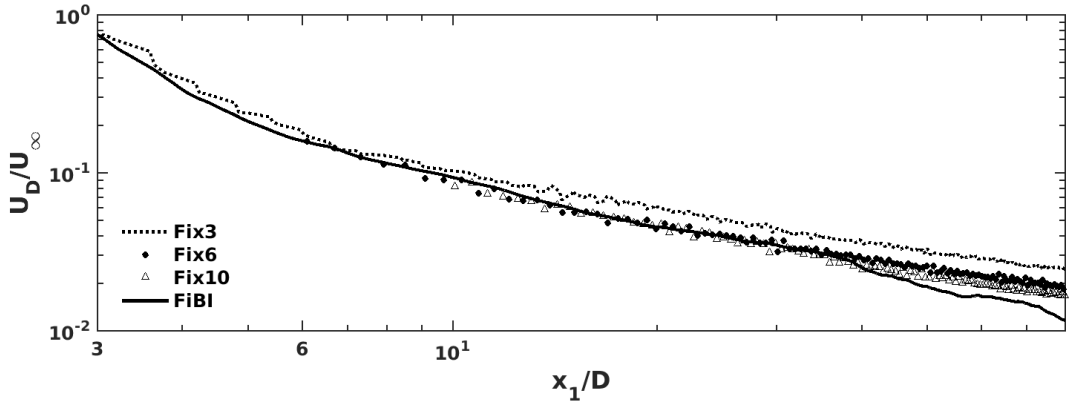

(b)

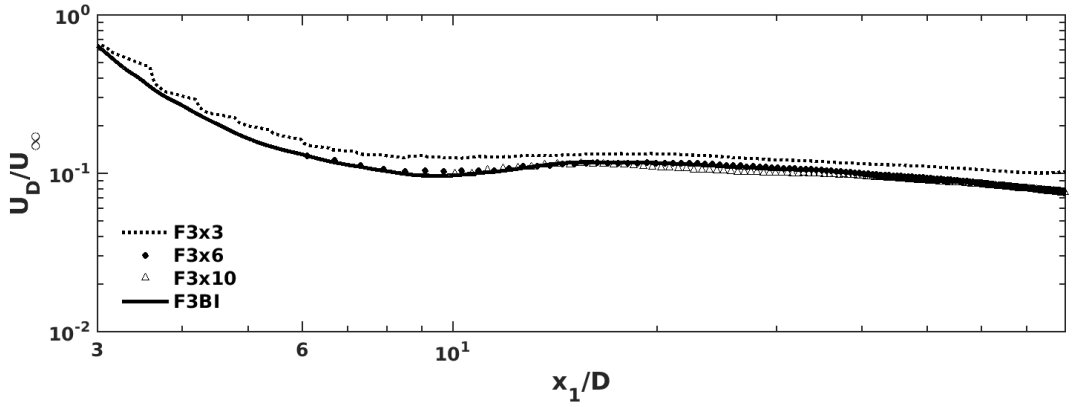

(c)

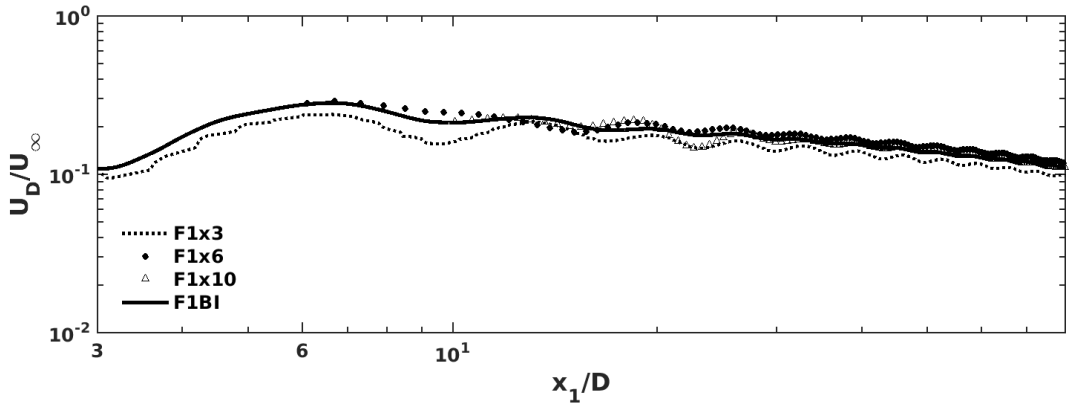

Figure 4.3: Streamwise normalized mean defect velocity (U_D/U_∞) at the centerline: (a) $Fr = \infty$, (b) $Fr = 3$, and (c) $Fr = 1$.

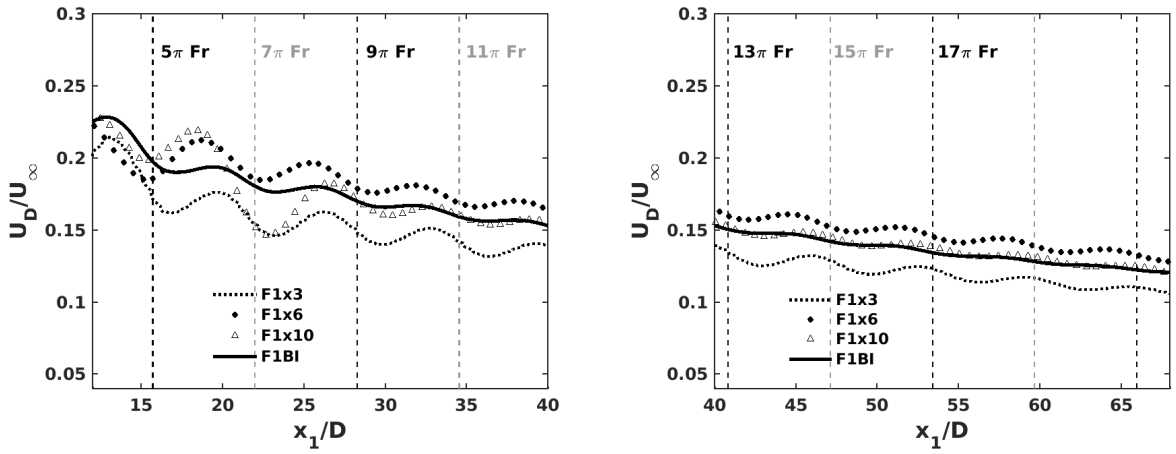

(a) (b)

Figure 4.4: A zoomed view of the streamwise mean defect velocity shows oscillatory modulation induced by the steady lee waves: (a) Near the body, (b) Farther downstream.

regions of reverse flow towards the sphere. However, $x_1/D = 6$ and $x_1/D = 10$ are found to be effective extraction locations which capture much of the flow physics. For the remainder of this work, $x_1/D = 6$ is chosen for further analysis as this choice requires a shorter and, therefore, less expensive body-inclusive domain for obtaining the inflow of the hybrid simulation.

4.0.17 Flow visualization

Instantaneous vorticity comparisons between the body-inclusive and hybrid model simulations at nondimensional time, $t = 125$, are given for the stratified cases in figures 4.5 and 4.6 using vertical ($x_1 - x_3$) and horizontal ($x_1 - x_2$) plane cuts for the azimuthal/lateral and vertical vorticity components, respectively. Overall, the figures indicate good qualitative agreement between the hybrid model and body-inclusive simulations. However, it is clear that more small-scale motions are captured in the body-inclusive simulations owing to the much finer grid resolution.

For $Fr = 3$, the visualization of azimuthal/lateral vorticity in figure 4.5a confirms capture of the layered structure indicative of fluctuation decay observed in the body-inclusive simulations. Faint phase lines resulting from the propagation of internal waves to the background are also evident. Large-scale vortex shedding is clearly captured by the hybrid model as evidenced by the wake

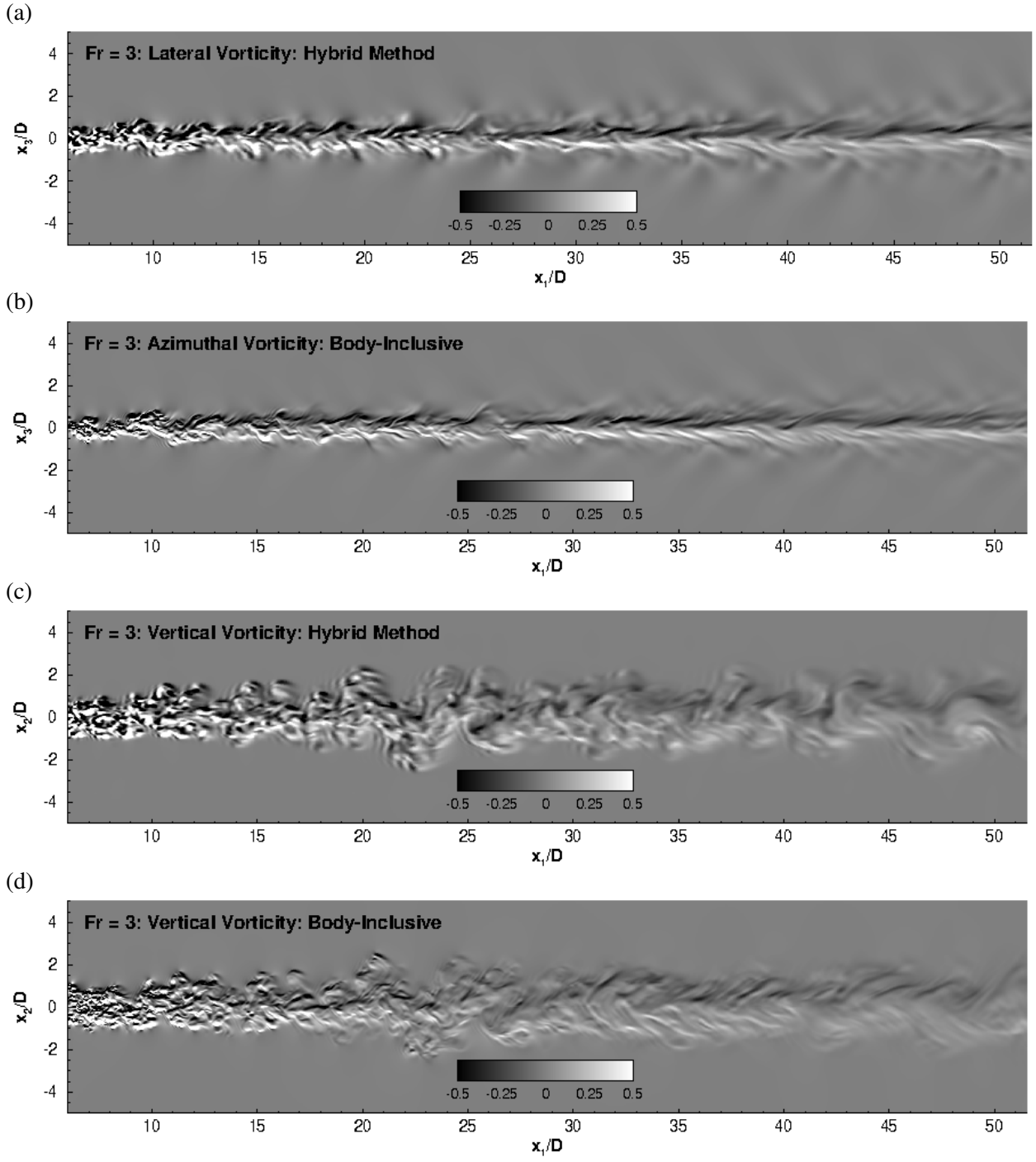

Figure 4.5: Azimuthal/lateral and vertical vorticity visualizations at nondimensional $t = 125$ shown on $x_1 - x_3$ and $x_1 - x_2$ plane cuts, respectively, for the hybrid model simulations (4.5a and 4.5c) and the body-inclusive simulations (4.5b and 4.5d) for $Fr = 3$ and extraction location, $x_1/D = 6$.

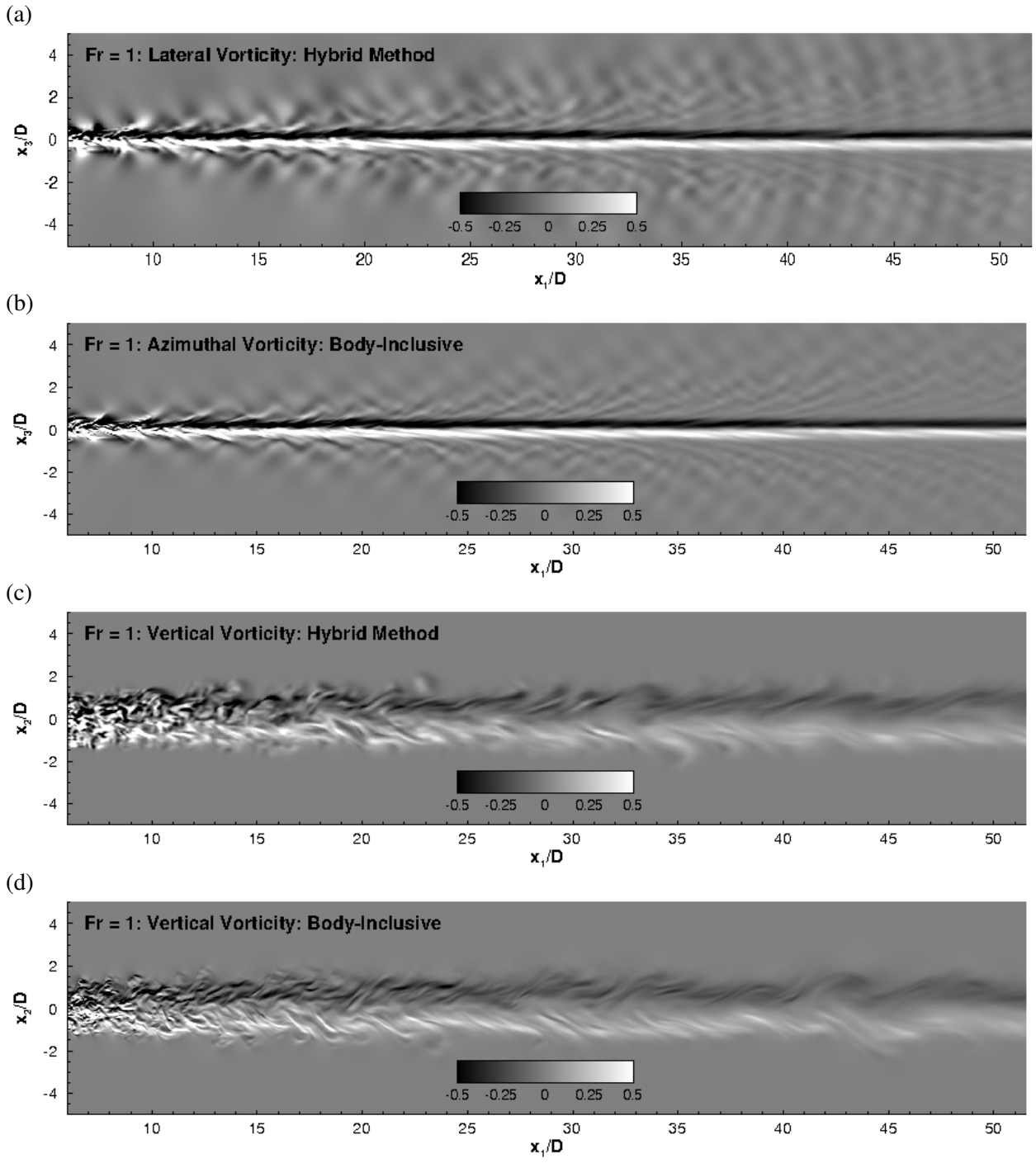

Figure 4.6: Azimuthal/lateral and vertical vorticity visualizations at nondimensional $t = 125$ shown on $x_1 - x_3$ and $x_1 - x_2$ plane cuts, respectively, for the hybrid model simulations (4.6a and 4.6c) and the body-inclusive simulations (4.6b and 4.6d) for $Fr = 1$ and extraction location, $x_1/D = 6$.

structure and downstream formation of coherent vortical structures in figure 4.5c. In figure 4.6, similar behavior is noted for $Fr = 1$. The layered structure is even more pronounced in figures 4.6a and 4.6c than in the corresponding $Fr = 3$ visuals. Additionally, the internal wave propagation angle observed in the hybrid model simulations agrees with the body-inclusive simulations.

4.0.18 Turbulence

Turbulence representation by the hybrid model is analyzed by means of *r.m.s.* velocities, area-integrated *t.k.e.*, and *t.k.e.* budget terms. Beginning with the *r.m.s.* velocities shown in figure 4.7, decay trends are consistent with the body-inclusive simulations with only minor deviations for most Fr. Oscillatory modulations in the vertical *r.m.s.* velocity profiles have a frequency that increases with background buoyancy frequency (N) as seen in figure 4.7c. The most notable deviation is found in the $u_{3,rms}$ profile for $Fr = 1$ which captures the wavelength of the oscillatory behavior seen in the body-inclusive simulations but underpredicts magnitude. While phasing is consistent, the amplitude of the oscillatory modulations differs in the region $x_1/D > 30$. For stratified cases where $x_1/D > 30$, horizontal motions dominate as shown by the magnitude of the $u_{1,rms}$ and $u_{2,rms}$ plots versus that of $u_{3,rms}$. The differences in $u_{3,rms}$ for the $Fr = 1$ case are not minor but as the *r.m.s* velocity is nearly an order of magnitude smaller than the $u_{1,rms}$ and $u_{2,rms}$ plots, these differences are acceptable. Figure 4.7 serves to emphasize that the influence of changing Fr is captured for less computational cost than performing the corresponding body-inclusive simulations.

The evolution of *t.k.e.* in the streamwise direction is given by area-integration of the $x_2 - x_3$ plane in figure 4.7d with *t.k.e.* (K) given by $K = \frac{1}{2}\langle u_i^{'} u_i^{'} \rangle$. Decay trends are captured for all Fr although in the region $x_1/D > 30$, the hybrid method results begin to decay more quickly than the body-inclusive cases for $Fr = \infty$ and $Fr = 3$. As with the *r.m.s* velocities, the effect of varying Fr on *t.k.e* is captured for less computational cost than performing the corresponding body-inclusive simulations.

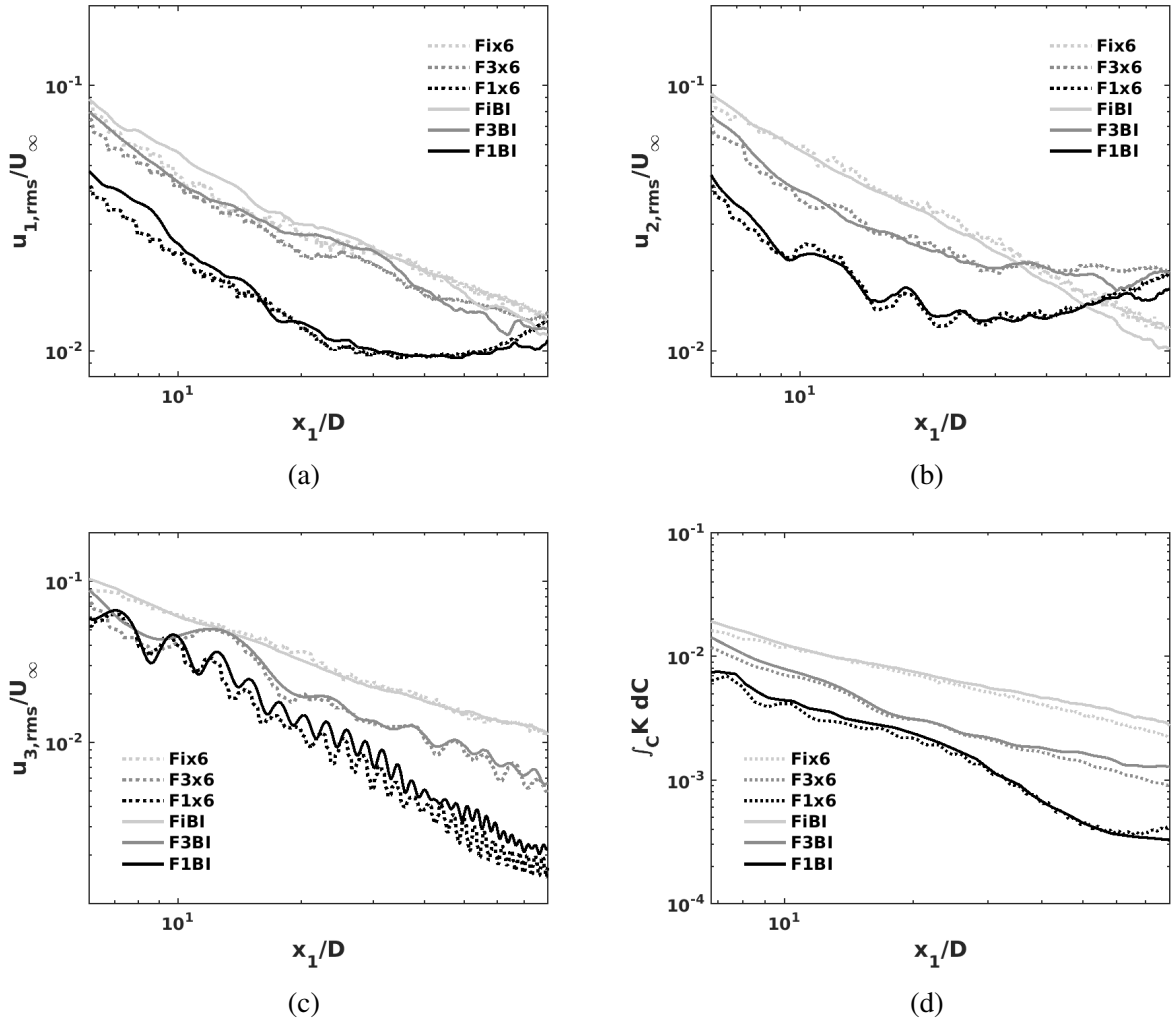

Figure 4.7: Evolution of centerline turbulence statistics: (a) streamwise velocity ($u_{1,rms}$), (b) spanwise velocity ($u_{2,rms}$), (c) vertical velocity ($u_{3,rms}$), and (d) area-integrated *t.k.e.*. Body-inclusive and hybrid simulations are compared for $Fr = \infty$, $Fr = 3$, and $Fr = 1$.

The *t.k.e.* budget in the Cartesian coordinate system used for this analysis is given by

$$\frac{\partial K}{\partial t} = P - \varepsilon + B - A - \frac{\partial T_i^{'}}{\partial x_i} \tag{4.8}$$

with production (P), dissipation (ε), buoyancy flux (B), advection (A), and transport term ($T_i^{'}$) specified as follows.

$$\begin{gathered} P = -\langle u_i^{'} u_j^{'} \rangle \frac{\partial \langle u_i \rangle}{\partial x_j}, \quad \varepsilon = 2\nu \langle s_{ij}^{'} s_{ij}^{'} \rangle, \quad s_{ij}^{'} = \tfrac{1}{2}\left(\frac{\partial u_i^{'}}{\partial x_j} + \frac{\partial u_j^{'}}{\partial x_i}\right), \\ B = -\frac{g}{\rho_0} \langle \tilde{\rho}^{'} u_3^{'} \rangle, \quad A = \langle u_j \rangle \frac{\partial K}{\partial x_j}, \\ T_i^{'} = \tfrac{1}{2} \langle u_i^{'} u_j^{'} u_j^{'} \rangle + \frac{1}{\rho_0} \langle u_i^{'} p^{'} \rangle - 2\nu \langle u_j^{'} s_{ij}^{'} \rangle \end{gathered} \tag{4.9}$$

Figures 4.8, 4.9, and 4.10 compare the *t.k.e.* budget terms, integrated over a $x_2 - x_3$ cross-section, from the hybrid model and body-inclusive simulations. There are discrepancies in some of these terms, e.g. turbulent dissipation in the intermediate wake, $x_1/D < 20$, as shown in figure 4.8. The majority of budget-term inconsistencies is attributed to the coarseness of the grid in comparison to that of the body-inclusive simulations. To support this assertion, three additional simulations were performed using a grid with higher resolution than the previous hybrid simulations. Inlet planes for these cases were generated via linear interpolation in time of the coarser grid data planes. Using Cases Fix6, F3x6, and F1x6 as benchmarks, the grid resolution is doubled in the spanwise (x_2) and vertical (x_3) directions and tripled in the streamwise (x_1) direction. This results in grid spacing of $\Delta x_1 = 0.02$ in the streamwise direction and minimum grid spacing of $\min(\Delta x_2) = \min(\Delta x_3) = 0.02$ in the spanwise and vertical directions. The new simulations are referred to as cases Fix6HR, F3x6HR, and F1x6HR corresponding to the $Fr = \infty$, 3, and 1 higher resolution cases, respectively. For these cases, the number of grid points in the streamwise (x_1), spanwise (x_2), and vertical (x_3) directions are $N_{x_1} = 2560$, $N_{x_2} = 512$, and $N_{x_3} = 512$, respectively. The domain lengths in the streamwise, spanwise, and vertical directions are $L_{x_1} = 51.2$, $L_{x_2} = 15.5$, and $L_{x_3} = 15.5$, respectively. The streamwise grid distribution is uniform while the spanwise and

(a)

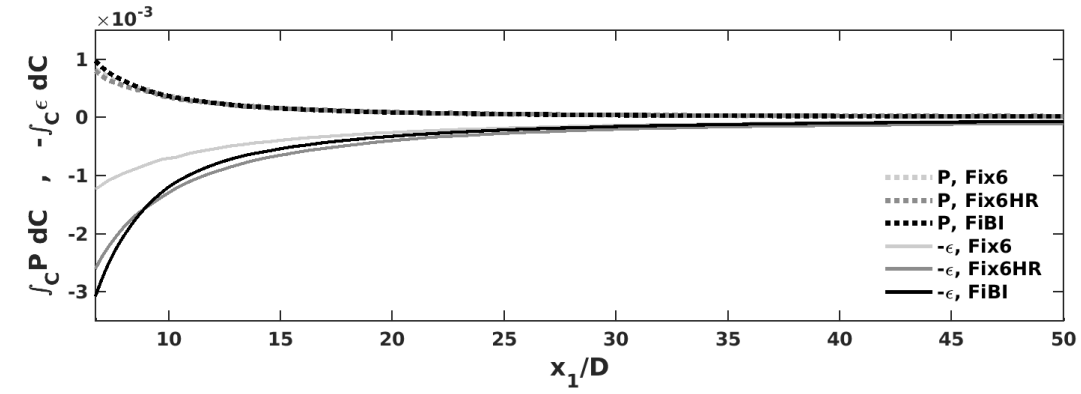

(b)

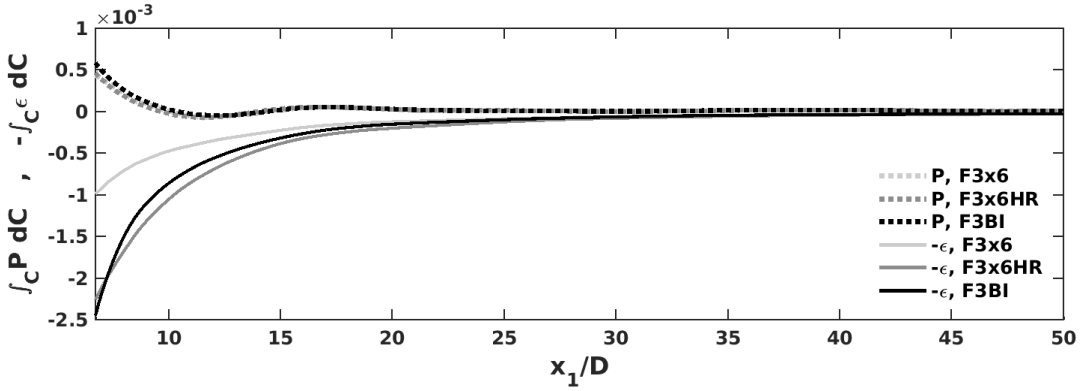

(c)

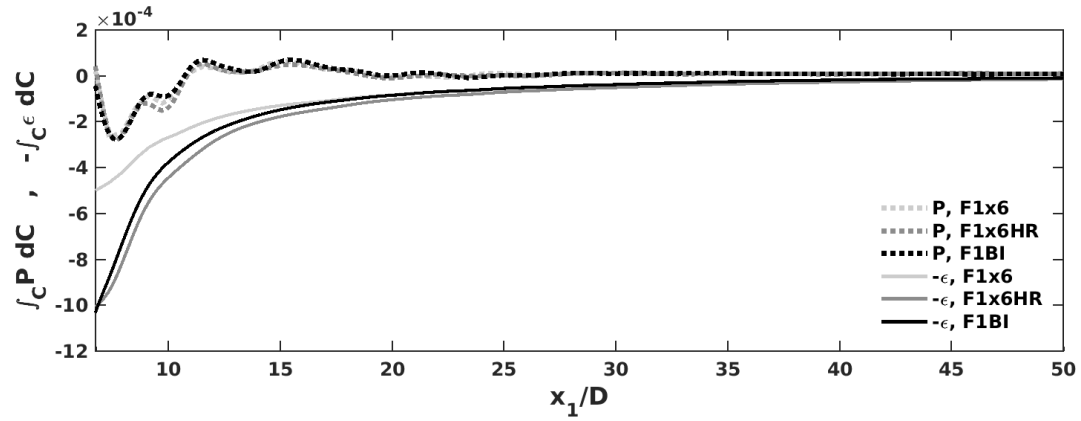

Figure 4.8: Area-integrated production (P) and dissipation (ε) evolution in the streamwise direction: (a) $Fr = \infty$, (b) $Fr = 3$, and (c) $Fr = 1$.

(a)

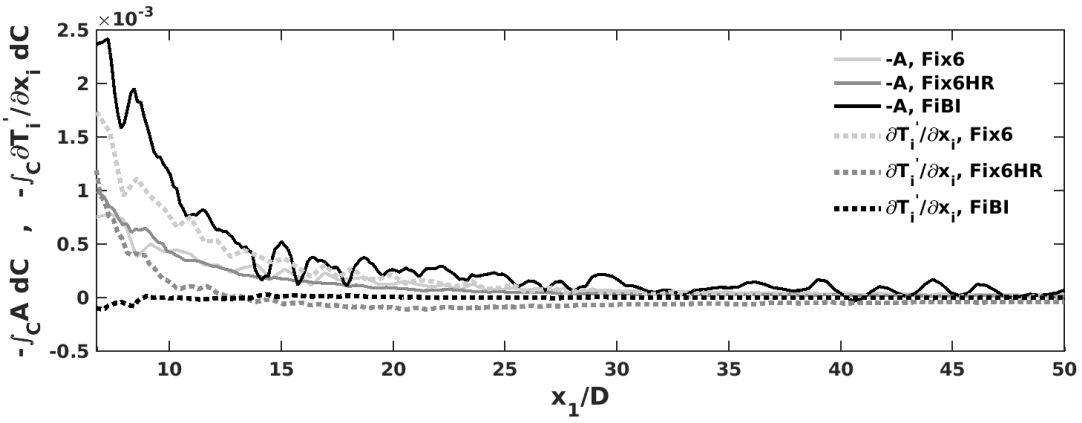

(b)

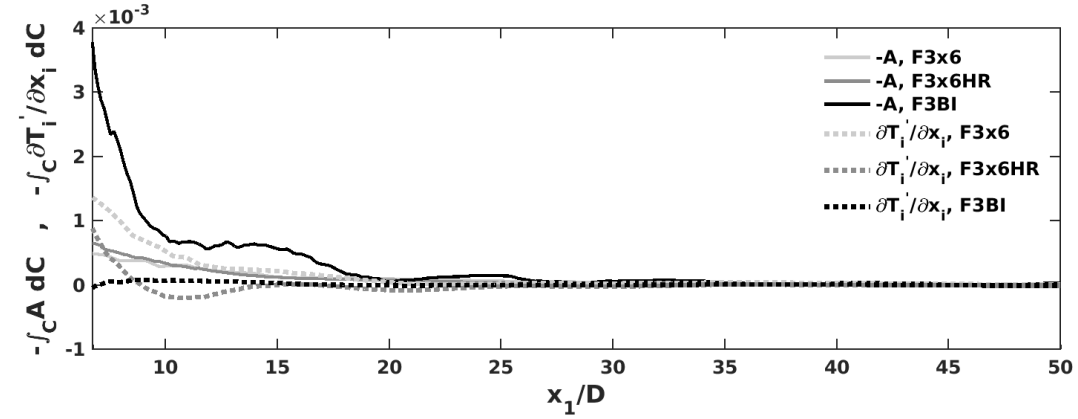

(c)

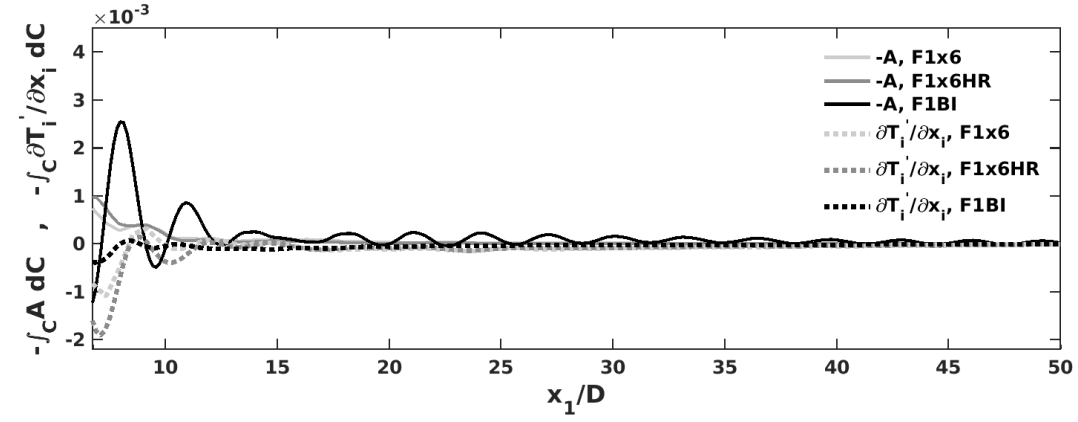

Figure 4.9: Area-integrated advection (A) and transport ($\partial T_i^{'}/\partial x_i$) evolution in the streamwise direction: (a) $Fr = \infty$, (b) $Fr = 3$, and (c) $Fr = 1$.

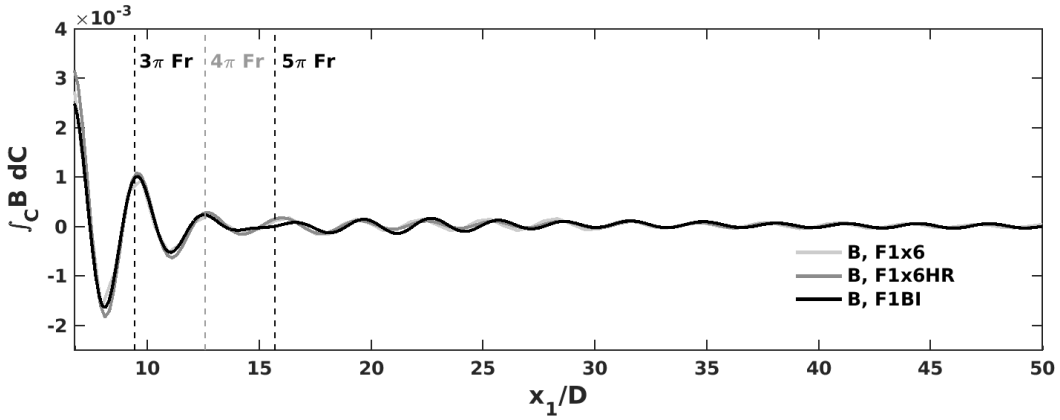

Figure 4.10: Area-integrated buoyancy flux (B) evolution in the streamwise direction for $Fr = 1$.

vertical grids are stretched at 0.75% outside of the uniformly-stretched regions $-2.0 < x_2/D < 2.0$ and $-2.0 < x_3/D < 2.0$. In the stretched regions, this indicates a ratio of 1.0075 between a stretched grid cell and its smaller neighboring cell.

When compared to the corresponding cases with coarser grid resolution, it is clear that the higher resolution cases better capture turbulence, particularly in the region $x_1/D < 15.0$ as seen in figures 4.8 and 4.9. As seen in figure 4.8, the production (P) is well-captured regardless of the grid resolution for all Fr. However, the dissipation (ε) is clearly better captured with the higher resolution cases. In the coarser grid cases for all Fr, there is a notable underestimation in dissipation near the domain inlet which is corrected with grid refinement. Production is characterized by low frequency modes which are well-captured in the coarse and fine grids. In contrast, small-scale structures and higher frequency modes responsible for dissipation are not necessarily captured in the coarse grid, resulting in the aforementioned underestimation. It should be noted that while the higher resolution cases do not result in an exact recovery of dissipation, the results are far better than the corresponding coarser cases. Although resolution has been tripled in the streamwise direction and doubled in the spanwise and vertical directions, the resolution remains coarser than the body-inclusive simulations. Given further refinement, the results are expected to continue to approach the dissipation of the body-inclusive simulations but this level of refinement is deemed sufficient to illustrate the sensitivity of certain terms to grid resolution.

Advection and transport are similarly examined in figure 4.9. Regardless of Fr, the hybrid

model results in an overall underestimation in advection (A) although with higher grid resolution, the results are in slightly better agreement with the body-inclusive simulations. While differences attributed to spatial resolution have been addressed, another source of error concerns the temporal resolution. These terms are particularly difficult to capture given the coarseness of the time series used in post-processing to obtain area-integrated streamwise-evolving statistics. The low and high frequency modes associated with these terms are sensitive to both time interval as well as the number of temporal ensembles used in post-processing. The coarser temporal resolution representative of the time variation of any given data plane is almost entirely responsible for the overall error in advection. Transport is overestimated by the hybrid model despite increasing resolution for all Fr. With further analysis of the individual transport components given in equation 4.9, little change is noted in the triple correlation and pressure transport components with improved grid refinement. However, the viscous component shows significant change particularly near the inlet where it is magnified in the higher resolution cases. This is consistent with the underestimation of dissipation previously noted and its increase with improved grid resolution. Additional grid refinement and improved temporal resolution would lead to better agreement with the body-inclusive simulations.

Buoyancy flux (B) is an important term in the $t.k.e.$ balance for $Fr = 1$. Figure 4.10 shows that both the coarse and higher resolution simulations agree well with the body-inclusive simulations for $Fr = 1$, capturing the phase and amplitude of the buoyancy flux oscillations. As noted by Pal *et al.* (2017) and Chongsiripinyo & Sarkar (2017), body-generated lee waves are responsible for wake expansion and contraction occurring at intervals of half the wavelength of the lee wave. This behavior is also reflected in the buoyancy flux which shows peaks of modulation at intervals of πFr in figure 4.10.

Given even further grid refinement, the results are expected to be increasingly consistent with the body-inclusive simulations. As the majority of discrepancies occur in the near wake, in the vicinity of the inlet plane of the hybrid simulation, and the focus of this work is not to capture detailed physics in this region, it is asserted that the hybrid model is an effective tool for the future study of downstream turbulence.

4.0.19 Conclusions

An investigation of a spatially-evolving hybrid model which utilizes data downstream of a sphere in a spatially-evolving, body-inclusive simulation as inflow conditions has been performed using DNS at $Re = 3700$ and $Fr = \infty, 3$, and 1. Instantaneous flow data in the form of spanwise-vertical ($x_2 - x_3$) plane cuts were extracted every one hundred time steps upon reaching statistical steady-state in the body-inclusive simulation. These planes were subsequently mapped from a cylindrical to a Cartesian grid with coarser resolution and fed as inflow into a new simulation without a body. The sensitivity of the hybrid model inflow location was assessed via comparison of three different choices, namely $x_1/D = 3$, $x_1/D = 6$, and $x_1/D = 10$. Validation of the method was performed by comparing key results to those of body-inclusive simulations including mean flow evolution, flow visualization, and turbulence.

Mean flow analysis revealed that inflow location requires careful consideration. It was determined that locations which coincide with complex flow (as in the case of $x_1/D = 3$ in the recirculation region) are not ideal choices and sufficient distance must be placed between the body and extraction location so as to avoid issues associated with this region. The other choices of location, $x_1/D = 6$ and $x_1/D = 10$, were found to be appropriate choices as they provide this separation between the body and the extraction location.

Vorticity visualizations for the stratified cases illustrated the strong qualitative agreement between the body-inclusive and hybrid model simulations. A two-layered flow structure, phase lines of internal wave propagation, and vortex shedding were all shown to be consistent. Minor differences in small-scale capture were attributed to the coarseness of the hybrid model simulation grid. Analysis of *r.m.s* velocities and area-integrated $t.k.e$ showed decay rates to be captured using the hybrid model. Higher resolution simulations were performed to demonstrate the impact of varying grid resolution on $t.k.e$ budget terms. It is clear that production and buoyancy flux are well-captured by the hybrid method regardless of grid resolution. Dissipation and transport are better captured with the fine grid.

These results validate the hybrid model as an effective tool to study body-inclusive problems

when faced with computational resource limitations. A spatially-evolving, body-inclusive simulation can be performed to a short distance downstream and the time history of two-dimensional planes saved to be used as inflow in a separate spatially-evolving simulation. The grid size of the spatially-evolving simulation can be designed using the Kolmogorov scale at the inflow and its expected downstream variation either known from a test case or, more generally, estimated from an assumed power law. The time step is calculated using the *CFL* condition. This new simulation does not include a body and is therefore able to use a coarser grid, resulting in a less computationally expensive alternative to a body-inclusive simulation. The hybrid model is also of interest given its adaptability to a variety of flow problems. In practice, flow initialization can be taken from any source including experiments and observational data. Domains can easily be extended far downstream, addressing a limitation to the use of spatially-evolving body-inclusive simulations when studying the non-equilibrium regime and far wake. In addition, though this investigation utilized flow past a sphere, the model could be extended to a variety of flow geometries and parameterizations, further emphasizing its robustness as a computational tool for studying flow over bodies into the far wake.

Chapter 4 is a reprint of material published as follows: A. VanDine, K. Chongsiripinyo, S. Sarkar, "Hybrid spatially-evolving DNS model of flow past a sphere", *Comput. Fluids*, 171, 41-52, 2018. The author of this dissertation is the primary investigator and author of this work.

Chapter 5

Conclusion

Although specific conclusions were included throughout this work at the end of each chapter, a brief summary of the overall contributions of the dissertation follows. The physical mechanisms present in stratified shear flows have been studied using a variety of computational techniques, e.g. temporal DNS, temporal LES, and a spatially-evolving hybrid DNS model. The particular canonical examples of a stratified shear layer and the wake behind a towed sphere were considered. Varying background stratifications were used to assess the influence of buoyancy effects on turbulence development. A number of SGS models for LES and a spatially-evolving hybrid DNS model were introduced as alternatives in cases, for which, traditional DNS is made infeasible by the immense computational cost.

In chapter 2, DNS was used to investigate the flow dynamics of a shear layer in the presence of varying levels of uniform stratification. LSA showed a higher growth rate of the fastest growing mode in the two-layer configuration relative to a shear layer in uniform background stratification. A variety of secondary instabilities documented in prior works were also observed in the cases presented herein, albeit with slight differences in their emergence and growth. A distinct contraction of the shear layer thickness was observed in cases with low Ri due to the flattening of KH billows in the streamwise direction before the development of turbulence. Optimal mixing was observed in the $Ri = 0.12$ case. An investigation of the transition layers which form at the periphery of the

shear layer revealed unique mixing mechanisms and late-time turbulence. These layers thin and see stronger local stratification at late time with increasing background stratification.

Though the DNS presented in chapter 2 were enlightening, DNS can be computationally expensive with increasing *Re* due to the decrease in the smallest scales of turbulent motion. As such, chapter 3 evaluated different SGS models in order to assess the performance of LES when simulating stratified shear layers. The Dynamic Smagorinsky, Ducros, and WALE models were chosen for their use as subgrid models in previous literature. While all of the models were able to accurately capture the mean flow, the Ducros model proved the most effective in capturing the small-scale statistics such as TKE dissipation rate. Overall, the LES models were shown not to sufficiently capture convective turbulence. A grid resolution study determined the Ducros model to be the most consistently performing model whereas the Dynamic Smagorinsky and WALE models showed a notable performance drop with coarsening grid resolution. The Ducros model proved to be the least computationally expensive LES model and showed great cost savings over the comparable DNS. It is asserted to be the best choice for similar work involving stratified shear layers in the future.

A hybrid spatially-evolving DNS model was developed and tested in chapter 4 to address the limitations of both DNS and LES. This model involves extracting data downstream of a body in a spatially-evolving, body-inclusive simulation and using said data as inflow conditions for a new body-exclusive simulation. The hybrid model was employed for a towed sphere under the influence of varying levels of stratification. A number of extraction locations were tested to evaluate the sensitivity of the resulting hybrid model simulation with distance downstream of the body. It was determined that extraction could not occur too close to the body due to the influence of the recirculation region directly behind the body. Visualizations and a grid resolution study revealed the hybrid model to be an effective tool for future use as long as the time between plane extraction and the resolution of the body-exclusive grid are carefully considered. The hybrid DNS model proved to be much less computationally expensive than the comparable body-inclusive simulation.

The next logical step in this research is the use of the hybrid model for more complex

body geometries and realistic flow scenarios. The hybrid model will allow for the extension of computational domains farther downstream of the body than previously feasible due to the grid requirements close to the body in body-inclusive simulations. More extensive parameter studies (such as higher, more application-relevant Re) are also accessible. The hybrid model presented herein could be further adapted using the Ducros LES model employed to study the stratified shear layer in chapter 3. This would result in even higher savings in computational cost and allow for an abundance of future research that has, until now, been deemed prohibitively expensive.

Bibliography

ARMENIO, V. & SARKAR, SUTANU 2002 An investigation of stably stratified turbulent channel flow using large-eddy simulation. *J. Fluid Mech.* **459**, 1–42.

ARRATIA, C. 2011 Non-modal instability mechanisms in stratified and homogeneous shear flow. PhD thesis, Ecole Polytechnique X.

ARRATIA, C., CAULFIELD, C. P. & CHOMAZ, J.M. 2013 Transient perturbation growth in time-dependent mixing layers. *J. Fluid. Mech.* **717**, 90–133.

BONNIER, M., BONNETON, P. & EIFF, O. 1998 Far-wake of a sphere in a stably stratied uid: characterization of the vortex structures. *Appl. Sci. Res.* **59**, 269–281.

BONNIER, MARION & EIFF, OLIVIER 2002 Experimental investigation of the collapse of a turbulent wake in a stably stratified fluid. *Phys. Fluids* **14** (2), 791–801.

BONNIER, MARION, EIFF, OLIVIER & BONNETON, PHILIPPE 2000 On the density structure of far-wake vortices in a stratified fluid. *Dynam. Atmos. Ocean* **31**, 117–137.

BRUCKER, K. & SARKAR, S. 2007 Evolution of an initially turbulent stratified shear layer. *Phys. Fluids* **19**, 105105.

BRUCKER, KYLE A. 2009 Numerical investigation of momentumless wakes in stratified fluids. PhD thesis, University of California, San Diego.

BRUCKER, KYLE A. & SARKAR, SUTANU 2010 A comparative study of self-propelled and towed wakes in a stratified fluid. *J. Fluid Mech.* **652**, 373–404.

CAULFIELD, C. P. & PELTIER, W. R. 2000 The anatomy of the mixing transition in homogeneous and stratified free shear layers. *J. Fluid Mech.* **413**, 1–47.

CAULFIELD, C. P., TANG, W. & PLASTING, S. C. 2004 Reynolds number dependence of an upper bound for the long-time-averaged buoyancy flux in plane stratified Couette flow. *J. Fluid. Mech.* **498**, 315–332.

CHAMECKI, M., MENEVEAU, C. & PARLANGE, M. 2007 The local structure of atmospheric turbulence and its effect on the smagorinsky model for large eddy simulation. *J. Atmos. Sci.* **64**, 1941–1958.

CHASHECHKIN, YU D. 1989 Hydrodynamics of a sphere in a stratified fluid. *Fluid Dynam.* **24** (1),

1–7.

CHOMAZ, J. M., BONNETON, P., BUTET, A. & HOPFINGER, E. J. 1993*a* Vertical diffusion of the far wake of a sphere moving in a stratified fluid. *Phys. Fluids A: Fluid Dynam.* **5** (11), 2799–2806.

CHOMAZ, J. M., BONNETON, P. & HOPFINGER, E. J. 1993*b* The structure of the near wake of a sphere moving horizontally in a stratified fluid. *J. Fluid Mech.* **254**, 1–21.

CHONGSIRIPINYO, KARU, PAL, ANIKESH & SARKAR, SUTANU 2017 On the vortex dynamics of flow past a sphere at $Re = 3700$ in a uniformly stratified fluid. *Phys. Fluids* **29** (2), 020704.

CHONGSIRIPINYO, KARU & SARKAR, SUTANU 2017 Effect of stratification on the turbulent wake behind a sphere at $Re = 10,000$. In *10th International Symposium on Turbulence and Shear Flow Phenomena (TSFP10)*. Chicago, USA.

CONSTANTINESCU, G. S. & SQUIRES, K. D. 2003 LES and DES investigations of turbulent flow over a sphere at Re=10,000. *Flow Turbul. Combust.* **70**, 267–298.

DE SILVA, I., FERNANDO, H., EATON, F. & HEBERT, D. 1996 Evolution of Kelvin-Helmholtz billows in nature and laboratory. *Earth Planet. Sci. Lett.* **143**, 217–231.

DIAMESSIS, P., SPEDDING, G. & DOMARADZKI, J. 2011 Similarity scaling and vorticity structure in high-Reynolds-number stably stratified turbulent wakes. *J. Fluid Mech.* **671**, 52–95.

DIAMESSIS, P. J. & SPEDDING, G. R. 2006 Scaling and structure of turbulent wakes at high Reynolds number. In *Proceedings of the Sixth International Symposium on Stratified Flows*, pp. 11–14. University of Western Australia, Perth, Australia.

DOMMERMUTH, D. G., ROTTMAN, J. W., INNIS, G. E. & NOVIKOV, E. A. 2002 Numerical simulation of the wake of a towed sphere in a weakly stratified fluid. *J. Fluid Mech.* **473**, 83–101.

DUCROS, F., COMTE, P. & LESIEUR, M. 1996 Large-eddy simulation of transition to turbulence in a boundary layer developing spatially over a flat plate. *J. Fluid Mech.* **326**, 1–36.

FRITTS, D. 1982 Shear excitation of atmospheric gravity waves. *J. Atmos. Sci.* **39**, 1936–1952.

FURUICHI, N. & HIBIYA, T. 2015 Assessment of the upper-ocean mixed layer parameterizations using a large eddy simulation model. *J. Geophys. Res. Oceans* **120**, 2350–2369.

GERMANO, MASSIMO, PIOMELLI, UGO, MOIN, PARVIZ & CABOT, WILLIAM H. 1991 A dynamic subgrid-scale eddy viscosity model. *Phys. Fluids A* **3** (7), 1760–1765.

GOURLAY, M. J., ARENDT, S. C., FRITTS, D. C. & WERNE, J. 2001 Numerical modeling of initially turbulent wakes with net momentum. *Phys. Fluids* **13** (12), 3783–3802.

HAZEL, P. 1972 Numerical studies of the stability of inviscid stratified shear flows. *J. Fluid Mech.* **51**, 39–61.

JOHNSTON, T. & RUDNICK, D. 2009 Observations of the transition layer. *J. Phys. Oceanogr.* **39**,

780–797.

KAMINSKI, A. K. & SMYTH, W. D. 2019 Stratified shear instability in a field of pre-existing turbulence. *J. Fluid Mech.* **862**, 639–658.

KHANI, S. 2018 Mixing efficiency in large-eddy simulations of stratified turbulence. *J. Fluid Mech.* **849**, 373–394.

LAWRENCE, G. A., BROWAND, F. K. & REDEKOPP, L. G. 1991 The stability of a sheared density interface. *Phys. Fluids A: Fluid Dyn.* **3** (10), 2360–2370.

LILLY, D. K. 1992 A proposed modification of the Germano subgrid-scale closure method. *Phys. Fluids A* **4** (3), 633–635.

LIN, JUNG TAI & PAO, YIH HO 1979 Wakes in stratified fluids. *Annu. Rev. Fluid Mech.* **11**, 317–338.

LIN, Q., BOYER, D L. & FERNANDO, H. J. S. 1992*a* Turbulent wakes of linearly stratified flow past a sphere. *Phys. Fluids A: Fluid Dynam.* **4** (8), 1687–1696.

LIN, Q., LINDBERG, W. R., BOYER, D. L. & FERNANDO, H. J. S. 1992*b* Stratified flow past a sphere. *J. Fluid Mech.* **240**, 315–354.

LUND, T. S., WU, X. & SQUIRES, K. D. 1998 Generation of turbulent inflow data for spatially-developing boundary layer simulations. *J. Comput. Phys.* **140**, 233–258.

MASHAYEK, A., CAULFIELD, C. P. & PELTIER, W. R. 2013 Time-dependent, non-monotonic mixing in stratified turbulent shear flows: implications for oceanographic estimates of buoyancy flux. *J. Fluid. Mech.* **736**, 570–593.

MASHAYEK, A. & PELTIER, W. R. 2012*a* The 'zoo' of secondary instabilities precursory to stratified shear flow transition. Part 1: Shear aligned convection, pairing, and braid instabilities. *J. Fluid Mech.* **708**, 5–44.

MASHAYEK, A. & PELTIER, W. R. 2012*b* The 'zoo'of secondary instabilities precursory to stratified shear flow transition. Part 2: The influence of stratification. *J. Fluid Mech.* **708**, 45–70.

MASHAYEK, A. & PELTIER, W. R. 2013 Shear-induced mixing in geophysical flows: does the route to turbulence matter to its efficiency? *J. Fluid Mech.* **725**, 216–261.

MATER, BENJAMIN D. & VENAYAGAMOORTHY, SUBHAS KARAN 2014 A unifying framework for parameterizing stably stratified shear-flow turbulence. *Phys. Fluids* **26** (3), 036601.

MEUNIER, PATRICE, DIAMESSIS, PETER J. & SPEDDING, GEOFFREY R. 2006 Self-preservation in stratied momentum wakes. *Phys. Fluids* **18** (10), 106601.

NICOUD, F. & DUCROS, F. 1999 Subgrid-scale stress modeling based on the square of the velocity gradient tensor. *Flow Turbul. Combust.* **62**, 183–200.

ORR, T. S., DOMARADZKI, J. A., SPEDDING, G. R. & CONSTANTINESCU, G. S. 2015 Numerical simulations of the near wake of a sphere moving in a steady, horizontal motion through a linearly stratified fluid at Re = 1000. *Phys. Fluids* **27** (3), 035113.

OSBORN, T.R. 1980 Estimates of the local rate of vertical diffusion from dissipation measurements. *J. Phys. Oceanogr.* **10**, 80–89.

PAL, A., SARKAR, S., POSA, A. & BALARAS, E. 2016 Regeneration of turbulent fluctuations in low-Froude-number flow over a sphere at a Reynolds number of 3700. *J. Fluid Mech.* **804**.

PAL, A., SARKAR, S., POSA, A. & BALARAS, E. 2017 Direct numerical simulation of stratified flow past a sphere at a subcritical Reynolds number of 3700 and moderate Froude number. *J. Fluid Mech.* **826**, 531.

PAO, H. P. & KAO, T. W. 1977 Vortex structure in the wake of a sphere. *Phys. Fluids* **20** (2), 187–191.

PASQUETTI, R. 2011 Temporal/spatial simulation of the stratified far wake of a sphere. *Comput. Fluids* **40**, 179–187.

PELTIER, W. & CAULFIELD, C. 2003 Mixing efficiency in stratified shear flows. *Annu. Rev. Fluid Mech.* **35**, 135–167.

PHAM, H. T. & SARKAR, S. 2010 Transport and mixing of density in a continuously stratified shear layer. *J. Turbul.* **11** (24), 1–23.

PHAM, H. T. & SARKAR, S. 2014 Large eddy simulations of a stratified shear layer. *J. Fluids Eng.* **136**, 060913.

PHAM, H. T., SARKAR, S. & BRUCKER, K. 2009 Dynamics of a stratified shear layer above a region of uniform stratification. *J. Fluid Mech.* **630**, 191–223.

PHAM, H. T., SARKAR, S. & WINTERS, K. B. 2013 Large-eddy simulation of deep-cycle turbulence in an equatorial undercurrent model. *J. Phys. Oceanogr.* **43**, 2490–2502.

PHAM, HIEU T., SMYTH, W. D., SARKAR, S. & MOUM, J. N. 2017 Seasonality of deep-cycle turbulence in the Eastern Equatorial Pacific. *JPO* **47**, 2189–2208.

POSA, A. & BALARAS, E. 2018 Large-eddy simulations of a notional submarine in towed and self-propelled configuration. *Comput. Fluids* **165**, 116–126.

REDFORD, J. A., LUND, T. S. & COLEMAN, G. N. 2015 A numerical study of a weakly stratified turbulent wake. *J. Fluid Mech.* **776**, 568–609.

RILEY, JAMES J. & LELONG, MARIE PASCALE 2000 Fluid motions in the presence of strong stable stratification. *Annu. Rev. Fluid Mech.* **32**, 613–657.

SALEHIPOUR, H. & PELTIER, W. R. 2015 Diapycnal diffusivity, turbulent Prandtl number and mixing efficiency in Boussinesq stratified turbulence. *J. Fluid Mech.* **775**, 464–500.

SALEHIPOUR, H., PELTIER, W. R. & MASHAYEK, A. 2015 Turbulent diapycnal mixing in stratified shear flows: the influence of Prandtl number on mixing efficiency and transition at high Reynolds number. *J. Fluid Mech.* **773**, 178–223.

SCHOWALTER, D., VAN ATTA, C. W. & LASHERAS, J. C. 1994 A study of streamwise vortex structure in a stratified shear layer. *J. Fluid Mech.* **281**, 247–291.

SCOTTI, A. 2010 Large eddy simulation in the ocean. *Int. J. Comput. Fluid D.* **24** (10), 393–406.

SHIH, L. H., R., KOSEFF J., IVEY, G. N. & FERZIGER, J. H. 2005 Parameterization of turbulent fluxes and scales using homogeneous sheared stably stratified turbulence simulations. *J. Fluid Mech.* **525**, 193–214.

SMYTH, W. D. & MOUM, J. N. 2000*a* Anisotropy of turbulence in stably stratified mixing layers. *Phys. Fluids* **12** (6), 1343–1362.

SMYTH, W. D. & MOUM, J. N. 2000*b* Length scales of turbulence in stably stratified mixing layers. *Phys. Fluids* **12** (6), 1327–1342.

SMYTH, W. D., MOUM, J. N. & CALDWELL, D. R. 2001 The efficiency of mixing in turbulent patches: Inferences from direct simulations and microstrucure observations. *J. Phys. Oceanogr.* **31**, 1969–1992.

SMYTH, W. D., MOUM, J. N., LI, Z. & THORPE, S. 2013 Diurnal shear instability, the descent of the surface shear layer, and the deep cycle of equatorial turbulence. *J. Phys. Oceanogr.* **43**, 2432–2455.

SMYTH, W. D., MOUM, J. N. & NASH, J. D. 2011 Narrowband oscillations at the upper equatorial ocean. Part II: Properties of shear instabilities. *J. Phys. Oceanogr.* **41**, 412–428.

SPEDDING, G. R. 1997 The evolution of initially turbulent bluff-body wakes at high internal Froude number. *J. Fluid Mech.* **337**, 283–301.

SPEDDING, GEOFFREY R. 2014 Wake signature detection. *Annu. Rev. Fluid Mech.* **46**, 273–302.

SPEDDING, G. R., BROWAND, F. K. & FINCHAM, A. M. 1996 Turbulence, similarity scaling and vortex geometry in the wake of a towed sphere in a stably stratified fluid. *J. Fluid Mech.* **314**, 53–103.

DE STADLER, MATTHEW B., SARKAR, SUTANU & BRUCKER, KYLE A. 2010 Effect of the Prandtl number on a stratified turbulent wake. *Phys. Fluids* **22** (9), 95–102.

SUNDERMEYER, M., SKYLLINGSTAD, E., LEDWELL, J., CONCANNON, B., TERRAY, E., BIRCH, D., PIERCE, S. & CERVANTES, B. 2014 Observations and numerical simulations of large-eddy circulation in the ocean surface mixed layer. *Geophys. Res. Lett.* **41**, 7584–7590.

THORPE, S. A. 1973 Experiments on instability and turbulence in a stratified shear flow. *J. Fluid Mech.* **61**, 731–751.

VANDINE, A., CHONGSIRIPINYO, K. & SARKAR, S. 2018 Hybrid spatially-evolving DNS model of flow past a sphere. *Comput. Fluids* **171**, 41–52.

WATANABE, TOMOAKI, RILEY, JAMES J., NAGATA, KOJI, ONISHI, RYO & MATSUDA, KEIGO 2018 A localized turbulent mixing layer in a uniformly stratified environment. *J. Fluid Mech.* **849**, 245–276.

WILLIAMSON, J. H. 1980 Low-storage runge-kutta schemes. *J. Comput. Phys.* **35**, 48–56.

XIANG, X., MADISON, T. J., SELLAPPAN, P. & SPEDDING, G. R. 2015 The turbulent wake of a towed grid in a stratified fluid. *J. Fluid Mech.* **775**, 149–177.